Gottfried Wilhelm Leibniz Universität Hannover
Fakultät für Mathematik und Physik
Max-Planck-Institut für Gravitationsphysik
Albert-Einstein-Institut

Leibniz Universität Hannover

Binary Merger Observations & Numerical Relativity

MASTER THESIS on the subject

Time and Frequency Domain Modelling of Gravitational Waves

for obtaining the academic degree
MASTER OF SCIENCE

presented by
Jannik Mielke
Matriculation number: 10014122

under the supervision of
Dr. Frank Ohme and Dr. Shrobana Ghosh

submitted on
24 November 2023

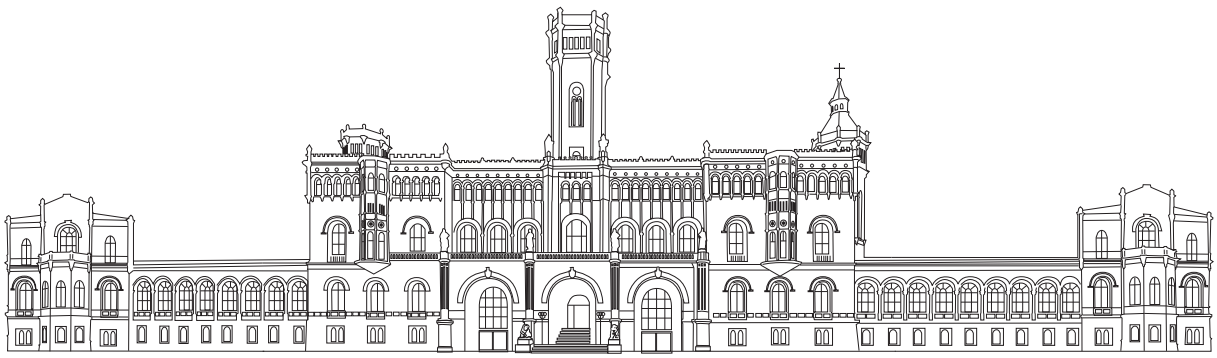

Day of submission: 24 November 2023
Changes from: 7 May 2024

Abstract

Detections of gravitational waves from astrophysical sources such as binary black holes by LIGO and Virgo has attracted widespread attention from the scientific community, the media and the general public. Among these sources, precessing systems with a misalignment of the black hole spin and the orbital angular momentum are of particular interest because of the rich dynamics they offer. For aligned-spin systems, the energy and momentum emitted above the orbital plane is symmetric to the emission below the plane. For mis-aligned systems, however, this is not the case and amplitude and phase modulations will appear in the waveform itself. Even when transformed to a coprecessing frame that follows the orbital angular momentum direction, such asymmetric features are clearly visible. When the signal is decomposed into modes of spin-weighted spherical harmonics, we can discuss the asymmetry between the negative and positive m-modes by defining an anti-symmetric waveform, which is neglected in most waveform models used in gravitational wave data analysis to date. Mode asymmetry is therefore a hot topic in the gravitational wave community, with many questions still to be answered. In this thesis, we analyse the phenomenology of the anti-symmetric waveform for several binary black hole configurations and relate it to the physics of remnant black hole recoil. We find strong correlations between the intrinsic system parameters and the amplitude and phase of the anti-symmetric waveform, and hence the magnitude of the out-of-plane recoil velocity.

Contents

1 Introduction

The Universe, with its unimaginable size and sheer endless possibilities, has inspired the minds of humanity for centuries. Humans observed the sky with the naked eye, or later with instruments such as telescopes, and tried to build a theory based on their observations. Nowadays, it is usually the other way round, and we confirm or reject the predictions of our theoretical models of nature by the outcome of experiments. This was also the case for gravitational waves (GWs), oscillations in the curvature of spacetime that Albert Einstein predicted in the early 20th century as a result of his theory of general relativity (GR) [1], which is still our current understanding of gravity. Almost 100 years later, on 14 September 2015, the first direct detection of a GW by the advanced Laser Interferometer Gravitational-Wave Observatory (LIGO) finally verified the existence of GWs [2]. The source of the detected GW was the inspiral and merger process 1.4 billion years ago of two black holes (BHs) with masses about 30 times that of the Sun. A BH is an extremely dense object with a strong gravitational field. With the first GW detection, a new era in astronomy has been opened up. To date, nearly 100 observations have been published by the LIGO-Virgo-KAGRA (LVK) collaboration [3–5], including a binary neutron star (BNS) merger [6] and two neutron star-black hole (NSBH) coalescences [7]. The most recent observation was the evidence of a GW background radiation by several pulsar timing array (PTA) collaborations, which take a different approach, observing and analysing a set of galactic pulsars to look for correlated signatures in the arrival times of the pulses at Earth [8–10]. The range of applications of GW detection is vast, from answering questions about fundamental physics [11–19] to our understanding of stellar evolution [20–23].

Besides challenges in the instrument's technology and in data analysis, the power of new discoveries from GW detection is limited by our ability to model the expected signals. Without an accurate understanding of how the physical characteristics of a source affect their waveform, measuring and interpreting these characteristics becomes problematic. While simple approximate waveforms were useful for the first detections and data analysis explorations, the true value of future GW astronomy lies in the need for precise theoretical models of waveforms. GW modelling can be understood in many ways, but the most informative step is always to analyse the phenomenology of the time-consuming full numerical solution of Einstein's GR theory for a given initial value problem. Such a solution, which usually takes the form of a wave in a matter-free spacetime, allows us to find imprints of the initial configuration physics and its time evolution. This is exactly how the title of this thesis should be interpreted, including the fact that understanding the physics of the GW source mainly means operating in the time domain, as the frequency domain is less intuitive and more useful for data analysis approaches.

More specifically, in this thesis we study a subtle physical effect that is noticeable in GW signals from numerical simulations of generic spinning binary black hole (BBH) systems or

in highly specialised waveform models such as `NRSur7dq4` [24], which is directly based on numerical simulations and which we will mainly use in this work. The physical effect mentioned is the asymmetry between the $+m$ and $-m$ multipoles of the wave's spherical harmonic decomposition. Due to these asymmetries, energy and linear momentum are preferentially radiated along or opposite to the orbital angular momentum, leading to an out-of-plane recoil of the remnant BH, since linear momentum is conserved. The mode asymmetries are of a small order of magnitude compared to the overall signal strength and are therefore neglected in most standard waveform models, but are essential if the full spin and recoil information is to be extracted with current or future detectors [25–30]. Motivated by a small number of publications that have studied the mode asymmetry in an abstract mathematical framework [31] or with the aim of building a first model [32] or of analysing it in terms of the recoil [33], here we bring together some of their concepts and further develop the relations between all of them.

The reader who is already familiar with the mathematical concepts and the basics of GW detection and modelling may wish to skip sec. 2 and move directly to the discussion of the imprint of the multipole asymmetry on the waveform of precessing BBHs in sec. 3. In sec. 4 we use our new knowledge of the asymmetry and relate it to the recoil velocity of the remnant BH. At the end of this thesis we summarise our results and give an outlook in sec. 5. All code related to this thesis is open source and available at `https://github.com/janmie1701/master-thesis`.

2 Gravitational waves

This section introduces important basic concepts of GWs, a fundamental prediction of Einstein's theory of GR. We start by exploring the mathematical foundations, including the most basic conceptual form of Einstein's equations in sec. 2.1, and go into more detail in sec. 2.2, until we have a theoretical framework to describe the GW radiation of precessing BBHs, which will be deeply analysed in this thesis. We will then go into the practical aspects, from the description of the detection of GWs in sec. 2.3 to the explanation of their modelling by different approaches in sec. 2.4.

2.1 Einstein field equations

The fundamental concept to describe the interaction between matter, space and time is the theory of GR. We briefly summarise standard textbooks by Hartle [34] and Schutz [35] in this chapter. In 1916 Albert Einstein published his pioneering work about the interpretation of gravity as a geometric property of a curved spacetime [36]. The American theoretical physicist John Archibald Wheeler summed up the Einstein field equations (EFE) in a few straightforward words: "Space tells matter how to move, matter tells space how to curve" [37]. In more mathematical words, the EFE read

$$R_{\mu\nu} - \frac{1}{2}Rg_{\mu\nu} + \Lambda g_{\mu\nu} = \frac{8\pi G}{c^4}T_{\mu\nu}\,. \tag{2.1}$$

To understand this expression, which is technically a set of ten nonlinear partial differential equations, we need to look at the key concept in GR that describes the local geometry of spacetime, called the *metric tensor* $g_{\mu\nu}$, for which the EFE has to be solved. It is often expressed as the line element in a four-dimensional manifold

$$\mathrm{d}s^2 = g_{\mu\nu}\mathrm{d}x^\mu \mathrm{d}x^\nu\,, \tag{2.2}$$

where we have used the Einstein summation convention of implicitly summing repeated indices. $R_{\mu\nu}$ is the *Ricci curvature tensor* and can be understood as a quantification of how the local geometry described by a specific metric tensor deviates from the geometry of the standard Minkowski spacetime $\eta = \mathrm{diag}(-1, +1, +1, +1)$. The Ricci tensor can be expressed with *Christoffel symbols* as

$$R_{\mu\nu} = \partial_\alpha \Gamma^\alpha{}_{\mu\nu} - \partial_\nu \Gamma^\alpha{}_{\mu\alpha} + \Gamma^\alpha{}_{\beta\alpha}\Gamma^\beta{}_{\mu\nu} - \Gamma^\alpha{}_{\beta\nu}\Gamma^\beta{}_{\mu\alpha} \tag{2.3}$$

in a local coordinate system. The Christoffel symbols are defined as

$$\Gamma^\alpha{}_{\mu\nu} = \frac{1}{2}g^{\alpha\beta}\left(\partial_\mu g_{\beta\nu} + \partial_\nu g_{\mu\beta} - \partial_\beta g_{\mu\nu}\right) \tag{2.4}$$

and are some auxiliary quantities in the concept of differential geometry to describe covariant derivatives on manifolds. By contraction of the Ricci tensor, the *Ricci scalar*

$$R = g^{\mu\nu} R_{\mu\nu} \tag{2.5}$$

can be derived.

The *cosmological constant* Λ is a constant coefficient of a term Einstein added to his field equations to explain his assumption of a static Universe. After Edwin Hubble's discovery that the Universe is expanding, Einstein set the cosmological constant to zero. Nowadays this quantity is interpreted as the energy density of vacuum and plays a huge role in the context of explaining the accelerated expansion of the Universe and dark energy. The *stress-energy tensor* $T_{\mu\nu}$ describes the density and flux of momentum and energy in spacetime. It is the gravitational field's source and provides a mathematical description of how matter and energy interact with spacetime.

The geometrized unit system, where $G = c = 1$ is set, simplifies many equations in GR. It follows that physical quantities like energy, time and length have the unit of mass. This convenient choice of physical units is used consistently throughout this thesis. SI units are only used in specific sections to get a better intuitive feeling for the quantitative dimensions.

2.1.1 Schwarzschild metric

One of the most famous analytical solutions of the EFE is the Schwarzschild solution. A few months after Einstein's publication in 1915, Karl Schwarzschild considered the EFE in a vacuum, meaning $T_{\mu\nu} = 0$, and assumed that all mass m is at a singular point at the origin. The solution he found is nowadays known as the *Schwarzschild metric*. Its line element in four-dimensional spherical coordinates, i.e. time t, radial line r, polar angle θ and azimuthal angle ϕ, reads [37]

$$\mathrm{d}s^2 = -\left(1 - \frac{2m}{r}\right)\mathrm{d}t^2 + \frac{1}{1 - \frac{2m}{r}}\,\mathrm{d}r^2 + r^2\,\mathrm{d}\theta^2 + r^2\sin^2(\theta)\,\mathrm{d}\phi^2\,. \tag{2.6}$$

This solution is relevant to astrophysics because it describes the metric of an uncharged, non-rotating BH. Additionally, due to *Birkhoff's theorem* [37], it characterises the outer gravitational field of an isolated, homogeneous, non-charged, non-rotating star of mass m. When looking at the line element, two special values of the radial coordinate, $r = 0$ and $r = 2m$, play a crucial role in the understanding of the properties of BHs. The true physical $r = 0$ singularity is a point of infinite density and curvature at the centre of the BH, while at the *Schwarzschild radius* $r_S = 2m$ the event horizon represents the boundary beyond which nothing can escape the gravitational attraction, including light.

2.1.2 Kerr metric

Because most of the BHs known through astrophysical observations are not of a static kind, it is worthwhile to study the properties of rotating BHs. A deeper understanding of rotating BHs can be found in Ref. [38], on which this chapter is based. The *Kerr metric*, another solution of the EFE, describes rotating BHs of mass m with a specific angular momentum $a = |\vec{s}|/m \in [0, m]$, also known as the Kerr parameter. The line element in *Boyer-Lindquist coordinates* has the following form:

$$\begin{aligned} \mathrm{d}s^2 = &-\left(1 - \frac{2mr}{\rho^2}\right)\mathrm{d}t^2 - \frac{4mra\sin^2(\theta)}{\rho^2}\,\mathrm{d}\phi\,\mathrm{d}t + \frac{\rho^2}{\Delta}\,\mathrm{d}r^2 + \rho^2\,\mathrm{d}\theta^2 \\ &+ \left(r^2 + a^2 + \frac{2mra^2\sin^2(\theta)}{\rho^2}\right)\sin^2(\theta)\,\mathrm{d}\phi^2\,, \end{aligned} \tag{2.7}$$

where $\rho^2 = r^2 + a^2\cos^2(\theta)$ and $\Delta = r^2 - 2mr + a^2$. Rotating BHs have a ring singularity at $r = a$ and a more complex structure of event horizons. Event horizons occur formally at spacetime points where the radial component of the underlying metric becomes singular, meaning $g^{rr} = 0$. Two solutions are obtained, commonly denoted by the symbols r_+ and r_-:

$$r_\pm = m \pm \sqrt{m^2 - a^2}\,. \tag{2.8}$$

There is a transition to the Schwarzschild limit of the event horizon of a non-rotating BH when $a = 0$, then $r_+ = 2m$ and $r_- = 0$.

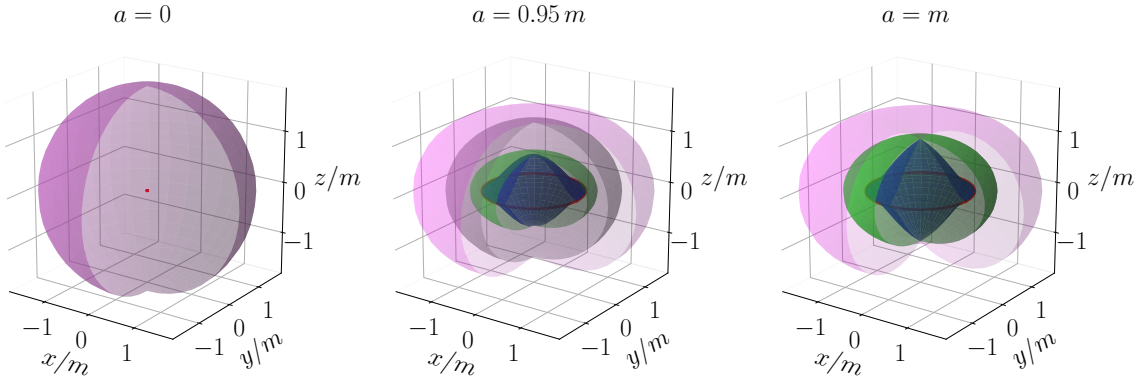

Figure 2.1: Important surfaces of the Kerr metric for a non-rotating, highly rotating and extremely rotating BH. The figures include the ergosphere outer boundary r_{E+} (magenta), the outer event horizon r_+ (grey), the inner stationary limit surface r_{E-} (green) and the inner event horizon r_- (blue). The ring singularity (red) is located at the cusp of the blue surface. In the Schwarzschild limit, $a = 0$, the ring singularity, the green and blue surfaces are one point at the origin, and the grey and magenta surfaces are identical. This figure has been modified based on Fig. 1 in Ref. [38] with ideas from a computational GR lecture by Matthias Hanauske in Summer Term 2021 at Goethe University Frankfurt, summarised on this website [39].

Solving $g_{tt} = 0$ leads to two further interesting solutions:

$$r_{E\pm} = m \pm \sqrt{m^2 - a^2 \cos^2(\theta)}\,. \tag{2.9}$$

These are known as the *stationary limit surfaces* or surfaces of infinite redshift. The space between r_{E+} and and the outer horizon r_+ is called ergosphere. In the *ergosphere*, particles, even light, have to co-rotate with the spin direction due to the strong *frame-dragging effect*. The inner surface structure is visualised in Fig. 2.1. Of course, the Kerr metric is only a theoretical concept for rotating BHs. However, even if understanding the structure of the inner horizons is of secondary importance, their spacetime in the outer regions strongly influences the matter, like accretion disks around a rotating BH, and is therefore highly relevant to astrophysics [40].

2.2 Mathematical concepts of gravitational waves

Spacetime geometry is not just a rigid background, it also exhibits a dynamic behaviour. One of the most fascinating consequences of the spacetime dynamics is that perturbations in the spacetime geometry can propagate as waves. This solution of the EFE is commonly known as a GW, which Einstein predicted in 1916 [1], just one year after his publication on GR [36]. GWs have analogies to electromagnetic waves. They transport energy, travel at the speed of light, and have the ability to interfere. In contrast, GWs can pass through matter without being significantly absorbed or scattered, making them very difficult to measure.

Unless otherwise stated, the first three chapters of this sec. 2.2 follow the standard textbooks by Hartle [34], Misner/Thorne/Wheeler [37] and Schutz [35]. In addition, several concepts are derived from the lecture on gravitational physics given by Frank Ohme at the Leibniz University Hanover in the summer semester of 2023.

2.2.1 Linearised gravity in vacuum

In the weak gravitational-field limit, perturbation theory can be applied to the flat Minkowski metric $\eta_{\mu\nu}$. This method is called linearised gravity and is widely used to describe GWs. Consider an almost flat spacetime with a small metric perturbation $h_{\mu\nu}$. There is a coordinate frame in which

$$g_{\mu\nu} = \eta_{\mu\nu} + h_{\mu\nu}, \qquad |h_{\mu\nu}| \ll 1\,. \tag{2.10}$$

Keeping only terms up to linear order in $h_{\mu\nu}$ when calculating the Ricci tensor, the vacuum EFE simplify to

$$R_{\mu\nu} = \frac{1}{2}(-\Box h_{\mu\nu} + \partial_\mu V_\nu + \partial_\nu V_\mu) = 0\,, \tag{2.11}$$

where we have introduced the d'Alembert operator $\Box = \partial_\mu \partial^\mu$ and an auxiliary vector

$$V_\mu = \partial_\alpha h_\mu{}^\alpha - \frac{1}{2}\partial_\mu h_\alpha{}^\alpha\,. \tag{2.12}$$

The choice of coordinates for which Eq. (2.10) holds is not unique. We can still apply a small coordinate transformation of the form

$$x'^{\mu} = x^{\mu} + \xi^{\mu}, \qquad |\partial_{\nu}\xi^{\mu}| \ll 1\,, \tag{2.13}$$

also called a gauge transformation. Under this transformation, $h_{\mu\nu}$ transforms as

$$h'_{\mu\nu} = h_{\mu\nu} - \partial_{\mu}\xi_{\nu} - \partial_{\nu}\xi_{\mu}\,. \tag{2.14}$$

We can enforce $V'_{\mu} = 0$. To achieve this, ξ_{μ} is required to satisfy the following relation:

$$\Box\xi_{\mu} = \partial_{\alpha}h_{\mu}{}^{\alpha} - \frac{1}{2}\partial_{\mu}h_{\alpha}{}^{\alpha}\,. \tag{2.15}$$

A solution to this equation can always be found [41]. Even more, this relation is not unique since a solution of the homogeneous equation $\Box\xi_{\mu} = 0$ can be added, say to the right-hand side, and still leave Eq. (2.15) valid. This results in the *Lorenz gauge* condition:

$$0 = \partial_{\alpha}h_{\mu}{}^{\alpha} - \frac{1}{2}\partial_{\mu}h_{\alpha}{}^{\alpha}\,. \tag{2.16}$$

For a simpler representation, we have chosen to omit the dash in the notation for the transformed coordinate system. By doing so, we see that in this Lorenz gauge Eq. (2.11) becomes a familiar form of the wave equation:

$$\Box h_{\mu\nu} = 0\,. \tag{2.17}$$

A general complex solution reads

$$h_{\mu\nu} = A_{\mu\nu}e^{ik_{\mu}x^{\mu}}\,, \tag{2.18}$$

where the wave vector k_{μ} has to fulfil $k_{\mu}k^{\mu} = -\omega^2 + |\vec{k}|^2 = 0$, i.e. GWs move with the speed of light. The dispersion relation $|\vec{k}| = \omega = 2\pi/\lambda$ is valid.

To find a simple representation of the symmetric perturbation tensor $h_{\mu\nu}$ underlying ten independent components, we attempt to eliminate eight components by gauge choice. Within a Lorenz gauge, a further gauge transformation can be applied that preserves the Lorenz gauge, as long as the additional transformation satisfies the wave equation. For example, looking at Eq. (2.14), we can choose $\partial_{\mu}\xi_{\nu} = h_{\mu\nu}$. These additional degrees of freedom are used to set four components of $h_{\mu\nu}$ to zero, $h^{\mu}{}_{\mu} = 0$ and $h_{0i} = 0$ with $i = 1, 2, 3$. Thus the Lorenz gauge condition in Eq. (2.16) gives $k^{\mu}h_{\mu\nu} = 0$. If we now align the coordinate system such that the z-axis is along the propagation direction, we can write $h_{\mu\nu}$ in this *transverse-traceless* (TT)

gauge as

$$h_{\mu\nu} = \begin{pmatrix} 0 & 0 & 0 & 0 \\ 0 & h_+ & h_\times & 0 \\ 0 & h_\times & -h_+ & 0 \\ 0 & 0 & 0 & 0 \end{pmatrix} . \tag{2.19}$$

The two independent remaining components are called *plus and cross polarisation*. The space between test particles is simultaneously squeezed and stretched by both polarisations. Their orientations are rotated 45° with respect to each other. It is common to consider both polarisations simultaneously by defining a complex-valued scalar *strain*,

$$h = h_+ - ih_\times \, , \tag{2.20}$$

which is very convenient when modelling waveforms, because we can get information about the strength of the GW via the absolute value $|h|$ and about the phase difference between the polarisations via the argument $\arg(h)$. The minus sign is chosen by convention.

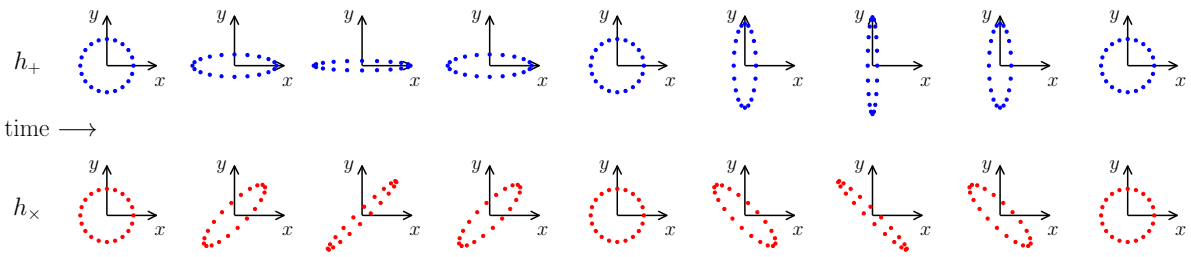

Figure 2.2: Visualisation of the two independent GW polarisations, h_+ and $h_\times$, as they affect the distances between free-floating test particles. A full period of a GW propagating along the z-axis and acting on the x-y-plane is depicted. The figure is reconstructed based on Fig. 8.1 and Eq. (8.39) in Ref. [42].

2.2.2 Sources of gravitational waves

Revisiting the full EFE, we have to consider matter as a source to generate GWs. By introducing the *trace-reversed* perturbation tensor

$$\bar{h}_{\mu\nu} = h_{\mu\nu} - \frac{1}{2}\eta_{\mu\nu}h_\alpha{}^\alpha \, , \tag{2.21}$$

so that the Lorenz gauge becomes $\partial_\alpha \bar{h}_\mu{}^\alpha = 0$, the EFE turn into

$$\Box \bar{h}_{\mu\nu} = -16\pi T_{\mu\nu} \, . \tag{2.22}$$

Analogous to the inhomogeneous electromagnetic wave equation we can obtain the general solution of Eq. (2.22) in terms of the *retarded integral*

$$\bar{h}_{\mu\nu}(t,\vec{x}) = 4\int \mathrm{d}^3x' \, \frac{T_{\mu\nu}(t-|\vec{x}-\vec{x}\,'|,\vec{x}\,')}{|\vec{x}-\vec{x}\,'|} \,. \tag{2.23}$$

To keep the weak-field approximation of linearised gravity, we approximate large distances from the source, $|\vec{x}-\vec{x}\,'| \approx |\vec{x}| := r$, and simplify Eq. (2.23):

$$\bar{h}_{\mu\nu}(t,\vec{x}) \approx \frac{4}{r}\int \mathrm{d}^3x' \, T_{\mu\nu}(t-r,\vec{x}\,') \,. \tag{2.24}$$

Using the stress-energy conservation $\partial_\mu T^{\mu\nu} = 0$ and projecting in the TT gauge [41], we can find

$$h_{ij}(t,r) = \frac{2}{r}\ddot{I}_{ij}(t-r) \,, \tag{2.25}$$

with $i,j \in \{1,2,3\}$. Here I_{ij} is the *quadrupole moment* tensor of a mass distribution,

$$I_{ij} = \int \mathrm{d}^3x' \, x'_i \, x'_j \, \rho(t-r,\vec{x}\,') \,, \tag{2.26}$$

where ρ is the mass density for non-relativistic matter.

Generally speaking, from this calculation we can say that all massive objects emit GWs if their motion is accelerated and if the motion is not perfectly spherical or rotationally symmetric. This is the case, for example, when a page is turned in this thesis or when a ball is hit in a game of table tennis. However, the masses and accelerations of objects on Earth are too small to produce GWs of sufficient magnitude to be detectable by our instruments. To detect relatively strong GWs, we must look for massive, accelerating astrophysical objects and events that produce GWs over a spectrum of wavelengths ranging from a few kilometres to larger than the observable Universe. In general, GW sources are classified into four different types: continuous, inspiral, burst and stochastic [43]. Continuous sources, often rapidly rotating neutron stars (NSs), emit constant, periodic GWs. Inspiral sources occur when two compact objects, such as NSs or BHs, spiral closer together and emit GWs of slowly increasing amplitude until they merge. Burst sources emit intense, short-lived bursts of GWs, such as supernova explosions. Stochastic sources produce a background of GWs, generated by the cumulative effect of many unresolved and indistinguishable events throughout the Universe.

2.2.3 Compact binary coalescences

Among the many different types of sources, we will focus on *compact binary coalescences* (CBCs), since they are relatively easy to describe and emit GWs in a frequency range detectable on Earth. The two-body problem in GR is not analytically solvable like the Kepler problem in classical physics, but we can get interesting results for a Newtonian orbit and some

additional assumptions. Let the binary system be characterised by two point masses m_1 and m_2, where $m_1 \geq m_2$, on a circular orbit located in the x-y-plane. The binary separation R should be much smaller than the distance to the source r. In the centre-of-mass coordinate frame, the position of the compact objects can be written as

$$\vec{x}_1 = \frac{\mu R}{m_1} \left(\cos\left(\omega_{orb} t\right), \sin\left(\omega_{orb} t\right), 0\right), \qquad \vec{x}_2 = -\frac{m_1}{m_2} \vec{x}_1 , \tag{2.27}$$

where we have defined the reduced mass $\mu = m_1 m_2 / M$ and $M = (m_1 + m_2)$ is the total mass. We can also write the binary separation as $R = |\vec{n}|$, where we have introduced $\vec{n} = \vec{x}_1 - \vec{x}_2$ as the *separation vector* from the lighter to the heavier BH.

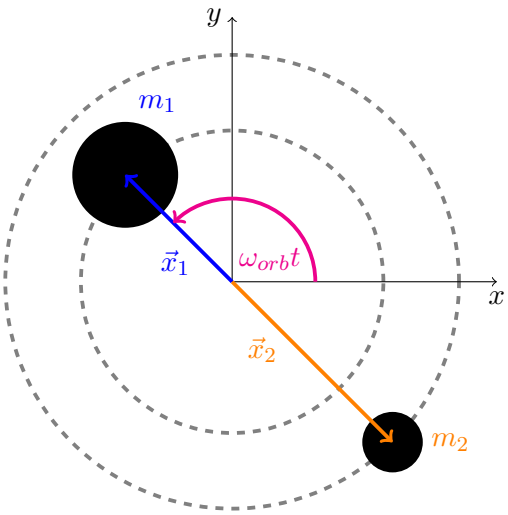

Figure 2.3: Two point masses characterised by their mass m_i and position $\vec{x}_i$ on circular orbits. Each revolves around the common centre-of-mass chosen as the origin of the coordinate system with an orbital angular velocity of ω_{orb}. The figure has been modified from Fig. 23.2 in Ref. [34] and from lecture drawings by Frank Ohme.

Applying these assumptions to the quadrupole formula in Eq. (2.25) results in

$$h_{ij} = \frac{4\mu R^2 \omega_{orb}^2}{r} \begin{pmatrix} -\cos(2\omega_{orb}(t-r)) & -\sin(2\omega_{orb}(t-r)) & 0 \\ -\sin(2\omega_{orb}(t-r)) & \cos(2\omega_{orb}(t-r)) & 0 \\ 0 & 0 & 0 \end{pmatrix} . \tag{2.28}$$

Considering the given matrix entries, $h_+ \sim \cos(2\omega_{orb}(t-r))$ and $h_\times \sim \sin(2\omega_{orb}(t-r))$, it can be observed that the GW's frequency is exactly twice the orbital frequency, $\omega_{GW} = 2\omega_{orb}$, in this idealised scenario. The two polarisations have an almost identical oscillatory behaviour, differing only by a phase shift of $\pi/2$. In addition, by plugging in some typical astrophysically motivated values for the different quantities in the amplitude factor before the matrix, we see that the strain of a GW is on the very tiny order of 10^{-21}, making its detection very difficult.

Remember also that we are dealing with astrophysical objects, i.e. a GW with a frequency of the typical order of 10^2 Hz corresponds to two objects with masses greater than the mass of the Sun orbiting 50 times per second.

The evolution of the orbital frequency of the BBH orbit can be calculated by considering next-order corrections in terms of the *post-Newtonian* (PN) expansion, a perturbative expansion in small parameters such as orbital velocity that expresses orders of magnitude of the deviations from Newton's law of universal gravitation [44]. From the conservation of energy it can be shown that in the leading order the evolution of ω_{orb} is described by the differential equation [45]

$$\dot{\omega}_{orb} = \frac{96}{5}\,\mathcal{M}_c^{5/3}\,\omega_{orb}^{11/3}\,, \tag{2.29}$$

where we have used the chirp mass

$$\mathcal{M}_c = \frac{(m_1 m_2)^{3/5}}{M^{1/5}} = \left(\frac{q}{(1+q)^2}\right)^{3/5} M \tag{2.30}$$

with the *mass ratio* $q = m_1/m_2$. By setting the integration constant such that the merger occurs at $t = 0$, i.e. $f \to \infty$ as $t \to 0$, we obtain the solution of Eq. (2.29) for $t < 0$

$$\omega_{orb} = \frac{15^{3/8}}{2^{9/8}\left(-96\mathcal{M}_c^{5/3} t\right)^{3/8}}\,. \tag{2.31}$$

It shows an increase in frequency during the inspiral, called the chirp signal, which is determined only by the chirp mass. A chirp is consistent with the fact that a part of the energy in the binary system has to be emitted in the form of GWs. Full GR confirms that the assumption of a perfectly circular binary orbit is no longer true, and that we have non-Keplerian orbits, meaning that R is shrinking as the gravitational radiation carries energy away from the system. As the compact objects get closer, their orbital velocity increases, leading to a rapid rise in GW emission. In the final stages of their inspiral, they merge into a single remnant object, such as a BH or NS, releasing an enormous amount of GW energy, on the order of several solar masses depending on the configuration. In addition to energy, GWs also remove linear and angular momentum from the system. Ruiz et al. [46] summarised the energy flux $\mathrm{d}E/\mathrm{d}t$, linear momentum flux $\mathrm{d}P_i/\mathrm{d}t$ and angular momentum flux $\mathrm{d}J_i/\mathrm{d}t$ for $i = x, y, z$ in terms of the strain h defined in Eq. (2.20):

$$\frac{\mathrm{d}E}{\mathrm{d}t} = \lim_{r\to\infty} \frac{r^2}{16\pi} \oint \mathrm{d}\Omega\, |\dot{h}|^2\,, \tag{2.32}$$

$$\frac{\mathrm{d}P_i}{\mathrm{d}t} = \lim_{r\to\infty} \frac{r^2}{16\pi} \oint \mathrm{d}\Omega\, l_i |\dot{h}|^2 \tag{2.33}$$

$$\frac{\mathrm{d}J_i}{\mathrm{d}t} = -\lim_{r\to\infty} \frac{r^2}{16\pi}\,\mathrm{Re}\left(\oint \mathrm{d}\Omega\,(\hat{L}_i h)\,\partial_t h^*\right)\,. \tag{2.34}$$

Here we introduced the standard solid angle element $\mathrm{d}\Omega$, the unit radial vector in flat space

$$\vec{l} = (\sin(\theta)\cos(\phi),\, \sin(\theta)\sin(\phi),\, \cos(\theta)) \tag{2.35}$$

and the *angular momentum operators*

$$\begin{aligned} \hat{L}_x &= -\sin(\phi)\partial_\theta - \cos(\phi)(\cot(\theta)\partial_\phi + i\, s\csc(\theta)) \\ \hat{L}_y &= \cos(\phi)\partial_\theta - \sin(\phi)(\cot(\theta)\partial_\phi + i\, s\csc(\theta)) \\ \hat{L}_z &= \partial_\phi\,, \end{aligned} \tag{2.36}$$

where $s = -2$ for h and $s = +2$ for h^*. In sec. 4.4 we will further simplify the integrals and take a closer look at the relationship between these physical flux parameters and the waveform itself.

2.2.4 Precessing binary black holes

We restrict ourselves even more to a subclass of CBCs, and focus on two BHs with arbitrary spins orbiting each other on a quasi-circular orbit. Binaries consisting of either non-spinning BHs or at least one with spin, where the spin axis is aligned with or opposite to the orbital angular momentum, are called *aligned-spin systems*. All remaining systems are categorised as *mis-aligned systems*. The GW radiation from a generic mis-aligned BBH system on a quasi-circular orbit is determined by seven intrinsic parameters, the mass ratio $q = m_1/m_2 \geq 1$ and the dimensionless spin parameters of the two BHs $\vec{\chi}_1$ and $\vec{\chi}_2$, summarised in $\lambda = \{q, \vec{\chi}_1, \vec{\chi}_2\}$. The *dimensionless spin parameter* is defined as $\vec{\chi} = \vec{s}/m^2 \leq 1$ and is related to the Kerr parameter via $a = |\vec{\chi}| \cdot m$ [47].

In most cases the total angular momentum $\vec{J} = \vec{L} + \vec{S}$ is approximately constant. It is defined as the sum of the *orbital angular momentum* $\vec{L}$ and the sum of the spin angular momenta of the two BHs $\vec{S} = \vec{s}_1 + \vec{s}_2$. We are talking about a non-precessing system when $\vec{s}_1$ and $\vec{s}_2$ are aligned with $\vec{L}$. But in general, the BH spins $\vec{s}_1$ and $\vec{s}_2$ are mis-aligned with respect to $\vec{L}$, so they exert torques on each other. This leads to a wobbling of the orbital plane, the geometric plane in which the orbit lies, i.e. $\vec{L}$ precesses around $\vec{J}$. In addition, $\vec{s}_1$ and $\vec{s}_2$ change their direction so that $\dot{\vec{L}} = -\dot{\vec{S}}$. The spin-spin and spin-orbit couplings can be described by the spin precession equations [44, 48, 49]

$$\dot{\vec{\chi}}_i(t) = \vec{\Omega}_i(t) \times \vec{\chi}_i(t)\,, \qquad i = 1, 2\,,\,. \tag{2.37}$$

$\vec{\Omega}_i$ is given in Eq. (A32) in Ref. [50]. It is a series in the PN expansion parameter $x(t)$, which can be chosen as $x(t) = M\omega_{orb}^{2/3}$. From Eq. (2.37) we can see that the magnitudes of the individual spins remain constant during the evolution of the spins. The precession frequency $\omega_i^{pre} = |\vec{\Omega}_i|$ is the frequency with which $\vec{\chi}_i$ precesses around $\vec{\Omega}_i$. In general, when both BHs are spinning, the total spin $\vec{S}$ changes its magnitude.

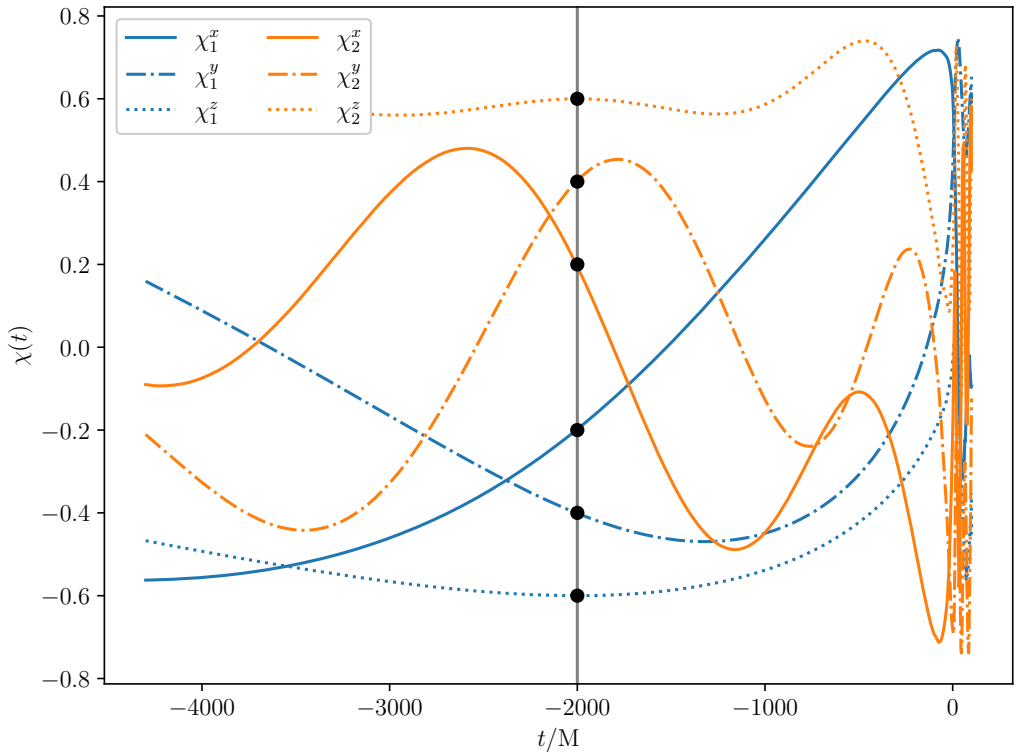

Figure 2.4: Spin dynamics of a highly precessing BBH system. The time evolution of the dimensionless spins in an inertial frame was calculated using an ODE solver implemented in `NRSur7qd4` for Eq. (2.37) with an initial condition of a $\lambda = \{3, (-0.2, -0.4, -0.6), (0.2, 0.4, 0.6)\}$ configuration defined at a reference time of $t_{ref} = -2000$ M. The spin of the heavier BH evolves over a longer time scale than that of the lighter BH. Since the PN theory collapses near the coalescence and the two BHs merge into one, so that the notation of two BHs no longer makes sense, the dynamics for $t \gtrsim -100$ M is not physical.

All the effects described above occur on three different timescales [51]. First, the BHs orbit around each other with an orbital period $t_{orb}/M \sim (R/M)^{3/2}$ given by Kepler's third law. The precession time, at which the BH spins and the orbital angular momentum changes direction, is on a timescale of $t_{pre}/M \sim (R/M)^{5/2}$. Finally, there is the radiation reaction time $t_{rr}/M \sim (R/M)^4$, where the binary separation R decreases as the system loses momentum and energy in the form of GWs. In the early inspiral we have $R \gg M$ and thus $t_{orb} \ll t_{pre} \ll t_{rr}$. This means that the BBHs go through many orbits and precession cycles before they merge.

Due to the difficulty of measuring individual spins [26, 27] and the computational intensity for the generation of waveforms for precessing systems [52–54], notable efforts have been made to reduce the size of the parameter space. Therefore, degeneracies between certain spin combinations are used to parameterise the spins of a binary. The most successful of these is the adoption of two spin parameters to describe the whole binary system, where we replace

the six spin parameters with two:

$$\chi_{\text{eff}} = \left(\frac{\vec{s}_1}{m_1} + \frac{\vec{s}_2}{m_2}\right) \cdot \frac{\vec{L}}{M}\,, \tag{2.38}$$

$$\chi_{\text{p}} = \frac{\max\left(A_1|\vec{s}_{1,\perp}|,\, A_2|\vec{s}_{2,\perp}|\right)}{A_2 m_2^2}\,. \tag{2.39}$$

Here $A_1 = 2 + \frac{3q}{2}$, $A_2 = 2 + \frac{3}{2q}$ and $|\vec{s}_{i,\perp}|$ is the magnitude of the in-plane spin component [55]. These parameters effectively quantify the amount of in-plane and out-of-plane spin of the binary system. Another useful parameter to mention is the angle θ_{LS} between $\vec{L}$ and $\vec{S}$, referred to as the *spin-orbit misalignment* or the spin-tilt [56].

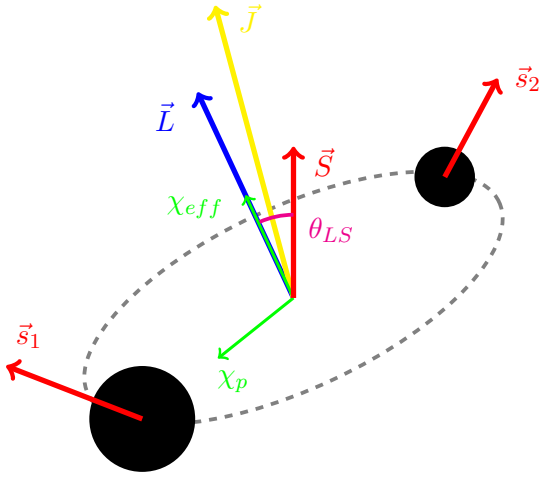

Figure 2.5: Illustration of the angles and vectors used to describe precessing BBHs. The entire system precesses around the total angular momentum $\vec{J}$. Keep in mind that χ_{eff} and χ_{p} are scalar quantities, but are drawn as vectors along $\vec{L}$ and $\vec{n}$ with a length of χ_{eff} and χ_{p}. This figure is modified based on Fig. 1 in Ref. [56].

The location and orientation of the source relative to an observer is described by another large set of extrinsic parameters, such as luminosity distance, binary inclination, declination, right ascension, polarisation angle, coalescence phase and time of arrival [57]. Of course, the extrinsic parameters are important for the actual detection of GWs, but we will focus on the variation of the intrinsic parameters, since these affect the real physics of the system. One of these physical effects in precessing BBH systems is called *mode asymmetry*, which we will analyse in detail in sec. 3 and sec. 4.

2.2.5 Spherical harmonic decomposition

We define a spherical coordinate system (t, r, θ, ϕ) with the BBH centre-of-mass at the origin. At an arbitrary reference time before the merger we fix the axis of the coordinate system along

some well-defined directions of the system. Usually the z-axis ($\theta = 0$) is parallel to the orbital angular momentum $\vec{L}$, the x-axis ($\phi = 0$) lies along the separation vector $\vec{n}$ and the y-axis ($\phi = \pi/2$) fulfils the triad. We denote this coordinate system as the *inertial frame*. Following Ref. [58] or [59], it can be shown that in this frame we can expand the GW strain in a basis of $s = -2$ *spin-weighted spherical harmonics* (SWSH):

$$h(t, r, \theta, \phi) = h_+ - ih_\times = \sum_{\ell=2}^{\infty} \sum_{m=-\ell}^{\ell} h_{\ell,m}(t, r, \lambda) \cdot {}^{-2}Y_{\ell,m}(\theta, \phi)\,. \tag{2.40}$$

The complex functions $h_{\ell,m}$ are named as the *modes* of GWs and depend on all physical intrinsic parameters λ. In the majority of cases the dominant contribution to GW radiation are the quadruple modes $\ell = 2$, $m = \pm 2$. Therefore all other modes are called higher harmonics or subdominant modes. In first order $h_{\ell,m}$ is proportional to $1/r$. This feature is used to extract the modes on spheres of various radii, when solving the EFE numerically, and then extrapolate to *future null infinity* [60]. For this reason, we drop the r dependence and the $h_{\ell,m}$ are in the following functions of time only. Furthermore, it turns out that the total mass of the binary M scales out [49], i.e. the modes are given in scaling units of M/r, which is dimensionless since mass and length have the same dimension in geometrized units, and time in units of M. In most waveform models the time of merger is defined as

$$\hat{t} = \arg\max_t \left(\sqrt{\sum_{\ell,m} |h_{\ell,m}|^2} \right)\,, \tag{2.41}$$

so roughly the peak of the dominant (2, ± 2) modes. The time series is usually shifted so that $\hat{t} = 0\,M$ [47], which we will adopt in the following chapters of this thesis.

Fig. 2.6 shows the three modes with the highest contribution to the total strain emitted by a given precessing BBH. We divide the waveform into three different regimes: *inspiral*, *merger* and *ringdown*. It is difficult to find a clear cut-off for the regimes without further information about the horizon structure of the merging BHs, but in approximation the inspiral regime is for times $t < \hat{t}$, the merger regime is around $\hat{t}$ and the ringdown regime is for $t > \hat{t}$. The phase and the amplitude for all modes increase until $\hat{t}$, which is characteristic of the long inspiral regime. The amplitude reaches its maximum in the merger regime. The now single BH is ringing and emitting exponentially damped waves.

For non-precessing binaries we can find symmetries in the negative and positive m-modes for fixed ℓ, since non-precessing systems are invariant under reflections across the orbital plane. But this is in general not true for a generic precessing system in any coordinate frame [31]. This first considerations about mode asymmetries will be analysed in more detail in many parts of this thesis and already shows the need to analyse positive and negative m-modes separately.

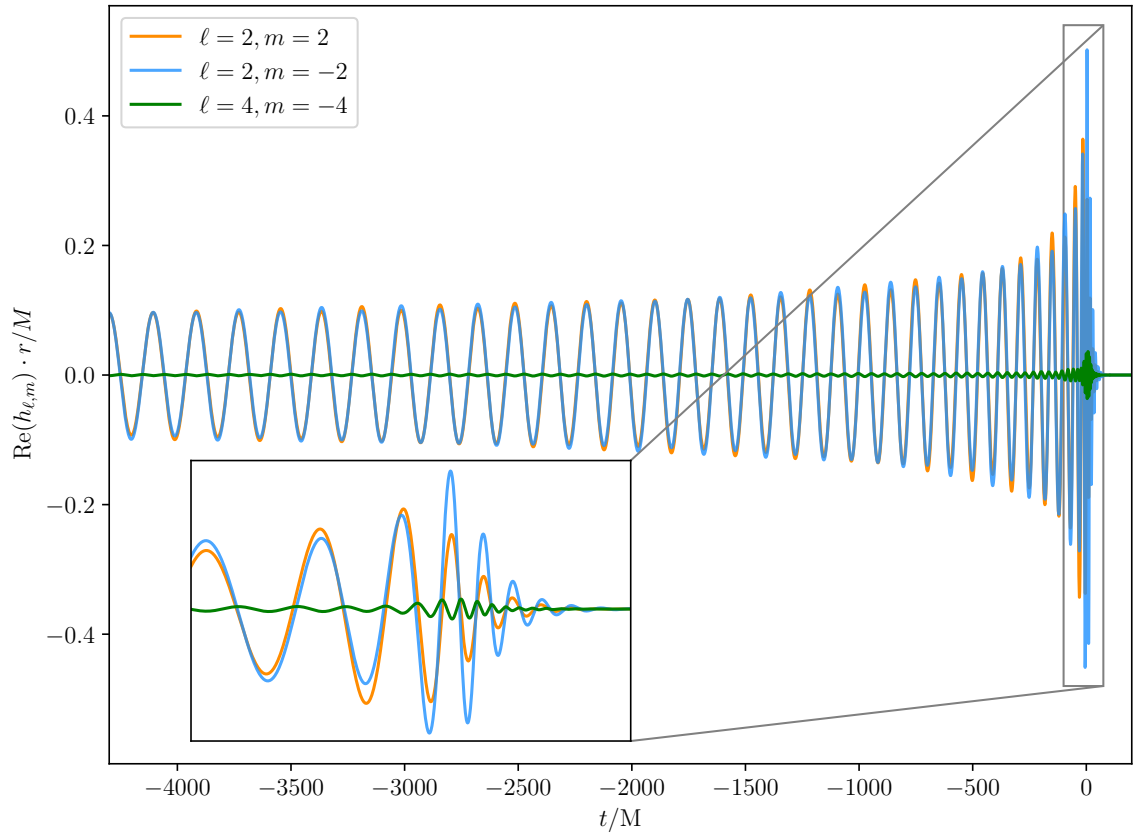

Figure 2.6: Real part of the three most dominant modes for a $\lambda = \{1, (0.8, 0, 0), (-0.8, 0, 0)\}$ configuration in a fixed inertial frame defined at a reference time of $t_{ref} = -4300\,M$. The GW's frequency and amplitude increase with time until the moment of merging at around $t \approx 0$, initiating the subsequent ringdown. Note the strong suppression of the $(4, -4)$ mode, even if this mode is the next subdominant mode after the dominant $(2, \pm 2)$ modes for this particular configuration. Especially in the merger regime, zoomed-in inset, we see a mode asymmetry between $h_{2,2}$ and $h_{2,-2}$ since we have a precessing system. The plot was generated using `NRSur7dq4` [24].

SWSH can be generated from the standard spherical harmonics and read in the Goldberg representation [61] as

$$\begin{aligned} {}^{s}Y_{\ell,m}(\theta,\phi) = (-1)^{\ell+m-s} \sqrt{\frac{(\ell+m)!(\ell-m)!(2\ell+1)}{4\pi(\ell+s)!(\ell-s)!}} \sin^{2\ell}\left(\frac{\theta}{2}\right) e^{im\phi} \\ \cdot \sum_{k=0}^{\ell-s} (-1)^k \binom{\ell-s}{k} \binom{\ell+s}{k+s-m} \cot^{2k+s-m}\left(\frac{\theta}{2}\right) . \end{aligned} \tag{2.42}$$

By definition, a function f with spin weight s transforms under rotation ψ around an choosen axis via $f \mapsto \exp(is\psi)f$. GWs of binary systems have spin weight $s = -2$. This can be seen by applying a rotation of $\psi = 2\pi/s$ around the propagation direction to Eq. (2.19). In other words it is consequence of a specific Lorentz transformation of a rank-2 tensor [42].

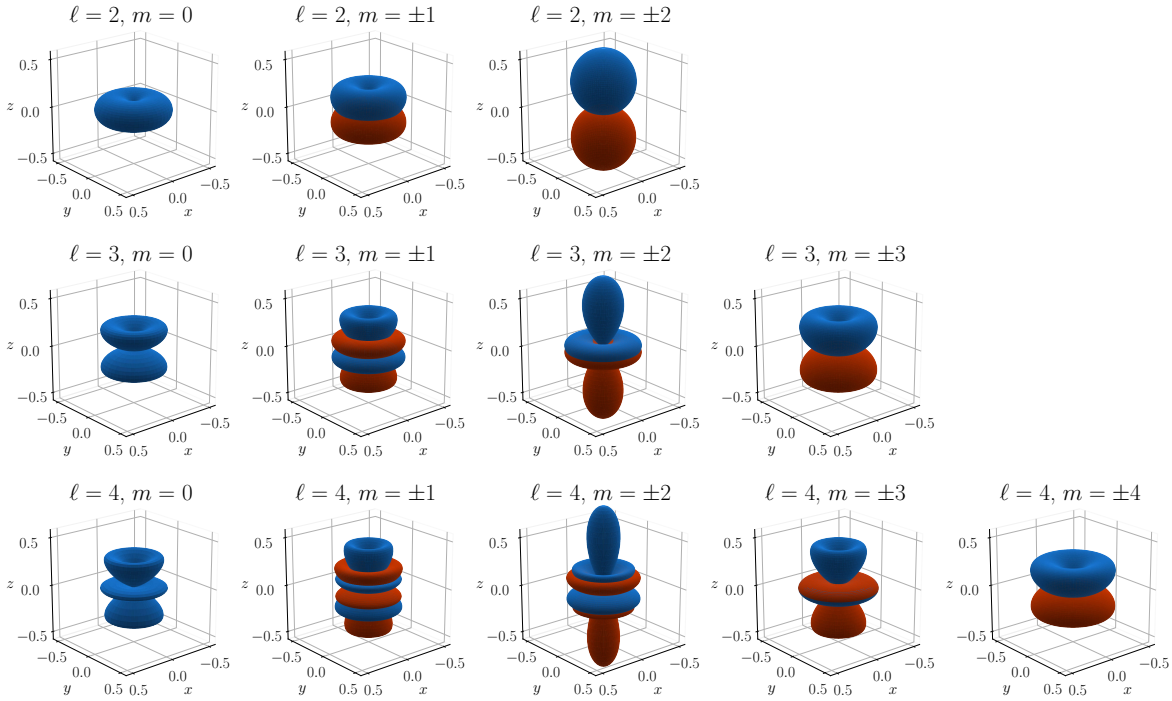

Figure 2.7: SWSH surface plots for $2 \leq \ell \leq 4$, $-\ell \leq m \leq \ell$ and $s = -2$. The distance of the surface from the origin indicates the absolute value of ${}^{s}Y_{\ell,m}$ from Eq. (2.42) in the angular direction (θ, ϕ). Blue surfaces represent $m \geq 0$, red surfaces $m < 0$.

The geometrical structure of the $s = -2$ SWSH, see Fig. 2.7, is consistent with the property of the GW to be quadrupolar, i.e. the structure does not allow any modes other than the $(2, \pm 2)$ modes to dominate. The $(2, \pm 2)$ modes are most efficient in radiating spherically GWs above and below the orbital plane. In addition, the structure of SWSH indicates that harmonics with positive/negative m-values have greater influence in directions with positive/negative z-values.

2.2.6 Source frames of reference

If we want to demonstrate that GWs from precessing BBHs contain features that are intrinsically a physical phenomenon and not just a coordinate artefact that can be resolved by transformation to another frame of reference, we need to explore frame transformation techniques. These techniques were initially introduced to simplify the time dependence of the modes and thus to simplify the modelling problem. In this chapter we are following definitions and explanations by Boyle et al. [31, 62]

As we have already seen in sec. 2.2.4, for precessing systems the orbital angular momentum $\vec{L}$ is no longer fixed in an inertial frame due to precession. The spins rotate, involving all three degrees of orbital rotational freedom, and the orbital plane wobbles during the inspiral. This means that in an inertial frame there is no fixed axis along which the radiation dominates. Energy emitted perpendicular to the orbital plane can be radiated in modes other

than the (2, ±2) modes, resulting in strong modulation of the amplitude and phase of each mode. This can be observed in the inertial frame from the *beat* pattern, see Fig. 2.8. The representation of the strain in a basis of SWSH has the advantage that transformations under rotations take a simple form. The modes in a second rotated frame $\tilde{h}_{\ell,m}$ can be calculated from the inertial frame modes $h_{\ell,m}$ via

$$\tilde{h}_{\ell,m}(t) = \sum_{m'} h_{\ell,m'}(t)\, \mathcal{D}^{(\ell)}_{m,m'}\left(R^{-1}(t)\right) , \tag{2.43}$$

where $\mathcal{D}^{(\ell)}$ are *Wigner matrices* [63] and R is the *rotor*, which can be expressed as an unit *quaternion* [62] and rotates the first set of basis vectors into the second.

We can define a *coprecessing frame* by applying a time-dependent rotation so that the orbital angular momentum $\vec{L}$ is always parallel to the z-axis of the coordinate system from which we measure the waveform. In this non-inertial frame the radiation is always strongest along the z-axis and the (2, ±2) modes dominate. The waveform in the coprecessing frame is analogous to that of a non-precessing system in an inertial frame, in the sense that the amplitude and phase modulations are absent [64].

To reduce further precession effects, another frame rotation can be applied in addition to the $\vec{L}$-orientation. In a *corotating frame* we align again the z-axis at each time step with $\vec{L}$ and additionally rotate the x-axis around the z-axis so that the separation vector between both BHs $\vec{n}$ is always along the x-axis. This is equivalent to applying a phase factor with the instantaneous orbital phase $\phi_{orb}(t)$, which is related to the orbital angular velocity by $\omega_{orb} = \mathrm{d}\phi_{orb}/\mathrm{d}t$, to the coprecessing frame modes [24]

$$h^{coro}_{\ell,m}(t) = h^{copr}_{\ell,m}(t)\, e^{im\phi_{orb}(t)} . \tag{2.44}$$

Here we denoted the strain in the coprecessing and corotating frame in the superscript. No superscript means that the inertial frame is used. Since $\omega_{GW} = 2\omega_{orb}$, as shown in sec. 2.2.3, we can define the orbital phase in terms of the GW phase. Here we use the average of the dominant (2, ±2) modes to calculate the orbital phase in Eq. (2.44):

$$\phi_{orb}(t) = \frac{1}{4}\left(\arg\left(h^{copr}_{2,-2}\right) - \arg\left(h^{copr}_{2,2}\right)\right) . \tag{2.45}$$

Since the corotating and coprecessing frames are only related by a phase factor, their amplitudes are equal $\left|h^{coro}_{\ell,m}(t)\right| = \left|h^{copr}_{\ell,m}(t)\right|$. However, the waveforms are no longer sinusoidal in the corotating frame and we cannot define a precise phase. However, the time evolution of the phase derivative is the dominant effect used to measure GWs, making this frame less useful for real world problems.

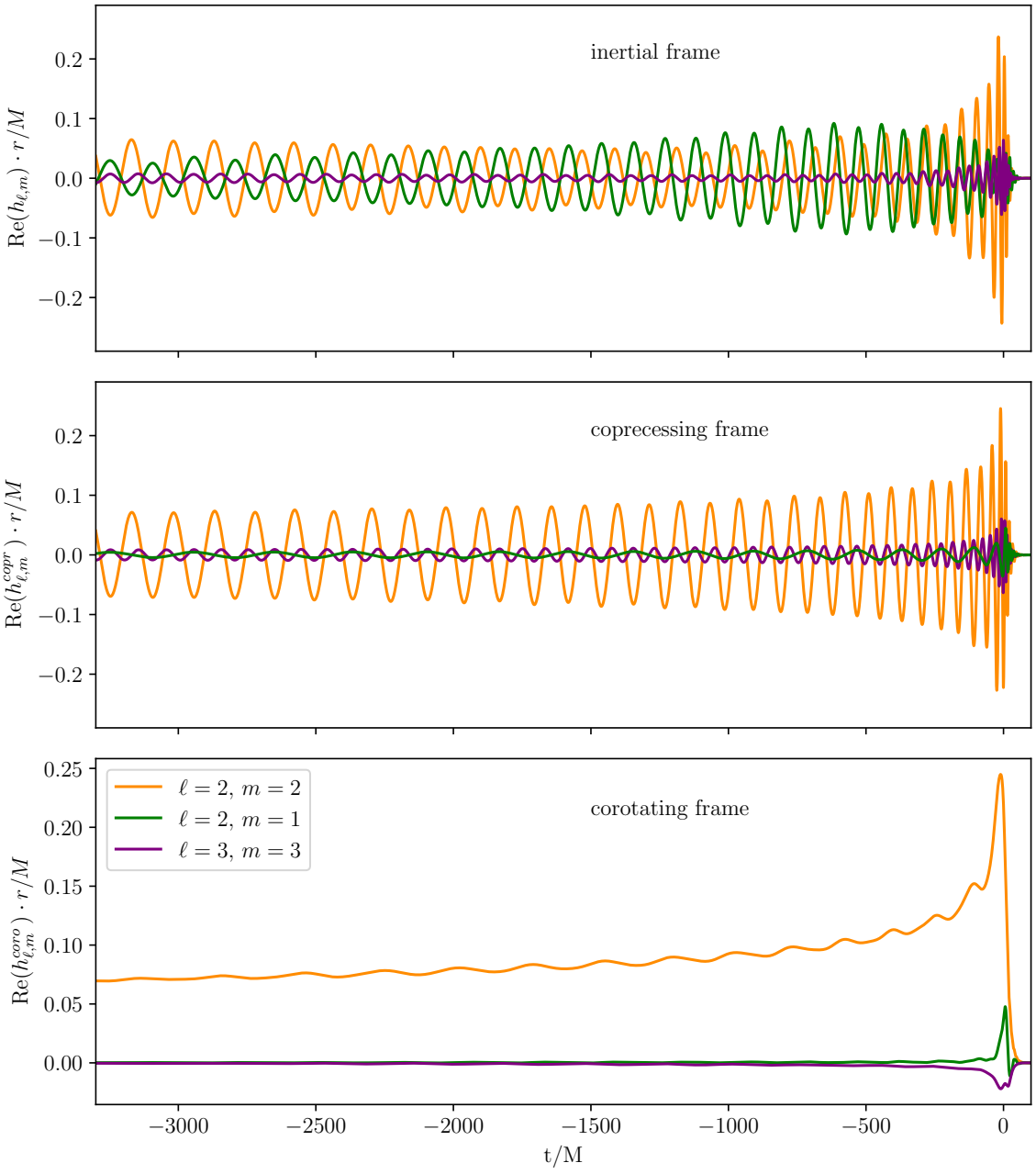

Figure 2.8: Real part of the (2, 2), (2, 1) and (3, 3) mode for a $\lambda = \{4, (-0.19, -0.6, 0), (-0.8, 0, 0)\}$ configuration defined at a reference time of $t_{ref} = -4300\,M$. Beat effects of the subdominant modes occur in the inertial frame. In the coprecessing frame the (2, 2) mode is the dominant one. Here, the fast phase evolution and the amplitude of the (2, 1) mode have been strongly suppressed by the frame rotation, while the (3, 3) mode remains similar. In the corotating frame, the modes no longer oscillate around zero and most of the precessing effects are removed. This figure has been modified based on Fig. 1 in Ref. [24].

Technically the two frame rotations described above are done by using the waveform itself without any knowledge of the spin dynamics of the system. Therefore, we use a mathematical concept that can be partly related to the orbital parameters in BBH systems, such as separa-

tion vector and orbital angular momentum evolution. The *waveform angular velocity vector* $\boldsymbol{\omega}$ is given by

$$\boldsymbol{\omega} = -\langle LL\rangle^{-1} \cdot \langle L\partial_t\rangle \,. \tag{2.46}$$

For $i, j \in \{x, y, z\}$ we define the matrix

$$\langle LL\rangle_{ij} = \sum_{\ell,m,m'} h^*_{\ell,m'} \,\langle \ell, m'|\hat{L}_i\hat{L}_j|\ell, m\rangle \, h_{\ell,m} \,. \tag{2.47}$$

The dominant eigenvector $\boldsymbol{V}_h$ of $\langle LL\rangle$ is called the *waveform's symmetry axis*. In addition we define the vector

$$\langle L\partial_t\rangle_i = \sum_{\ell,m,m'} \mathrm{Im}\left(h^*_{\ell,m'} \,\langle \ell, m'|\hat{L}_i|\ell, m\rangle \, \partial_t h_{\ell,m}\right) \,, \tag{2.48}$$

which according to Ref. [62] can be interpreted abstractly as a projection of the waveform's time derivative onto the rotational parts of the waveform and is equivalent to Eq. (2.34) [31]. Here we used a quantum-mechanical motivated bra-ket notation and set $\hbar = 1$. The states $|\ell, m\rangle$ are the same in position basis as the SWSH:

$$\langle x|\ell, m\rangle = {}^sY_{\ell,m}(\theta, \phi). \tag{2.49}$$

The angular-momentum operators $\hat{L}_i$ act on the states as

$$\hat{L}_z \,|\ell, m\rangle = m \,|\ell, m\rangle \tag{2.50}$$

$$\hat{L}_\pm \,|\ell, m\rangle = \sqrt{(\ell \mp m)(\ell \pm m + 1)} \,|\ell, m \pm 1\rangle \tag{2.51}$$

where $\hat{L}_\pm = \hat{L}_x \pm i\hat{L}_y$. In position basis the $\hat{L}_i$ are the same as in Eq. (2.36) [61]. The task now is to find the rotor $R(t)$, which describes a frame whose waveform angular velocity is $\boldsymbol{\omega}$. One can show that the rotor has to fulfil this differential equation [62]:

$$\boldsymbol{\omega} = 2\dot{R}R^* \,. \tag{2.52}$$

By setting physically motivated boundary conditions for the integration of this equation, we achieve that in this frame the z-axis is always aligned with $\boldsymbol{V}_h$ and the x-axis is always aligned with the BBH separation vector $\vec{n}$ by setting the (2, 2) phase to zero. In Ref. [62] it was shown that $\boldsymbol{\omega}$ and $\boldsymbol{V}_h$ are related to the separation vector $\vec{n} \sim \boldsymbol{\omega} - (\boldsymbol{V}_h \cdot \boldsymbol{\omega})\boldsymbol{V}_h$ and the orbital angular momentum $\vec{L} \sim (\boldsymbol{V}_h \cdot \boldsymbol{\omega})\boldsymbol{V}_h$. This means that we have found the rotor for the corotating frame and by neglecting the evolution of $\vec{n}$ also for the coprecessing frame. Finally, by using the quaternion notation of R, we can reduce the numerically expansive computation of the Wigner matrices in Eq. (2.43) at each time step to perform the frame rotation. The entire procedure described for this manipulation of the time-dependent modes for frame rotation methods is already implemented in the `scri` package [65]. An alternative

coprecessing frame is the *quadrupole-aligned* frame, which orients the coordinate system, such that the (2, ±2) modes are maximised. It was proposed by Schmidt et al. [64], but later in Ref. [66] it was shown that the quadrupole-aligned frame is equivalent to the waveform axis alignment technique just described when only the (2, ±2) modes are included.

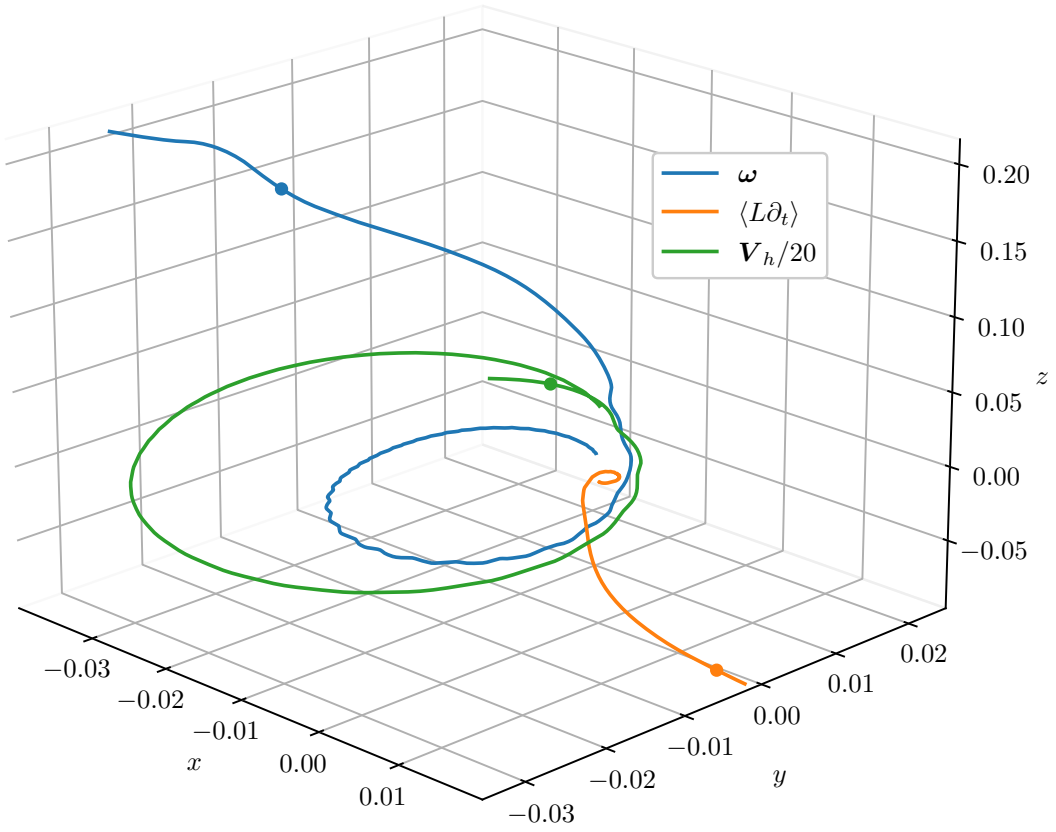

Figure 2.9: Trajectories of three vectors used to build source frames just from waveform quantities. The waveform of the same precessing system as in Fig. 2.8 is inserted in the definitions of the waveform angular velocity $\boldsymbol{\omega}$, the projection of the waveform's time dependence onto rotation $\langle L\partial_t \rangle$ and the waveform axis $\boldsymbol{V}_h$, which is just for visibility scaled by a factor of 1/20. The last 4300 M until merger are shown. The dot indicates the time of merger at $t = 0\,M$. The trajectories are smooth at first, then increasingly oscillating until the merger. The question of the physical meaning of these trajectories is not so easy to answer, but it is certainly worth getting a visual feeling for the mathematical constructions used to perform frame rotations. The plot is generated using functions implemented in the `scri` package [65].

To be more precise, it is useful to introduce two other source frames that are often found in the literature. The *conutating frame*, which is analogous to the copreccessing frame, and the *coorbital frame*, which is analogous to the corotating frame. The conutating and coorbital frames, grouped together as binary frames, are defined in terms of the orbital elements of the binary, such as the two individual spins, while the coprecessing and corotating frames, grouped together as waveform frames, are defined in terms of the angular velocity of the

waveform. Since `scri` uses the algorithm described in the paragraph above, and thus deals with waveform frames, we speak only of coprecessing and corotating frames, and have in mind the analogy of aligning the coordinate axis with the orbital elements of the binary.

Notation	Waveform frame	Binary frame	Axis alignment
$h(t)$	Inertial	Inertial	$\hat{x} \parallel \vec{n}(t_{ref}), \quad \hat{y} = \hat{x} \times \hat{z}, \quad \hat{z} \parallel \vec{L}(t_{ref})$
$h^{copr}(t)$	Coprecessing	Conutating	$\hat{x} \parallel \vec{n}(t_{ref}), \quad \hat{y} = \hat{x} \times \hat{z}, \quad \hat{z} \parallel \vec{L}(t)\ \forall t$
$h^{coro}(t)$	Corotating	Coorbital	$\hat{x} \parallel \vec{n}(t)\ \forall t, \quad \hat{y} = \hat{x} \times \hat{z}, \quad \hat{z} \parallel \vec{L}(t)\ \forall t$

Table 1: Different source frames explained in this chapter. The reference time t_{ref} is an arbitrary but fixed time point before the merger. Note that the waveform frames are determined from the waveform alone, but are analogous to the binaries frames, which are defined with respect to the BBH orbital elements. The definitions follow Ref. [31].

2.2.7 Reference epoch

The waveform and the spin dynamics of a precessing BBH system strongly depends on a parameter f_{ref}, which is a reference frequency at which the spin directions are specified. The strong dependence is due to the fact, that in precessing systems the directions of the BH spin angular momenta change with time. As already seen in the first PN order in Eq. (2.31) the frequency, be it a GW or an orbital frequency, depends on time, i.e. analogously we can define a corresponding reference time t_{ref}. The generic term is called *reference epoch*. As there is currently no convention on how to set the reference epoch for waveform generation, e.g. using an angular or ordinary frequency or a point in time, one has to be careful how the waveform models define the reference epoch. One reason why there is no standard convention is that different waveform models use different physically and mathematically motivated approaches to build the basic framework of the model, as will be discussed in sec. 2.4, making it difficult to find a standardised convention.

As an example, we explain how the `NRSur7dq4` model defines the reference epoch and how to find a mapping between reference frequency and time. To generate a waveform with `NRSur7dq4` the spins can be defined at a reference frequency, here an ordinary GW frequency in units of cycles per total mass M. The relation between an angular frequency ω and ordinary frequency f in geometrized units is given by

$$\frac{\omega}{\mathrm{rad/M}} = 2\pi \frac{f}{\mathrm{cyc/M}}\,. \tag{2.53}$$

We can get the GW phase behaviour $\phi_{GW} = \arg(h)$ from a waveform $h(t)$ generated from a spin configuration at some arbitrary but fixed reference epoch, for example the `NRSur7dq4` default case $t^{\mathbf{0}}_{ref} = -4300\,M$ [24]. Calculating the time derivative of the phase $\dot{\phi}_{GW}$, which

is in units of radians per M since the phase is in units of radians, and using $\omega = \dot{\phi}$ gives

$$\frac{f_{GW}(t)}{\text{cyc/M}} = \frac{1}{2\pi}\,\frac{\dot{\phi}_{GW}(t)}{\text{rad/M}}\,, \tag{2.54}$$

which is exactly the reference frequency that `NRSur7dq4` wants to use. We take advantage of this relation to find an algorithm that maps an user given reference time $t^{\mathbf{1}}_{ref}$ to the wanted reference frequency $f^{\mathbf{1}}_{ref}$:

0. Specify intrinsic parameters $\lambda^{\mathbf{1}} = \{q, \vec{\chi}_1, \vec{\chi}_2\}$ and a reference time $t^{\mathbf{1}}_{ref}$.
1. Generate a time-domain waveform $\text{GW}^{\mathbf{0}}$ with $\lambda^{\mathbf{1}}$ at arbitrary $t^{\mathbf{0}}_{ref}$ or $f^{\mathbf{0}}_{ref}$.
2. Calculate the $\text{GW}^{\mathbf{0}}$ phase-time map via $\phi_{\text{GW}^{\mathbf{0}}}(t) = \left(\arg\left(h^{copr}_{2,-2}(t)\right) - \arg\left(h^{copr}_{2,2}(t)\right)\right)\Big/2$, the average of the argument of the two most dominant modes in the coprecessing frame.
3. Substitute $\dot{\phi}_{\text{GW}^{\mathbf{0}}}(t = t^{\mathbf{1}}_{ref})$ in Eq. (2.54) to get $f^{\mathbf{1}}_{ref}$ in units of cyc/M.

An implementation in `Python` is given in appendix B. We can use the calculated $f^{\mathbf{1}}_{ref}$ and the same $\lambda^{\mathbf{1}}$ to generate a new waveform $\text{GW}^{\mathbf{1}}$. We find that $\text{GW}^{\mathbf{1}}$ is a good approximation of the waveform produced by the configuration λ at the given reference time, if $t^{\mathbf{1}}_{ref} \lesssim -100\,M$. The approximation holds for a choice of $t^{\mathbf{1}}_{ref}$ in the inspiral regime and for small mass ratios, because the frequency-time map of $\text{GW}^{\mathbf{0}}$ and $\text{GW}^{\mathbf{1}}$ is equal up to PN order 3/2. To prove this, one can extend Eq. (2.29) to this order. Therefore the reader can explore Eq. (3.20) and (3.21) in Ref. [45] and find out that ω_{orb} is a function of only the mass ratio q, the total mass M and the effective spin χ_{eff}. Since M is scaled out and $q(t^{\mathbf{0}}_{ref}) = q(t^{\mathbf{1}}_{ref})$ and $\chi_{\text{eff}}(t^{\mathbf{0}}_{ref}) = \chi_{\text{eff}}(t^{\mathbf{1}}_{ref})$, we have shown that the frequency-time map of $\text{GW}^{\mathbf{0}}$ can be used to figure out any reference time $t^{\mathbf{1}}_{ref}$ to generate $\text{GW}^{\mathbf{1}}$.

	$\frac{f_{GW}}{\text{cyc/M}}$	$\frac{f_{orb}}{\text{cyc/M}}$	$\frac{\omega_{GW}}{\text{rad/M}}$	$\frac{\omega_{orb}}{\text{rad/M}}$
$f_{GW}\Big/\text{cyc/M}$	1	$\frac{1}{2}$	2π	π
$f_{orb}\Big/\text{cyc/M}$	2	1	4π	2π
$\omega_{GW}\Big/\text{rad/M}$	$\frac{1}{2\pi}$	$\frac{1}{4\pi}$	1	$\frac{1}{2}$
$\omega_{orb}\Big/\text{rad/M}$	$\frac{1}{\pi}$	$\frac{1}{2\pi}$	2	1

Table 2: Conversion table for reference frequencies in different units. It should be read as the quantity on the left multiplied by the conversion factor is equal to the quantity on the top. For example, the third row and first column is Eq. (2.54). The conversion factors do not change in SI units, but the unit of an ordinary frequency is Hz and the unit of an angular frequency is rad/s.

The inverse algorithm, i.e. giving a reference frequency in cyc/M and obtaining a reference time in units of M, is analogous by replacing t_{ref} with f_{ref} in the above enumeration. If the waveform model defines the reference epoch in another way, step 3 can be adjusted by picking the right conversion factor in Table 2.

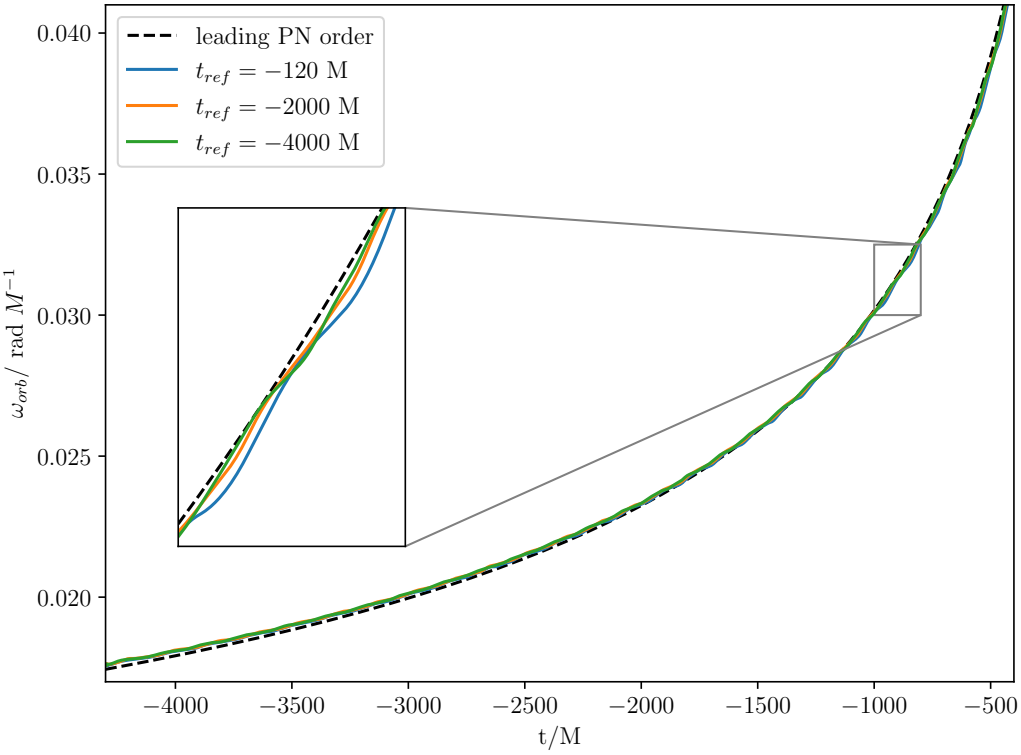

Figure 2.10: Frequency-time map for $\lambda = \{q = 2, \vec{\chi}_1 = (0.5, 0.2, 0.5), \vec{\chi}_2 = (-0.3, 0.1, 0.5)\}$ configurations defined at different reference times. The black dashed line is the leading PN order expression defined in Eq. (2.31). The solid lines are calculated from the waveforms via the time derivative of Eq. (2.45). Since q and χ_{eff} are equal for all configurations $\omega_{orb}(t)$ is up to $\text{P}^{3/2}\text{N}$ order equal. Higher order corrections include in-plane spin effects and explain the small oscillations, which can be seen in the inset.

2.3 Detecting gravitational waves

In the previous chapter, we saw that the amplitude of GWs decays linearly with the distance from the source, that the GW effect is small and that there is a wide range of GW-emitting sources, making their detection very difficult. Despite all the challenges, physicists have made considerable efforts to observe GWs with state-of-the-art instruments.

2.3.1 History

The first attempt to detect GWs with aluminium bar detectors was made by Joseph Weber in the 1960s [67–70], but his claimed detection was later found to be inaccurate [71]. In 1974 Russell Hulse and Joe Taylor discovered the binary system PSR 1913+16 composed of a NS and a pulsar [72]. After 14 more years of observations and measurements of the binary's orbit, it was confirmed that the distance between the two objects was decreasing over time at exactly the rate predicted by GR [73]. This indirect detection was the first clear evidence for the existence of GWs and motivated physicists to detect them directly.

On 14 September 2015, the LIGO made the first direct observation of a GW, named GW150914. The LIGO and Virgo research groups announced their groundbreaking discovery in 2016 [2] which led to the awarding of the Nobel Prize in Physics in 2017 to Rainer Weiss, Barry Barish and Kip Thorne. The GW signal was emitted due to the collision of two BHs, with masses of 36 $M_\odot$ and 29 $M_\odot$, which merged and became a BH with a mass of 62 $M_\odot$. This event resulted in the emission of GWs with a total energy of 3 $M_\odot$. Since then, multiple groups have reported hundreds of observations, including BBHs, NSBH and BNS mergers, by analysing the publicly available data [74, 75] from four observation periods, with the fourth observation run still ongoing. The data was recorded by three Earth-based detectors: LIGO Livingston (Louisiana, USA), LIGO Hanford (Washington, USA) [76], and Virgo at Santo Stefano a Macerata (Pisa, Italy) [77]. Towards the end of the third observation period, a fourth detector, KAGRA at Kamioka (Gifu, Japan) [78], joined the network. Due to its size, the fifth current operating detector, GEO 600 in Sarstedt (Hanover, Germany), is not expected to reach a level of sensitivity that will allow regular GW detections. However, it plays an important role as a test bed for new technologies. Once proven effective, these technologies will be integrated into other detectors. All of the detectors are laser interferometers with scales up to 4 km. A brief introduction to them will be provided in sec. 2.3.3.

Using radio telescopes to analyse pulsars is another approach to detecting GWs. Pulsars are rapidly rotating NSs that emit radio waves in sweeping patterns, similar to lighthouses. PTAs track these signals by using millisecond pulsars to detect the small perturbations that GWs cause in the signal's travel time. PTAs focus on detecting supermassive BBHs, galaxy mergers, and poorly understood sources of GWs, such as the primordial background of GWs from cosmic inflation or cosmic strings. Three large global projects, North American Nanohertz Observatory for Gravitational Waves [9, 79–84], Australian Parkes PTA [10, 85, 86], and European PTA [8, 87–91], collect data from various radio telescopes. The first evidence of a stochastic ultra-low-frequency GW background, including the Hellings-Downs curve [92], was disclosed in the 15-year data release on 29 June 2023.

2.3.2 Motivation for gravitational wave measurements

Over the last few centuries, various types of telescopes that use electromagnetic waves such as gamma rays, radio waves, or visible light have been utilised to "see" the Universe. Thus, the recent era of detecting GWs is often referred to as "listening" to the Universe to highlight the relevance and novelty.

All observed CBCs to date have one thing in common, the merger of two compact objects with a stellar origin. The life cycle of a star involves several phases. Stars begin their journey as clouds of gas and dust that collapse to form protostars. Once nuclear fusion starts, stars transition into a phase characterised by the generation of energy. Depending on their mass, stars can conclude their lives as white dwarfs or explode in supernovae, scattering heavy elements across the Universe and resulting in a BH or NS [93]. By analysing GWs from merging processes we can learn something about the evolution and demography of BHs and NSs. The most popular formation channels for BBHs are the isolated and the dynamical channels [94]. The isolated channel, where two massive binaries complete their life cycle, gives rise to aligned-spin BBHs. While the dynamical channel, where BBHs form in dense clusters, leaves various imprints on the mass, orbital properties and especially the spins of two BHs, with a chance to form precessing BBHs. Measuring the distribution of aligned and mis-aligned BBHs is an active area of research to determine which channel is more likely. In addition, the recoil of the BH formed after the merger is of great astrophysical interest, since the recoil can exceed the escape velocity of even the most massive galaxies in the Universe [95, 96].

In this paragraph we briefly list some more astrophysical, cosmological, fundamental physical and quantum physical reasons why it is important to measure GWs, and give some references for further reading. GW measurements of binaries containing a NS, such as GW170817, the first GW event ever detected caused by the merger of two NSs [6], can tell us something about the interior structure of NSs, since we are dealing with quantum chromodynamics at ultra-high densities with exotic states of matter [97]. We can learn about the NS equation of state or the nucleosynthesis of elements [11]. In addition, interesting astrophysical GW sources could be detected, such as core-collapse supernovae [20], isolated NSs [98], exotic objects [99], or white dwarf binaries [100]. Although GR is the best current description of gravity, it is likely to be an incomplete theory because it is incompatible with quantum mechanics. One might therefore expect GR to break down in strong field regimes. GWs from a BH merger are an ideal test of GR [14, 101]. Cosmologically, GWs are of scientific interest because the Universe became transparent to electromagnetic waves only 380 million years after the Big Bang. With GWs, we can look further back in time and search for primordial BHs [15, 16], find out about the Hubble constant [17, 18] or about inflation [19].

2.3.3 Detectors

In principle, all GW detectors currently in operation are highly advanced Michelson interferometers. These L-shaped interferometers split a laser beam into two perpendicular beams. In each arm, one beam passes an input test mass that acts as a mirror. It then travels a long distance, e.g. 4 km for the advanced LIGO design [102], before being reflected by the output test mass. On its return journey, a significant proportion of the light is again reflected by the input test mass, increasing the time the light takes to travel through the arms. The two test masses effectively form a large Fabry-Pérot cavity. As the light passes through the input test mass, it recombines and interacts with the light from the opposite arm. To generate the read-out, a photodiode captures the beam at the output port. These interferometers are sensitive in a 10 Hz to kHz band, where the main sources are CBCs, supernovae and continuous waves from spinning NSs.

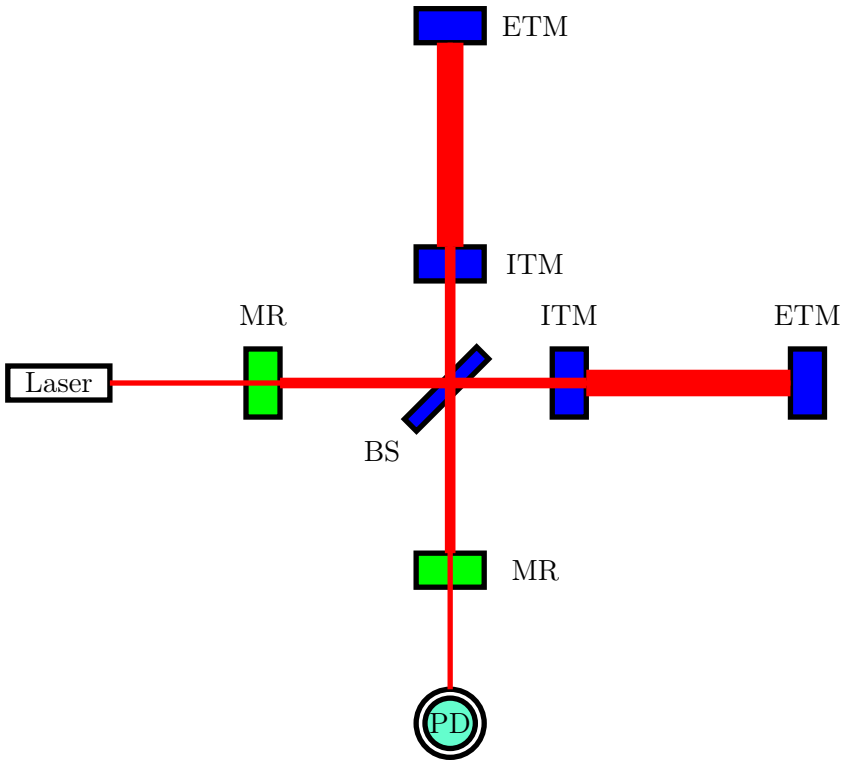

Figure 2.11: Simplified optical configuration of the advanced LIGO interferometer design. The main components are a Nd:YAG laser, 50/50 beamsplitter (BM), input test masses (ITM), end test masses (ETM), photodiode (PD) and some refined laser modulation and power recycling (MR) constructions. The thickness of the beams indicates the different effective laser powers of 125 W, 5.2 kW and 750 kW. The figure has been modified based on Fig. 1 in Ref. [102].

As illustrated in Fig. 2.2, the distance between the two freely-floating test masses in each arm of the interferometer changes if a GW passes through it. We assume a GW travelling in the

z-direction, linearly polarised with $h_+ = h_+(t - z)$ and $h_\times = 0$. The proper distance change ΔL between two masses separated by L along the optimally located arm on the x-axis is

$$\frac{\Delta L}{L} = \frac{h_+}{2} \tag{2.55}$$

in first order [35]. This change in length is equivalent to a change in laser frequency in each arm. By splitting the same laser beam into two, the frequency difference and the resulting phase difference on recombination can be used to monitor the GW amplitude.

We see from Eq. (2.55) that to increase the impact of a GW on the detector, one can extend the length L of the arms, hence the current detectors being on a scale of kilometres. Alternatively, the detected signal can be amplified by boosting the power of the laser circulating within the arms by implementing a Fabry-Pérot cavity and power recycling mirrors. The interferometer design noise is determined by different noise sources summarised in Table 3. The detectors have been designed so that these noises are extremely quiet [103]. This is achieved by pre-stabilising the laser, implementing damping techniques, and using many other refined constructions. Using a minimum of two GW detectors is crucial to enhance the significance of detections. Multiple detectors in different locations improve accuracy, ensure astrophysical validity, and allow better source localisation in the sky.

Noise sources	Description
Quantum noise	Photon fluctuations due to Heisenberg uncertainty
Thermal noise	Molecular motion-induced mirror vibrations
Seismic noise	Ground vibrations managed with isolation systems
Gravity gradients	Variations in local gravitational field
Gas noise	Residual gas interactions with mirrors and laser light in vacuum
Laser noise	Small variations in the laser intensity and frequency
Coating noise	Scattering and absorption from coating imperfections

Table 3: Examples of noise sources in the advanced LIGO design [103].

Numerous upgrades and extensions to the existing network of ground-based GW detectors are planned. In the near future, a third copy of the advanced LIGO detector design will be built in India [104]. More upgrades to the LIGO detectors, known as A+, A$^\sharp$ and LIGO Voyager, will include advances in quantum squeezing technologies, larger test masses, increased laser power, changes in laser frequency, cryogenic operation and many other refinements [105]. In addition, completely new ground-based detectors are being planned for operation in the

mid-2030s. The Einstein Telescope (ET) [106] in Europe will be an underground triangular interferometric detector with a 10 times better sensitivity than the current instruments. The Cosmic Explorer (CE) [107] in the United States will use an arm length of 40 km. The Neutron Star Extreme Matter Observatory (NEMO) in Australia will be an interferometer optimised for the study of nuclear physics with merging NSs [108]. Three space-based projects are being developed to overcome the low-frequency limitations of Earth-based observatories. The Laser Interferometer Space Antenna (LISA) [109] is a collaboration between ESA, NASA and the LISA Consortium. LISA will consist of three satellites in heliocentric orbit using time delay interferometry with an arm length of $2.5 \cdot 10^9$ m to detect GWs in the range of about 0.1 mHz to 1 Hz. Following successful technology testing with LISA Pathfinder [110], the LISA mission is planned for launch in 2037. DECIGO is a proposed Japanese GW detector that will be based in space. The detector will be triangular in shape, with each side measuring 10^6 m [111]. Another proposed space-based observatory is the TianQin [112] detector, consisting of three satellites with a reduced arm length of 10^5 m orbiting the Earth.

2.3.4 Data analysis

As seen in the previous chapter, the detector's sensitivity is limited by different noise sources. To achieve optimal sensitivity, advanced data analysis techniques are necessary. We can express the output of the detector $s(t)$ as a linear combination of the noise $n(t)$ and a potentially additive GW signal $h(t)$:

$$s(t) = n(t) + h(t)\,. \tag{2.56}$$

We assume that the noise is stationary and Gaussian with a mean of zero. In reality, this is an approximation, as noise characteristics slowly change over time and there are small non-Gaussian noise disturbances known as *glitches*. However, the pace of noise change is slow compared to the typical duration during which CBC signals are observable [113]. Furthermore, multiple methods have been developed to eliminate glitches from the data [114].

We can construct the meaningful *signal-to-noise ratio* (SNR), denoted by $\rho(t)$, which allows us to measure the importance of the signal against the background noise [115, 116], as

$$\rho(t) = \frac{\langle s, h\rangle}{\sqrt{\langle h, h\rangle}}\,. \tag{2.57}$$

Once the SNR surpasses a threshold determined by search configurations, the search may have potentially detected a signal. Here we used the *noise-weighted inner product* between to functions $a(t)$ and $b(t)$ given by

$$\langle a, b\rangle\,(t) = 4\mathrm{Re}\left[\int_0^\infty \mathrm{d}f\,\frac{\tilde{a}^*(f)\,\tilde{b}(f)}{S_n(f)}\right]\,, \tag{2.58}$$

where $\tilde{a}(f)$ is defined using the common definition of Fourier transformation in signal processing

$$\tilde{a}(f) = \mathcal{F}[a(t)] = \int_{-\infty}^{\infty} \mathrm{d}t\, a(t) e^{-2\pi i t f}\,, \tag{2.59}$$

where f is an ordinary frequency. The one-sided *power spectral density* can be calculated from pure noise $n(t)$ and a finite time interval of length T as [117]

$$S_n(f) = \frac{2}{T}\overline{|\tilde{n}(f)|^2}\,, \tag{2.60}$$

where the overline denotes the average. The *amplitude spectral density* is the square root of the power spectral density and has units of $\mathrm{Hz}^{-1/2}$.

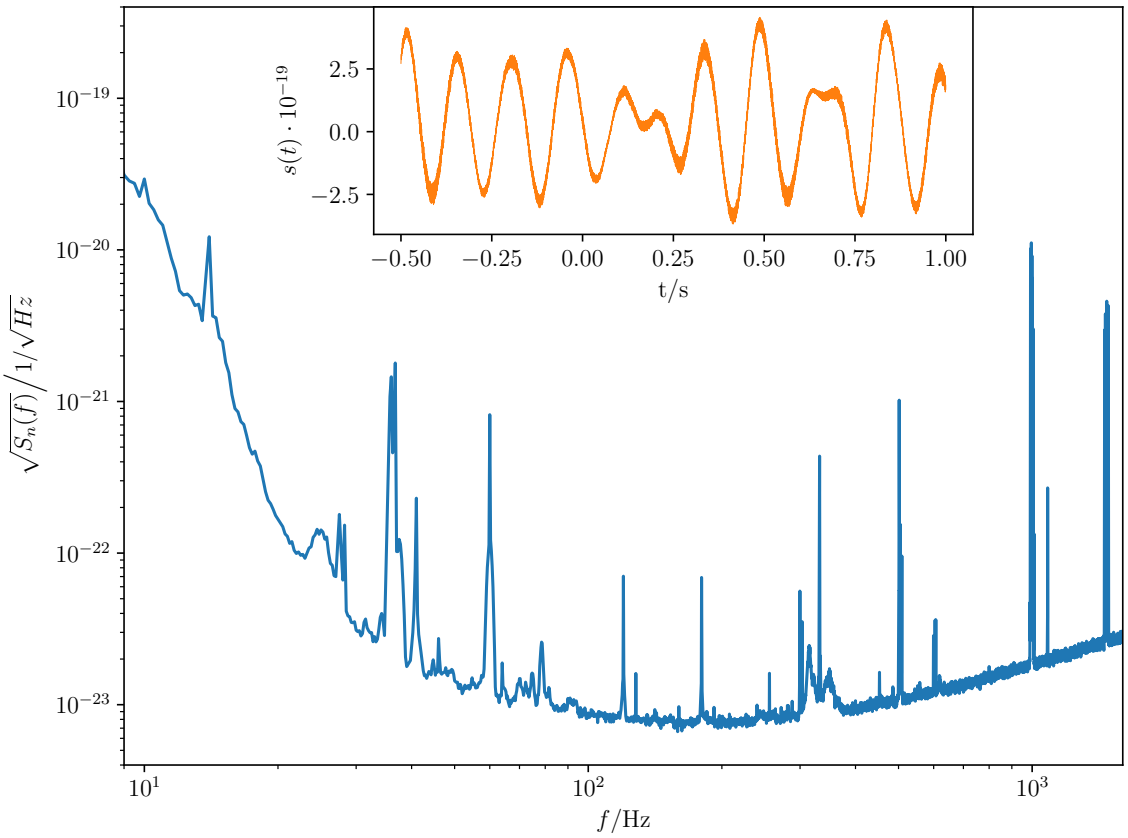

Figure 2.12: Amplitude spectral density $\sqrt{S_n(f)}$ of the raw LIGO Hanford detector data calculated from a time interval of GPS time 1126258950 to 1126259462 (512 s before until 14 September 2015 at 09:50:45 UTC, the time given in Ref. [2] as the start time of the first ever detected event GW150914). The data were divided into overlapping 4 s chunks, each spaced by 2 s. A Tukey window was applied to each chunk and then fast Fourier transformed. Finally the power spectrum from all the chunks was Welch averaged. The inset shows the raw detector time series $s(t)$ with the GW150914 signal $h(t)$ from 0 s to around 0.5 s, which is not visible to the naked eye without any further data analysis techniques such as whitening or bandpassing [116].

The first step in data analysis is to correlate the observed data with a set of template waveforms representing different possible signals. This process identifies potential events and is called *matched filtering*. In a matched filter search, the unknown finite set of signal parameters $\theta \in \mathbb{R}^n$ is not known in advance. The optimal detection statistic would be obtained by maximising the *likelihood ratio* $\Lambda(s|\theta)$ over all unknown parameters by integrating $\Lambda(s|\theta)$ over these parameters. Assuming stationary and Gaussian detector noise, we can write the likelihood ratio as [117]

$$\Lambda(s|\theta) = \exp\left(-\frac{1}{2}\left\langle s - h(\theta), s - h(\theta)\right\rangle + \frac{1}{2}\left\langle s, s\right\rangle\right) . \tag{2.61}$$

The related well-known *Fisher information* matrix $F_{ij}[h] = \langle \partial h/\partial\theta_i, \partial h/\partial\theta_j\rangle$ is another strong analytical framework for measuring uncertainties for GW observations [118]. Various independent search pipelines already contain all the algorithms needed to detect signals in the data. Just to name a few examples, we have `PyCBC` [119], `GstLAL` [120] or `MBTA` [121].

Once a candidate event is detected, *parameter estimation* becomes crucial and further source characterisation is performed using *Bayesian inference* [117]. This involves using stochastic sampling techniques to obtain estimates of the system's binary intrinsic and extrinsic parameters. `Bilby` [122], `LALinference` [123] and `PyCBC Inference` [124] are one of the most popular software packages for parameter estimation.

2.4 Modelling gravitational waves

Matched filtering and parameter estimation are powerful tools for finding and characterising known signals in noisy data. However, these methods are critically dependent on the accuracy of the waveform model used to predict GWs. Although analytical expressions to describe the GW radiation from two merging BHs have been developed in the previous chapters, our formulae are based on approximations such as assuming no eccentricity of orbits, small mass ratios, or ignoring dynamical friction due to astrophysical environments around BHs. In this chapter we take a brief look at how to solve the full EFE numerically and at the various approximate waveform models that have been established over the years. We can categorise them into three main waveform families that are widely utilised: *effective-one-body* (EOB), *phenomenological*, and *surrogate* waveforms. Most waveform models are included in `LALSuite` [125], the LIGO algorithm library for GW analysis routines.

2.4.1 Numerical relativity

For astrophysically interesting systems such as BBHs no exact analytical solution for the underlying spacetime metric is known. A first approach is to use perturbative methods. The expansion parameter in PN can be chosen as the ratio of the characteristic velocity of the BHs to the speed of light. However, when the BHs are about to merge, the expansion parameter

is no longer small, since the BHs are moving at about half the speed of light. Similarly, BH perturbation theory can only be used to describe the ringdown of the remaining BH after the merger by describing the ringdown morphology with an infinite sum of damped sinusoids, called *quasi-normal modes*, around the final Kerr BH state [126]. All perturbative methods break down in the strong field regime near the BH merger, and full numerical simulation of the EFE is the only way forward. This research field is known as *numerical relativity* (NR).

Realistic astrophysical computer simulations must solve the EFE and the associated hydrodynamic equations in a time-dependent manner without special symmetry assumptions. To realise this on a computer, it is necessary to rewrite the underlying equations. We are following Ref. [127] to briefly describe the NR basics. Ref. [128] is recommended for a quick read. In NR the (3+1)-decomposition, which divides a four-dimensional manifold into three-dimensional space-like hypersurfaces $\sum_t$, is used for the EFE reformulation. The spacetime metric $g_{\mu\nu}$ is thereby divided into a purely spatial metric γ_{ij}, a lapse-function α and a shift-vector β_i:

$$g_{\mu\nu} = \begin{pmatrix} -\alpha^2 + \beta_i\beta^i & \beta_i \\ \beta_i & \gamma_{ij} \end{pmatrix} . \tag{2.62}$$

The lapse-function α describes the difference between the coordinate time t and the proper time τ of a particle, i.e.

$$\mathrm{d}\tau^2 = \alpha^2(t, x^j)\,\mathrm{d}t^2 . \tag{2.63}$$

The shift-vector measures how the coordinates on the space-like hypersurface $\sum_t$ are shifted when the particle moves an infinitesimal time step further $\sum_{t+\mathrm{d}t}$, i.e.

$$x^i_{t+\mathrm{d}t} = x^i_t - \beta^i(t, x^j)\,\mathrm{d}t \tag{2.64}$$

By inserting this ansatz for the metric into the EFE, one can reformulate the equations into a system of first-order differential equations, the ADM equations [129], named after its authors Richard Arnowitt, Stanley Deser and Charles W. Misner. Since the ADM equations are not numerically stable, i.e. small numerical perturbations could build up exponentially, one must rewrite them using a conformal transformation of the metric. This transformation is known as Baumgarte-Shapiro-Shibata-Nakamura-Oohara-Kojima (BSSNOK) reformulation [130, 131]. It turns out that BSSNOK is well-posed and stable. The algorithm requires the initial hypersurface $\sum_0$ specified by the user and then iteratively calculates in time intervals $\mathrm{d}t$ the dynamic time evolution of the system.

There are different methods for extracting the strain h from a NR simulation. One common method is to use the complex Weyl tensor component Ψ_4 [132], which is related to the strain via

$$\Psi_4 = -\ddot{h}_+ + i\ddot{h}_\times = -\ddot{h} . \tag{2.65}$$

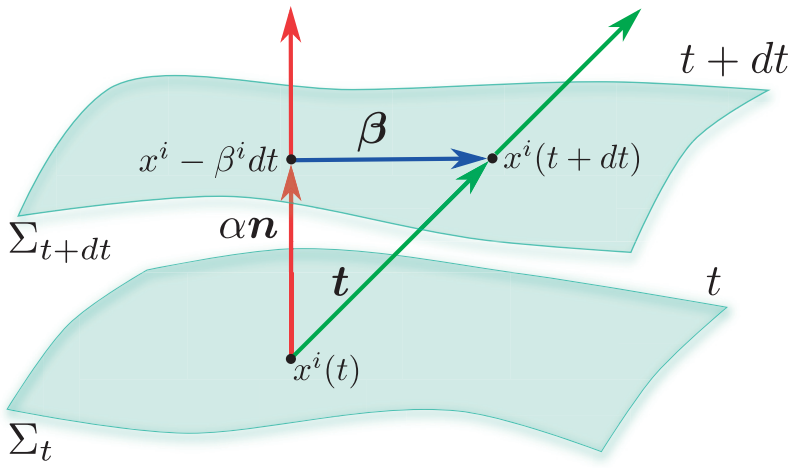

Figure 2.13: Visualisation of the (3+1) decomposition. The key concept is the decomposition of spacetime into constant-time hypersurfaces $\sum_t$ and $\sum_{t+\mathrm{dt}}$. The four-vector $\boldsymbol{t}$ indicates the time evolution and can be divided into a space-like component, represented by the spatial four-vector $\boldsymbol{\beta}$, and a time-like component $\alpha \boldsymbol{n}$, where $\boldsymbol{n}$ is a time-like unit vector to the hypersurface. The lapse α measures the proper time between neighbouring surfaces. The components of the shift-vector β^i measure the coordinate shift from one surface to the next. The illustration is taken from Fig. 7.1 in Ref. [127].

The measurement of Ψ_4 is more accurate than measuring small perturbations on a flat background. Analogous to Eq. (2.40) we can expand the Weyl scalar in a basis of SWSH:

$$\Psi_4 = \sum_{\ell=2}^{\infty} \sum_{m=-\ell}^{\ell} \psi_{\ell,m}(t,r) \cdot {}^{-2}Y_{\ell,m}(\theta,\phi)\,. \tag{2.66}$$

Following [133], the $h_{\ell,m}$ modes can then be obtained by performing a double time integration of Ψ_4

$$h_{\ell,m}(t) = \int_{-\infty}^{t} \mathrm{d}t' \int_{-\infty}^{t'} \mathrm{d}t'' \psi_{\ell,m}(t) + A_{\ell,m} t + B_{\ell,m}\,, \tag{2.67}$$

where we scaled out the explicit dependence on the distance from the origin r with the same argument as in sec. 2.2.5. The integration constants $A_{\ell,m}$ and $B_{\ell,m}$ can be obtained via a fitting procedure by the imposition of some physical condition, e.g. that the strain should tend to zero after the ringdown. However, it turns out that a small numerical error in Ψ_4 can be magnified by integrating. These numerical errors cause nonlinear drifts in the waveform. A common technique to avoid this effect, is to go in the Fourier domain [134]. Therefore we Fourier transform the $\psi_{\ell,m}(t)$ via Eq. (2.59) and apply a step filter of the following form

$$\tilde{h}^{filtered}_{\ell,m}(f) = \begin{cases} -\tilde{\psi}_{\ell,m}(f)/\omega^2\,, & \omega \geq \omega_0 \\ -\tilde{\psi}_{\ell,m}(f)/\omega_0^2\,, & \omega < \omega_0 \end{cases}\,, \tag{2.68}$$

where ω_0 is the lowest frequency expected to be physical. Note the relationship of the angular

frequency ω to the ordinary frequency via $\omega = 2\pi f$. Finally we inverse Fourier transform the $\tilde{h}^{filtered}_{\ell,m}(f)$ to go back in the time domain. Various other filters methods have been developed [135, 136], e.g. a smooth transition near ω_0.

Although NR is the most accurate technique to solve the EFE, NR encounters the issue of extremely high computational costs, which renders it impractical for generating thousands of waveforms for parameter estimation. For comparison, the surrogate package `NRSur7dq4` quickly generates waveforms within milliseconds for individual cases, whereas NR can take several weeks or even months. Factors such as longer waveforms, higher resolution, method selection or initial parameters can affect the timescale. As a result, only a small number of NR datasets, in the order of thousands, are available. To name just a few NR codes dealing with the BBH problem and associated catalogues of publicly available simulations, we have the `SpEC` code [137] developed by the Simulating eXtreme Spacetimes (SXS) collaboration [52], `MAYA` [53] or `BAM` [54, 138].

2.4.2 Phenomenological waveform family

The phenomenological waveform-family was initially introduced in Ref. [139]. Essentially, their technique aligns the analytical PN-waveform, which describes the inspiral phase, with the more precise NR-waveform in the merger phase, leading to a finite set of hybrid waveforms [136]. These hybrid waveforms are then fitted to a parameterised model based on the phenomenology of the waveform, which can subsequently be correlated with the actual physical characteristics of the binary system. The generated model is fast to evaluate, highly accurate and usually suitable for frequency domain calculations. Several models from the phenomenological family have been developed over the past two decades. One well-known example is the non-precessing model `IMRPhenomD` [140], which was instrumental in detecting GW150914. The prefix "IMR" denotes that the model encompasses the entire inspiral-merger-ringdown and the postfix "D" indicates its version number. Subsequent versions included additional effects, such as higher modes and precession [141–146]. The latest phenomenological waveform model is called `IMRPhenomXO4a` [147]. In this frequency domain model the dominant mode asymmetry is already included [32]. It should be mentioned here that in some future work it is definitely worthwhile to investigate the accuracy of `IMRPhenomXO4a` with a modelling of the phenomenology of mode asymmetries in the time domain, which we will describe in sec. 3. The reader interested in building a phenomenological time-domain model can have a look into Ref. [148–150].

2.4.3 Effective-one-body waveform family

EOB waveforms, introduced in Ref. [151], provide a comprehensive model for GWs and cover the inspiral, merger and ringdown regime. This formalism maps the BBH system to a system with a test particle in an effective external metric. It uses a Hamiltonian that is constructed

with a radiation-reaction force. Resummation techniques [152] are applied to express both the Hamiltonian and radiation-reaction force non-polynomially. Additional parameters are incorporated to capture non-perturbative effects [153]. The EOB fits these free parameters to NR simulations for the inspiral and merger and adds an analytical model for the ringdown. The first waveform model including inspiral, merger and ringdown within the EOB family was developed in Ref. [154], initially for non-spinning BBHs, later extended to spinning cases in Ref. [155]. Later refinements included higher order modes, aligned spins, and precession [156]. Currently, the `SEOBNRv5PHM` [157] is the most comprehensive EOB model, taking into account both, higher order modes and precession. Solving differential equations for specific parameters with the EOB ansatz can be computationally expensive, and its time-domain formulation requires a frequency-domain transformation for data analysis. Therefore, reduced order models in the frequency domain are often used to speed up computations for GW search and parameter estimation [158, 159].

2.4.4 Numerical relativity surrogate waveform family

Surrogate modelling is a data-driven approach to waveform modelling where nothing is assumed about the underlying phenomenology. Instead, the NR waveforms themselves are used to implicitly reconstruct the phenomenology. This is achieved by first constructing an accurate basis using the NR waveforms and then using sophisticated interpolation techniques to create a waveform model. NR surrogate models are typically more accurate than the approximate methods described above, but are only valid in limited region of parameter space that is covered by the underlying simulations. The reader can see Ref. [160] or Ref. [161] for more technical details.

The first surrogate model was introduced in Ref. [162] and used non-spinning NR waveforms. The `NRSur7dq2` model [49] laid the foundation for full coverage of the seven-dimensional parameter space for the generic non-eccentric BBH problem. The development of `NRSur7dq4`, the latest generic surrogate model for precessing BBHs trained on 1528 SXS NR simulations, was carried out in the corotating frame. `NRSur7dq4` has relatively narrow parameter boundaries, $q \leq 4$, $|\vec{\chi}_1|$, $|\vec{\chi}_2| \leq 0.8$, and is claimed to have over 99 % accuracy against NR waveforms computed with the advanced LIGO design sensitivity noise curve [24]. Another advantage is the fast evaluation time of about 50 ms. However, an important limitation of this surrogate model is that it does not cover the whole LIGO frequency band, since it has a start time of about $-4300\,M$, i.e. it is valid for a total mass of $M \gtrsim 66 M_\odot$, assuming a GW starting frequency of 20 Hz [24]. To remedy this, a hybridised non-precessing model called `NRHybSur3dq8` is presented in Ref. [163]. In this work, NR waveforms are stitched together with PN and EOB waveforms at early times. In addition, Ref. [164] recently developed an eccentric model `NRSur2dq1Ecc` for non-spinning waveforms and eccentricities up to 0.2. There have also been surrogate models developed [165–167] for extreme mass-ratio inspirals using point-particle BH perturbation theory.

3 | Phenomenology of mode asymmetry

There are many ways to improve currently existing waveform models for GW signals from BBH coalescences. For example, numerical computing has made great progress in allowing faster and more complex simulations. In addition, neglected small physical effects can be implemented into newer waveform models. One of these small effects, which is encoded in the waveform itself, is the mode asymmetry, which is present in precessing BBHs.

We start with the general definition of the mode asymmetry in sec. 3.1. We then look at the morphology of several quantities derived from the mode asymmetry for a specific BBH configuration as an example in sec. 3.2. Sec. 3.3 and sec. 3.4 describe the dependence of these quantities on the intrinsic parameter space and in particular for BBH configurations with both spins in the orbital plane.

3.1 Definition of the +/− waveform

In some arbitrary frame for a $\ell \geq 2$ and a positive $0 < m \leq \ell$ we define

$$h^{\pm}_{\ell,m}(t) = \frac{h_{\ell,m}(t) \pm (-1)^{\ell}\, h^{*}_{\ell,-m}(t)}{2}\,. \tag{3.1}$$

This quantity is a complex-valued time series. We call it the *symmetric* waveform for "+" and the *anti-symmetric* waveform for "−". The symmetric/anti-symmetric (+/−) waveform describes a combination, sum or difference, of the $m > 0$ and $m < 0$ modes [24]. By multiplying the $h_{\ell,m}$ modes with their associated SWSH and remembering the structure of the SWSH, we can approximately identify the anti-symmetric waveform with the difference of the GW radiation above and below the orbital plane. In non-precessing systems the modes are invariant under reflection across the orbital plane and thus the symmetry

$$h_{\ell,m} = (-1)^{\ell}\, h^{*}_{\ell,-m} \tag{3.2}$$

holds. In this case $h^{+}_{\ell,m} = h_{\ell,m}$ and $h^{-}_{\ell,m} = 0$, so Eq. (3.1) is only non-trivial for precessing systems, where this symmetry is broken and we have $h_{\ell,m} \neq h^{*}_{\ell,-m}$ [31].

3.2 Morphology of mode asymmetries

The majority of waveform models ignore the broken multipole symmetry for precessing systems, limiting the number of models that can be used to discuss the +/− waveform characteristics. At the time of writing, only waveforms generated by `IMRPhenomXO4a` [147], NR surrogate models [24] or full NR simulations include mode asymmetries. To gain a deeper insight into the definition in Eq. (3.1), we analyse as an example the +/− waveform emitted by a particular precessing BBH configuration, which has a non-vanishing anti-symmetric

waveform but is otherwise arbitrarily chosen. In the following four chapters we decided for a NR waveform from the SXS collaboration [49, 52, 168] with the name `SXS:BBH:0802`. This is a $q = 2$ BBH configuration with both BHs spinning. The spins are defined at a reference orbital frequency of $f_{ref} \approx 0.0164\,\mathrm{rad}/M$ and take the values $\vec{\chi}_1 \approx (0.58, 0.01, -0.55)$ and $\vec{\chi}_2 \approx (-0.02, -0.07, 0.79)$. Most of the NR post-simulation techniques described in sec. 2.4.1, such as the Ψ_4 integration, are already applied to the data we get from the SXS catalogue. In addition, we cut out the junk radiation before f_{ref} from the modes. Nevertheless, at the boundaries of the time series or for very small values, some numerical noise may be visible in the following plots. Finally, we shift the time series so that the time at which a common event horizon forms is $t = 0$, which is approximately the time of merger defined in Eq. (2.41) via the peak amplitude of the mode sum.

3.2.1 Real and imaginary part

To learn something about the phenomenology of time-domain waveforms, the most intuitive way is to look at the real or imaginary part of the complex-valued time series. We expect the $+/-$ waveform to be a sinusoid with a time-dependent frequency, since it is a combination of sinusoidal modes $h_{\ell,m}$. In Fig. 3.1 we compare the real and imaginary part of dominant symmetric waveform $h^+_{2,2}$ with the dominant modes $h_{2,\pm2}$. We observe that the waveforms $\mathrm{Re}(h^+_{2,2})$ and $\mathrm{Im}(h^+_{2,2})$ behave like the average of the real and imaginary parts of the positive and negative m-modes for fixed ℓ, respectively. This behaviour is something expected from the definition of the symmetric waveform itself. With $\mathrm{Im}(z^*) = -\mathrm{Im}(z)$ for any complex number $z \in \mathbb{C}$, Eq. (3.1) can be decomposed:

$$\mathrm{Re}\left(h^+_{\ell,m}\right) = \begin{cases} \dfrac{\mathrm{Re}(h_{\ell,m}) + \mathrm{Re}(h_{\ell,-m})}{2}, & \ell\,\text{even}, \quad (3.3) \\ \dfrac{\mathrm{Re}(h_{\ell,m}) - \mathrm{Re}(h_{\ell,-m})}{2}, & \ell\,\text{odd}, \quad (3.4) \end{cases}$$

$$\mathrm{Im}\left(h^+_{\ell,m}\right) = \begin{cases} \dfrac{\mathrm{Im}(h_{\ell,m}) - \mathrm{Im}(h_{\ell,-m})}{2}, & \ell\,\text{even}, \quad (3.5) \\ \dfrac{\mathrm{Im}(h_{\ell,m}) + \mathrm{Im}(h_{\ell,-m})}{2}, & \ell\,\text{odd}. \quad (3.6) \end{cases}$$

It seems that the minus sign in Eq. (3.4) and Eq. (3.5) does not correspond to the definition of a conventional average. But since we assume that in a precessing system the mode symmetry is only broken at a small level, and Eq. (3.2) is approximately valid, we have exactly the average behaviour we wanted with the definition of the symmetric waveform. Analogously, the same argument holds for the anti-symmetric waveform, which is a quantity that measures the difference between the modes with positive and negative m for fixed ℓ.

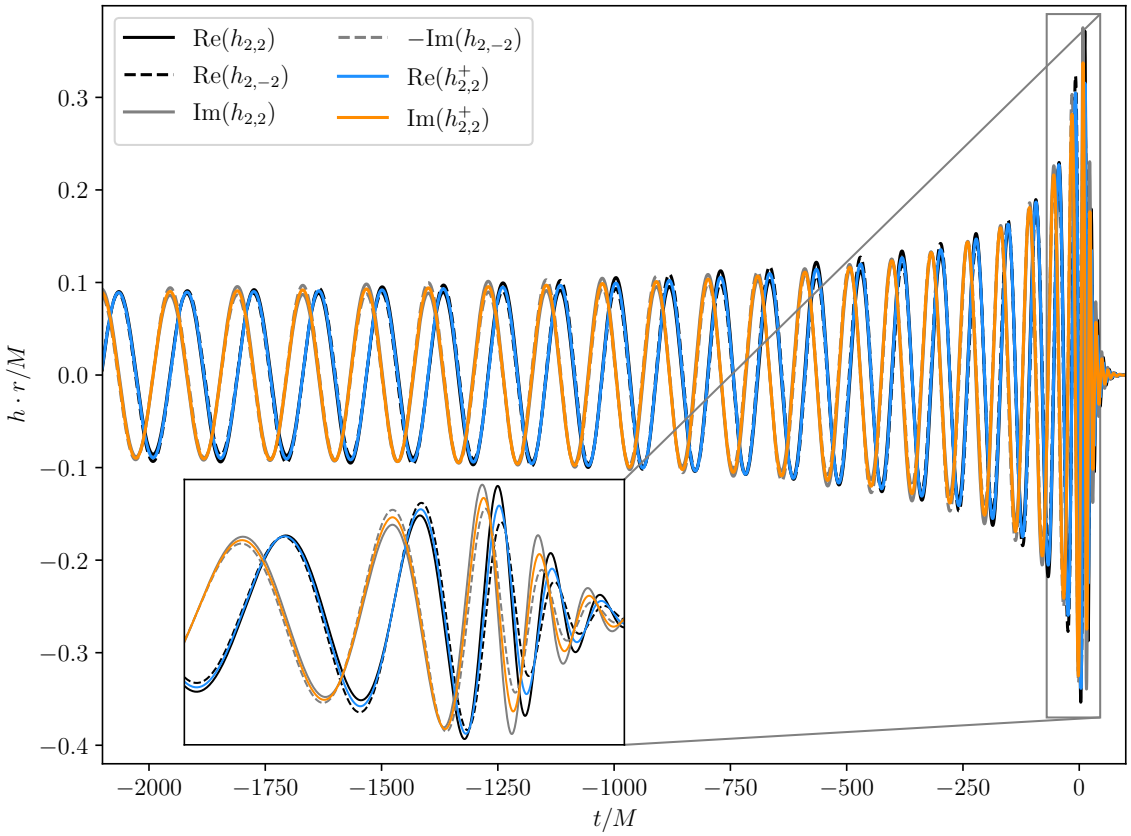

Figure 3.1: Real and imaginary part of the symmetric waveform $h^{\pm}_{2,2}$ and the dominant modes $h_{2,\pm2}$ of the `SXS:BBH:0802` configuration in the inertial frame. The symmetric waveform is the average of the $h_{2,\pm2}$ modes. In the merger regime there is a bigger amplitude difference between the positive and negative m-mode and a slightly different phase behaviour. Note that $-\mathrm{Im}(h_{2,-2})$ is plotted, since there is π-phase shift with respect to $\mathrm{Im}(h_{2,2})$ because ℓ is even.

In Fig. 3.2 the real and imaginary part of the anti-symmetric waveform is compared to the symmetric waveform of `SXS:BBH:0802`. We observe that in the inspiral regime the anti-symmetric waveform is much smaller than the symmetric one, but builds up to a significant amount until the merger. There is a slight difference between the symmetric and anti-symmetric waveform in terms of the time at which the maximum of the waveform is reached. Note that the phase shift between the symmetric and anti-symmetric waveform has some influence on the recoil velocity of the remnant BH, which we will see in sec. 4.5. In addition, we can see that the symmetric waveform oscillates faster than the anti-symmetric one. Since it is difficult to observe and explain all the physical effects using only the real and imaginary parts of the $+/-$ waveform, in the next chapter we will focus on another representation of the complex-valued function $h^{\pm}_{2,2}(t)$.

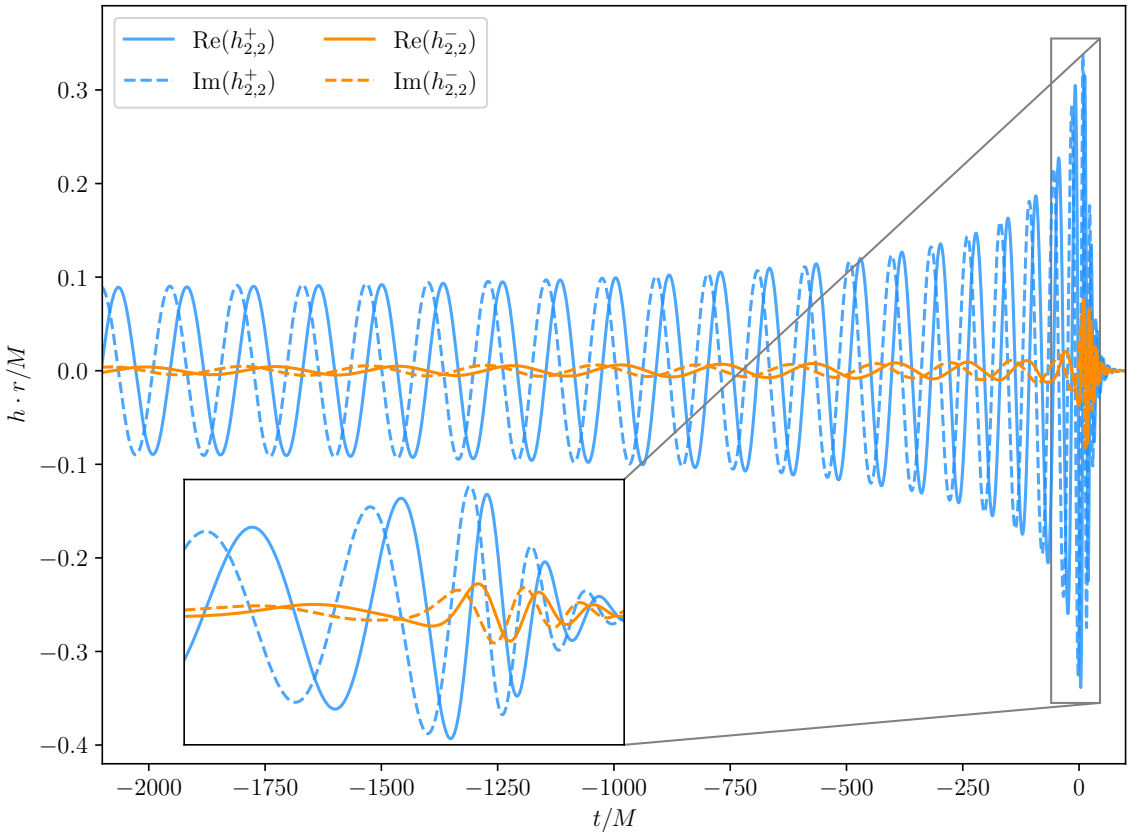

Figure 3.2: Real and imaginary part of the dominant +/− waveform of the `SXS:BBH:0802` configuration in the inertial frame.

3.2.2 Amplitude and phase

Any complex number can be expressed in an exponential form, including

$$h^{\pm}_{\ell,m}(t) = a^{\pm}_{\ell,m}(t)\, e^{i\phi^{\pm}_{\ell,m}(t)}\,. \tag{3.7}$$

We denote $a^{+}_{\ell,m} = |h^{+}_{\ell,m}| \in \mathbb{R}$ as the symmetric amplitude and $\phi^{+}_{\ell,m} = \arg(h^{+}_{\ell,m}) \in \mathbb{R}$ as the symmetric phase. We call this the anti-symmetric amplitude and phase in the "−" case.

In Fig. 3.3, we can observe the effects more clearly, which were indicated in Fig. 3.2. The symmetric amplitude for `SXS:BBH:0802` increases until the time is about $\hat{t}^{+} \approx 5.8\,M$, while the anti-symmetric amplitude peaks at about $\hat{t}^{-} \approx 14.3\,M$ before decaying exponentially. We observe small oscillations in the inspiral regime of $a^{\pm}_{\ell,m}$. This was found partially to be a result of the inertial frame and is at least for $a^{+}_{\ell,m}$ eliminated by converting to the coprecessing frame, but is still visible for $a^{-}_{\ell,m}$, see Fig. 3.5. The ratio of peak amplitudes is about 24 %, which is a large amount, at least in the merger regime, especially considering that mode asymmetries are ignored in most waveform models. The high ratio also means that the anti-symmetric

waveform in this regime is of great importance in describing the physics that occurs during the merger, such as the remnant BH recoil, which we will analyse in sec. 4. However, the effect of the anti-symmetric waveform on the SNR is negligible, as this waveform is of small order of magnitude in the inspiral regime, which has the largest impact on the SNR [117]. Nevertheless, it is worth investigating the characteristics of the anti-symmetric waveform as it allows the measurement of spins in third generation detectors or the detection of the remnant BH recoil velocity [32, 169–172].

In the inspiral regime, the symmetric phase $\phi^{+}_{\ell,m}$ evolves more than twice as quickly as the anti-symmetric phase $\phi^{-}_{\ell,m}$, which corresponds to the observation of a faster oscillation of the symmetric waveform compared to the anti-symmetric waveform in Fig. 3.2. Around the $+/-$ waveform time of the merger $\hat{t}^{\pm}$, the phases begin to fall faster as the ringdown begins. In addition the phases become parallel to each other, i.e. the phase derivatives should be equal in the merger-ringdown regime.

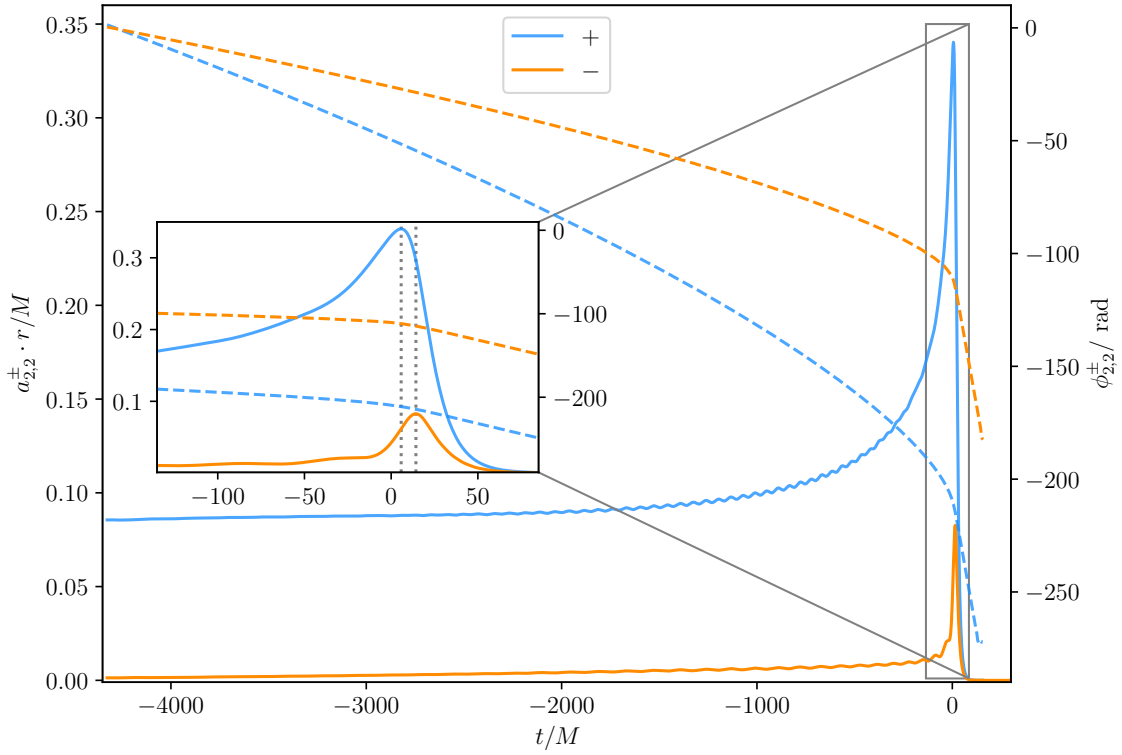

Figure 3.3: Amplitude and phase of the dominant $+/-$ waveform of the `SXS:BBH:0802` configuration in the inertial frame. The left axis corresponds to the solid lines, while the right axis corresponds to the dashed lines. The inset shows the merger regime. The grey dotted lines indicate the maxima of $a^{\pm}_{\ell,m}$ at $\hat{t}^{+} \approx 5.8\,M$ and $\hat{t}^{-} \approx 14.3\,M$, respectively.

3.2.3 Subdominant +/− waveforms in different source frames

As already seen in sec. 2.2.6 GW modes contain modulations of the amplitude and phase in an inertial frame. These modulations occur especially in the case of subdominant modes, because the power of the dominant modes is radiated in the subdominant modes due to the movement of the orbital plane. Since the +/− waveform is a combination of positive and negative m-modes, we expect these artefacts as well. In Fig. 3.4 it is shown that these beat artefacts are visible in $h^{-}_{2,1}$ of `SXS:BBH:0802`, but can be simplified by converting the modes $h_{2,\pm1}$ to the coprecessing or corotating frame and then applying Eq. (3.1).

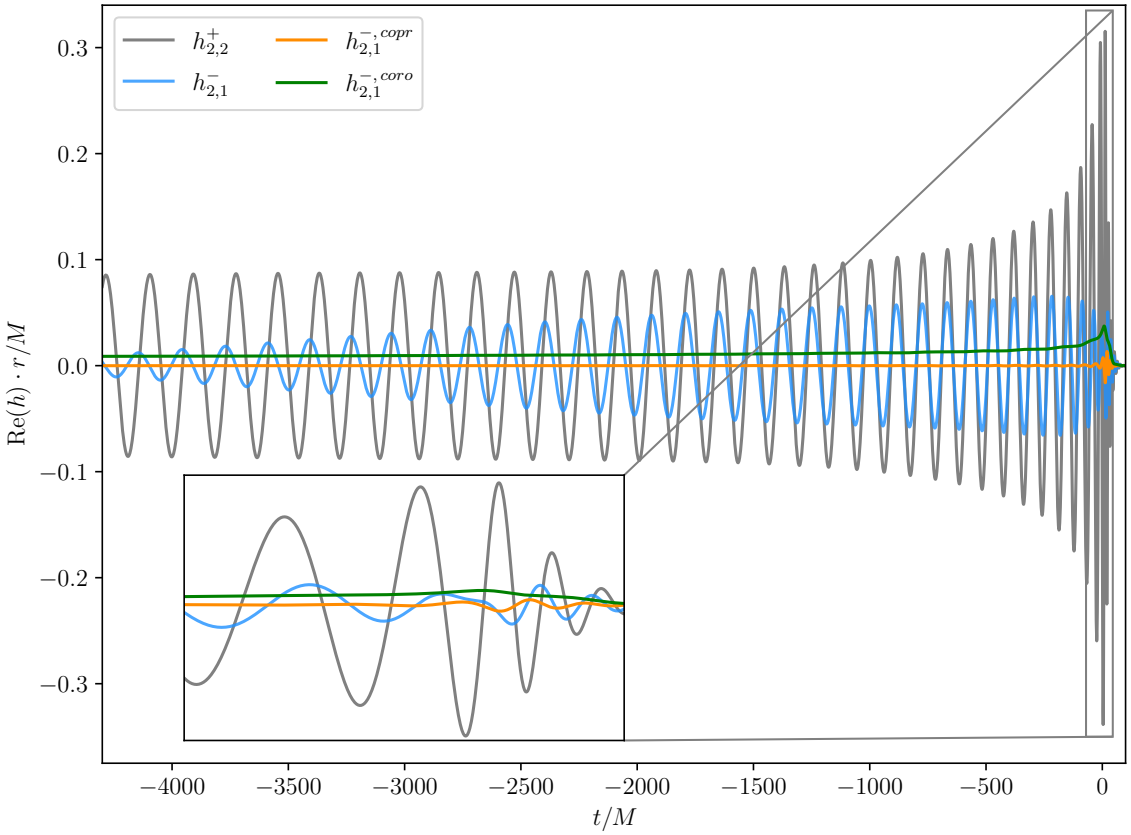

Figure 3.4: Real part of the anti-symmetric $h^{-}_{2,1}$ waveform of `SXS:BBH:0802` in the inertial (blue), coprecessing (orange) and corotating (green) frame. To see the order of magnitude of the dominant modes, the symmetric waveform $h^{+}_{2,2}$ is plotted in grey.

It turns out that these rotations do not cancel out the anti-symmetric waveform. It is natural to ask whether the non-vanishing of the anti-symmetric waveform holds in general for all precessing configurations, or whether we could get rid of the asymmetries by finding another rotation of the coordinate system. Everything points to that the mode asymmetry is indeed rotationally invariant, i.e. no rotation can eliminate the anti-symmetric waveform of an arbitrary precessing system. In Ref. [31] this was shown by some analytical considerations for frame rotations.

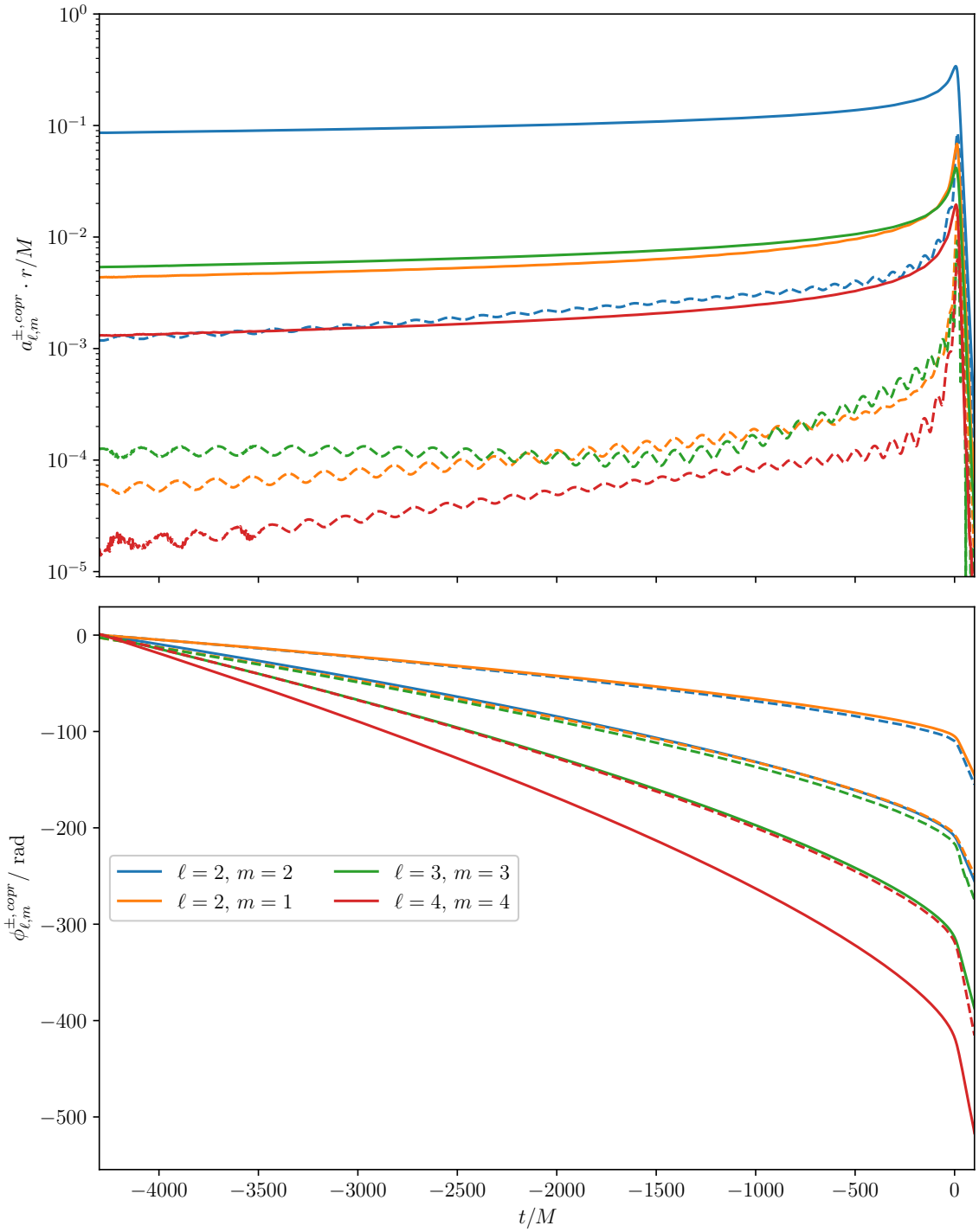

Figure 3.5: Amplitude and phase behaviour of the four most dominant coprecessing-frame waveforms $h^{\pm,copr}_{\ell,m}$ of `SXS:BBH:0802`. The solid lines are the "+" case, while the dashed lines are the "−" case.

Note, however, that putting too much time dependence of a waveform into a time-dependent frame rotation can oversimplify the physics. For example, it is harder to understand the physics in the corotating frame because the waveform is less sinusoidal and we have no clear

phase behaviour. So we treat the corotating frame as a strong mathematical concept, which is of course powerful for applying empirical interpolation methods in models like `NRSur7dq4`, but makes it more difficult to understand some physical concepts. We will concentrate on the coprecessing frame in the following, leaving the corotating frame +/− waveform for subsequent research.

In the upper plot of Fig. 3.5 the amplitudes of the +/− waveform in the coprecessing frame $a^{\pm,\,copr}_{\ell,m}$ are illustrated on a logarithmic scale. In fact, the oscillations of the symmetric amplitude are cancelled out by the frame rotation, but are still present for the anti-symmetric amplitude. It is planned to further investigate the anti-symmetric amplitude oscillations and to explore additional dimensions of the problem in subsequent research. But what we can already see is that $a^{\pm,\,copr}_{\ell,m}$ follow a clear order with respect to their magnitude, here for `SXS:BBH:0802` in the order $a^{+,\,copr}_{2,2}$, $a^{+,\,copr}_{3,3}$, $a^{+,\,copr}_{2,1}$ and $a^{+,\,copr}_{4,4}$. The corresponding anti-symmetric amplitudes are up to two orders of magnitude smaller. For the dominant (2, 2) anti-symmetric amplitude, this means that it is almost as strong as the next strongest symmetric (3, 3) amplitude. In the merger regime, the anti-symmetric amplitudes increase significantly, almost to the order of magnitude of their corresponding symmetric amplitude.

The subdominant time series behave similarly to the dominant. Similar to how the dominant phases are related by $\phi^+_{2,2} \approx 2\phi^-_{2,2}$ in the inspiral, there is a factor that relates the subdominant phases. For instance we found for `SXS:BBH:0802` $\phi^+_{2,1} \approx 1/2\,\phi^-_{2,1}$, $\phi^+_{3,3} \approx 17/12\,\phi^-_{3,3}$ and $\phi^+_{4,4} \approx 13/10\,\phi^-_{4,4}$. To figure out the exact factors with possible corrections from the spin-precession rate is a current task of research [32]. For us it is important to note that the difference $\phi^+_{\ell,m} - \phi^-_{\ell,m}$ stays approximately constant for $t \to \infty$, since the curves get parallel in the merger-ringdown regime. In other words it holds $\dot{\phi}^+_{\ell,m} = \dot{\phi}^-_{\ell,m}$ during ringdown, which is expected from perturbation theory [32]. In sec. 4.5 we will analyse the phase differences in more detail in relation to the remnant BH recoil.

3.2.4 Frequency domain

A discussion of the +/− waveform of `SXS:BBH:0802` in the frequency domain is worthwhile for modelling reasons. But first, let us introduce the Fourier domain definition of the +/− waveform

$$\tilde{h}^{\pm}_{\ell,m}(f) = \mathcal{F}\left[h^{\pm}_{\ell,m}(t)\right] = \frac{\tilde{h}_{\ell,m}(f) \pm (-1)^{\ell}\,\tilde{h}^{*}_{\ell,-m}(-f)}{2}\,. \tag{3.8}$$

Fig. 3.6 shows the dominant +/− frequency-domain waveform in the coprecessing frame. Since we are dealing with a discretised time series, the Fourier transform is a bit tricky and we have to apply several steps to get smooth curves. First, we transform the individual NR modes from the inertial to the coprecessing frame and plug them into Eq. (3.1). Then we use a standard cubic interpolation method implemented in `SciPy` [173] to interpolate $h^{\pm}_{\ell,m}(t)$ to uniform time steps. We then apply a Tukey window with a shape parameter of $\alpha = 0.015$

[174] to reduce the Gibbs effect [175], a ringing artefact in discrete Fourier analysis. Finally, we apply a standard discrete fast Fourier transform algorithm implemented in `NumPy` [176] and normalise the result. Analytically, this procedure should be the same as first Fourier transforming the modes and then plugging them into Eq. (3.8). However, there are some small differences that can be resolved with further numerical Fourier techniques.

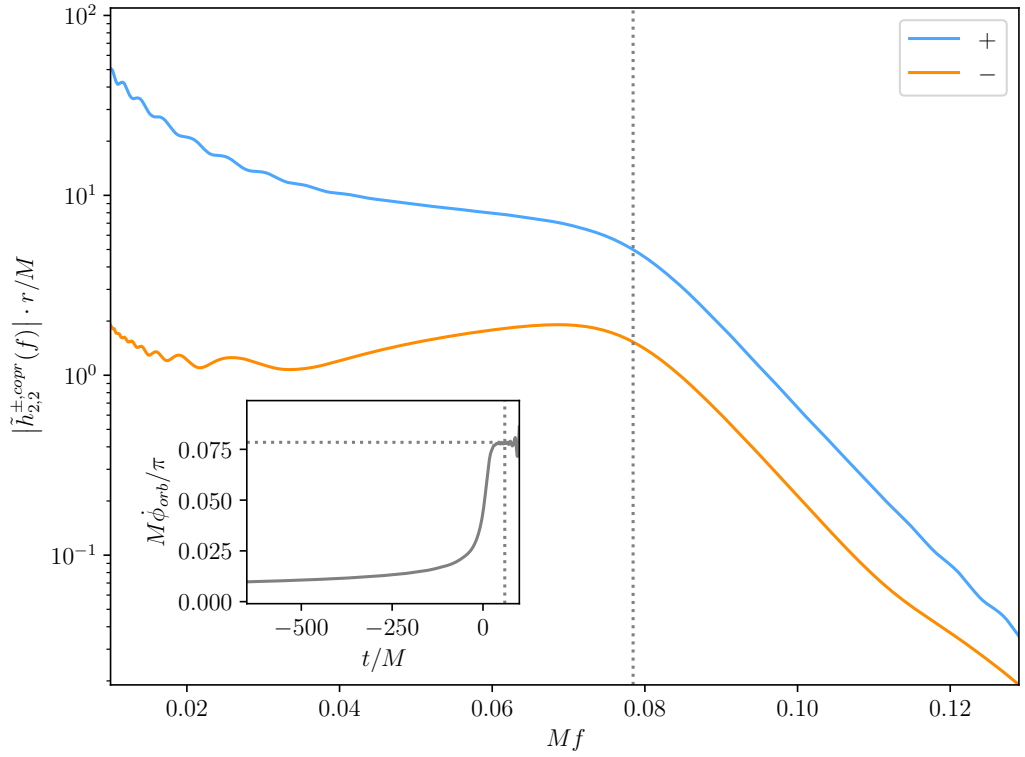

Figure 3.6: Amplitude of the dominant $+/-$ waveform in the frequency domain for the NR simulation `SXS:BBH:0802`. The inset shows the phase derivative as defined in Eq. (2.45) and divided by π to have the same units as the Fourier frequencies. The vertical grey dotted line at $t_{RD} \approx 60\,M$ represents the ringdown start time and the horizontal grey dotted line represents the ringdown frequency at about $Mf_{RD} \approx 0.078$.

To build a model of the anti-symmetric amplitude in the frequency domain, as was done in Ref. [32], we can use the fact that the symmetric amplitude is a kind of rescaling of the anti-symmetric one. In addition, we can observe an approximately equal decay rate of the $+/-$ waveform for $f > f_{RD}$, where $Mf_{RD} \approx 0.078$ is the ringdown frequency for `SXS:BBH:0802`. We get the ringdown frequency by computing the derivative of the orbital phase defined in Eq. (2.45) and identify the ringdown frequency with the phase derivative at which the phase derivative stabilises during ringdown at around $t_{RD} \approx 60\,M$, which is shown in the inset of Fig. 3.6. The ringdown frequency is of great interest when building phenomenological models [140]. To summarise this short chapter on frequency-domain waveforms, it is more difficult to intuitively understand the dynamic features of the waveform, but Fourier domain models

are usually much quicker to evaluate. In the following, we will return to the time-domain, as our main objective is not to build a model, but rather to understand the physical imprint of the intrinsic parameters on the waveform and the recoil of the remnant BH.

3.3 Variations in parameter space

Now that we have seen the basic morphology of the mode asymmetry for a particular configuration, we examine some of the main properties of the $+/-$ waveform by varying the intrinsic parameter space. In sec. 2.2.6 and sec. 2.2.7 we introduced the tools to deal with the different modes $h_{\ell,m}$, which we get from most waveform models or NR simulations. We can specify the spins of a BBH configuration at a self-chosen reference epoch and transform the modes into different coordinate frames. Since NR surrogate models are based on interpolations of an accurate basis using NR waveforms themselves, these models already include mode asymmetries in the time domain, albeit in a very limited region of the full parameter space. To generate the plots in this chapter we will use the latest version `NRSur7dq4` of the NR surrogate waveform family [24].

We reduce the seven-dimensional space to four dimensions and start with a single-spin configuration. Note that the analysis of only one BH spinning is an appropriate procedure, since there are methods which map between generic two-spin configurations and approximately equivalent single-spin configurations where the spin is placed on the heavier BH [177]. In Fig. 3.7 we fixed three of the four parameters, $q = 1$, $\chi = 0.8$, $\theta = \pi/2$ and $\phi = 0$, and varied the remaining fourth parameter for 1024 samples in a calibration range covered by `NRSur7dq4`. The spin in each sample is defined close to merger at $t_{ref} = -100\,M$. To learn how the mass ratio q, spin magnitude $\chi = |\vec{\chi}|$, out-of-plane spin angle θ and in-plane spin angle ϕ of the heavier BH affect the $+/-$ waveform, we focus on the peak of the dominant $+/-$ amplitude in the coprecessing frame

$$\hat{a}^{\pm} = \max_t \left(a_{2,2}^{\pm,\,copr}(t) \right) . \tag{3.9}$$

The corresponding time argument $\hat{t}^{\pm} \approx 0$ is approximately at the time of merger. There are other possible choices to compare waveforms like the inner product of two functions as described in Eq. (2.58), but since we are mostly interested in the magnitude of the anti-symmetric contribution in comparison to the symmetric one, the dominant peak amplitude is a reasonable choice. Some basics of the anti-symmetric phase behaviour in the parameter space are discussed in sec. 4, in the context of the BH recoil. However, it is now already worth mentioning that in Ref. [32] a map was found from the symmetric phase derivative to the anti-symmetric phase derivative which is independent of location in the parameter space.

The $+/-$ waveform has a strong dependence on q as can be seen in Fig. 3.7. The decreasing behaviour of the dominant symmetric peak amplitude and the slow increasing in the anti-symmetric case is already noticeable from PN equations. Therefore we take a look at

the coprecessing frame PN expressions given in Eq. (13) and Eq. (14) of Ref. [32]. Note that even though these equations are given in the frequency-domain, we can build an argument for our time-domain considerations on them, since only the PN expansion parameters depend on frequency and not the expansion coefficients, which are responsible for the amplitude changes with variations in parameter space. So we use the coefficients and observe up to their respective leading orders:

$$\begin{aligned} a_{2,2}^{+,copr} &\sim \eta = \frac{q}{(1+q)^2}\,, \\ a_{2,2}^{-,copr} &\sim (1+\delta)\eta = \frac{2q^2}{(1+q)^3}\,. \end{aligned} \tag{3.10}$$

Here $\eta = m_1 m_2/M^2$ is the symmetric mass ratio and $\delta = (m_1 - m_2)/M$ is the fractional mass difference. Indeed, we observe that the unintuitive morphology of these expressions persists until the merger, as can be seen by comparing the dashed lines with the solid lines in the upper left plot of Fig. 3.7.

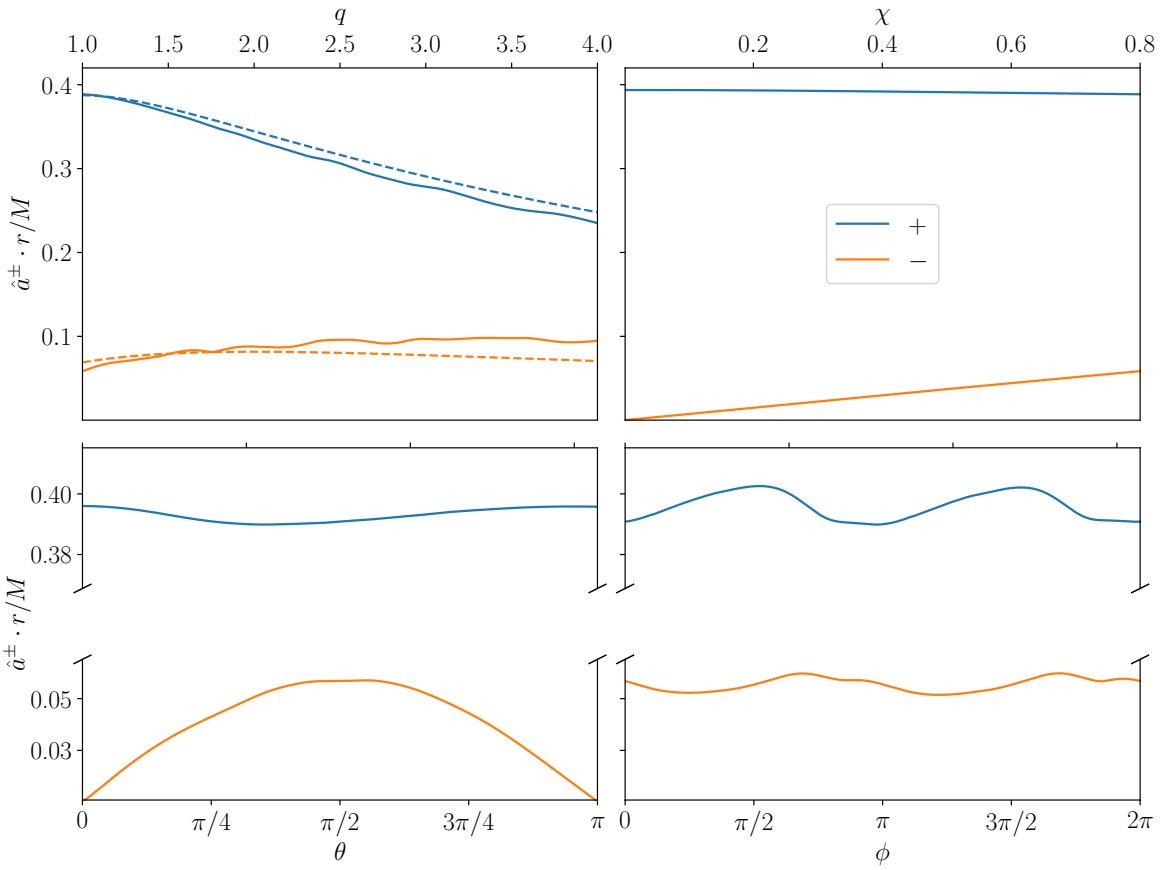

Figure 3.7: Peak amplitude of the dominant $+/-$ waveform $\hat{a}^{\pm}$ for variations in the parameter space of a BBH system with the spin placed on the heavier BH. Note the scales and the break in the y-axis of the lower plots, which means that the oscillations are in a small order of magnitude. In the upper left plot, the morphology of the PN equations from Eq. (3.10) with a proportionality factor chosen to fit the scale of the plot are shown as dashed lines.

The anti-symmetric amplitude scales linearly with the spin magnitude χ, while the symmetric amplitude is independent on χ. This is also expected from the PN expressions mentioned in the paragraph above, since $a_{2,2}^{-,copr} \sim \chi$ and $a_{2,2}^{+,copr}$ is not a function of χ in this particular in-plane spin configuration with $\theta = \pi/2$ up to PN order $\mathcal{O}(\nu^5)$, where ν is the PN expansion parameter which can be expressed as $\nu = (M\omega_{orb})^{1/3}$. Note that we have chosen equal-mass configurations here, with the spin completely in the plane. So there could be higher order terms that depend on θ and q, disturbing the clear linear dependence of $\hat{a}^-$ on χ.

The same PN expression can be used to explain the effect of the polar angle on the anti-symmetric amplitude. We have $a_{2,2}^{-,copr} \sim \sin\theta$, i.e. the anti-symmetric waveform reaches its maximum if the spin is completely in the plane, $\theta = \pi/2$. This behaviour is expected, since the anti-symmetric waveform vanishes for aligned-spin systems, i.e. $\theta = 0$ and $\theta = \pi$. For the symmetric amplitude we see some small variations with θ. These may have some physical explanation, but since there is a dependence on θ only in the PN order of $\mathcal{O}(\nu^5)$, we expect the dependence to be very small. In addition, we choose to measure the variation of the $+/-$ waveform at a point in the merger regime where it is questionable whether the PN expressions hold. So we assume that the symmetric waveform does not change to much with the out-of-plane spin.

In the lower right plot of Fig. 3.7, we observe small π-periodic oscillations of the $+/-$ amplitude when varying the in-plane-spin ϕ. This is surprising, since PN expressions predict no ϕ-dependence in either $+/-$ amplitude. In order to analyse the in-plane spin effect in more detail, in the following chapter we consider systems with two BHs spinning in the plane.

3.4 In-plane spin configurations

We analyse equal-mass two-BH spinning configurations by fixing the spin of the second BH with a magnitude of $|\vec{\chi}_2| = 0.8$ in the direction of the separation vector. The first BH with the same spin magnitude is rotated by an angle ϕ_1 in the orbital plane. Both spins are entirely in the plane. Note that this rotation mainly changes the sum of both spins, i.e. the total in-plane spin magnitude, and we are not analysing a pure in-plane spin angle effect. However, we do find a secondary result from the ϕ_1-rotation, which shows a real in-plane spin angle effect on the phase of the anti-symmetric waveforms, which we will explain below.

But first, the explanation of the primary result, best visible in the inset of Fig. 3.9, namely that the magnitude of the anti-symmetric waveform is approximately symmetric around the maximum at $\phi_1 = \pi$, is not trivial. This is counterintuitive to the argument made in the previous chapter for the out-of-plane angle θ, because for $\phi_1 = \pi$ the in-plane spin magnitude is zero.

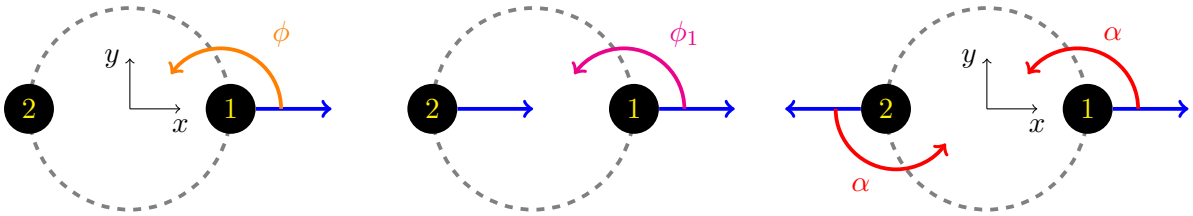

Figure 3.8: Illustration of three different in-plane spin rotations of equal-mass binaries used in this chapter. The reader is facing the orbit, so that the orbital plane is in the paper plane. The blue arrows indicate the BH spins with a magnitude of $\chi_i = 0.8$ defined at $t_{ref} = -100\,M$. The left plot shows the rotation of the azimuthal angle ϕ for only one of the BH spins used in Fig. 3.7. The middle plot shows the azimuthal angle rotation of the first BH ϕ_1, while the second BH has a fixed spin direction, so that for a ϕ_1 rotation the sum of the two spin vectors is not constant. In contrast, in the right-hand plot, a simultaneous rotation of both spins in the plane by an angle α keeps the spin sum to zero, a superkick configuration for all α.

We assume that the increase of the anti-symmetric amplitude with the misalignment of the two spins in the orbital plane is related to the bobbing of the whole orbital plane for these particular configurations, which also reaches the peak for the maximum spin misalignment $\phi_1 = \pi$ [178]. Therefore, it is important to note that for anti-aligned in-plane spin configurations with the same spin magnitude, the orbital plane changes only with the z-direction. So the mode asymmetry of the positive and negative m-modes results in an up-and-down movement of the orbital plane in the direction of the orbital angular momentum. Maybe the mode asymmetries can be resolved with a frame transformation. For BBH configurations with a vanishing spin sum component in the plane, the orbital angular momentum does not precess, i.e. the inertial and coprecessing frame are identical. Because the coprecessing frame does not follow the bobbing of the orbital plane, we may be able to define a centre-of-mass frame, in which the bobbing is cancelled, and thus the anti-symmetric waveform could disappear. Whether or not this statement about boosted frames is true is a task for future work. Incidentally, these fine-tuned BBHs of equal mass, with spins lying in the plane and pointing in opposite directions, are called *superkick* configurations, which were discovered in Ref. [179, 180]. The reason for the name and the bobbing of the orbital plane will be explored in a sec. 4

Besides the magnitude of the anti-symmetric waveform depending on the rotation of ϕ_1, we find some interesting phase dependence on this rotation when looking at the real part of the waveforms in Fig. 3.9. Between different in-plane spin directions there seems to be only an overall phase shift. Indeed the PN calculations and explorations in Ref. [32] confirm this observation. The PN expression predicts $h^{-,copr}_{2,2} \sim \exp(-i(\phi_{orb} + \alpha))$, i.e. a rotation of the spin within the plane by an angle $\Delta\alpha$, causes a corresponding shift in the dominant anti-symmetric phase by $\Delta\alpha$. Here we have a different notation, and we use α for an in-plane

spin rotation, because we want to rotate both spins at once, as opposed to Fig. 3.9 where one spin was fixed, i.e. a α-rotation is a pure in-plane angle effect. For the α-rotation, we use the superkick case since the anti-symmetric amplitude is at maximum. However, the phase shift argument is true for all configurations, in which the relative angle between the spins is fixed in an α-rotation. In Fig. 3.10 we choose $\vec{\chi}_1 = 0.8 \cdot (\cos\alpha, \sin\alpha, 0)$ and $\vec{\chi}_2 = -\vec{\chi}_1$ specified at $t_{ref} = -100\,M$ to show the phase shift in the waveform by an angle of α. As an example, we have chosen $\alpha = 0$ and applied a phase shift of $\exp(-i\pi/2)$ to obtain approximately the same anti-symmetric phase as for a configuration with $\alpha = \pi/2$. The amplitudes are slightly different, as can be seen in the lower right plot of Fig. 3.7. To summarise the in-plane spin effect, we have found a simple phase dependence of the anti-symmetric waveform on the in-plane spin, but we can only state that there are small periodic amplitude modulations with a variation of the in-plane spin angle, without a good explanation.

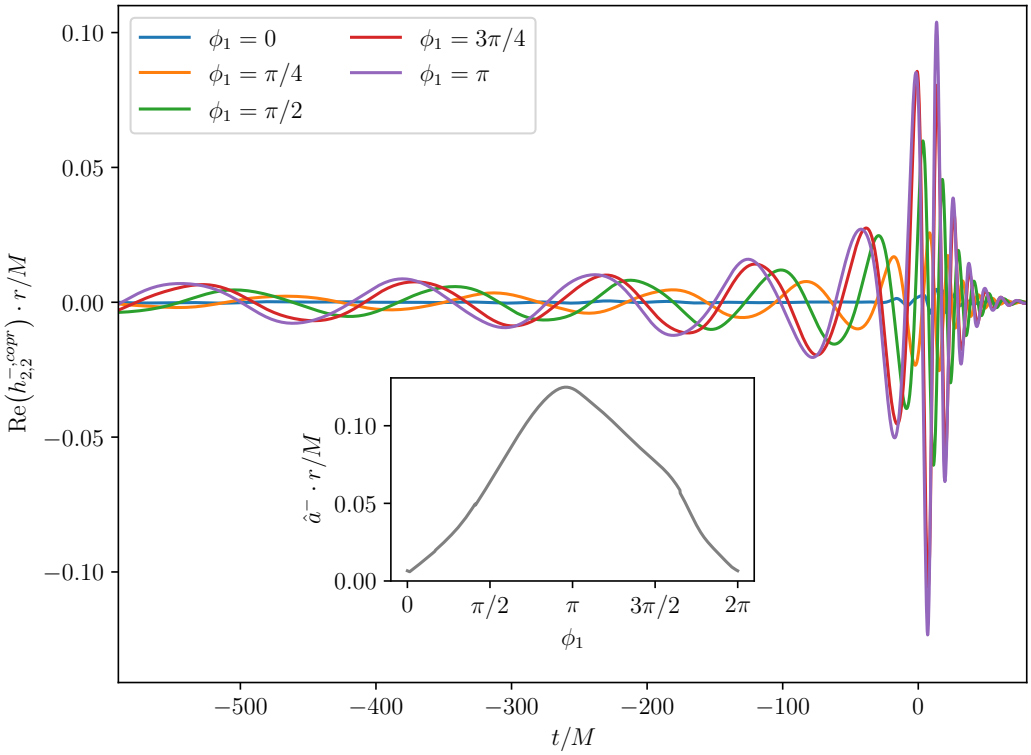

Figure 3.9: Dominant anti-symmetric waveform of equal-mass in-plane spin configurations defined at $t_{ref} = -100\,M$. $\phi_1 = 0$ corresponds to both spins pointing in the same direction, while for $\phi_1 = \pi$ the spins are pointing in the opposite direction. The inset shows the sinusoidal dependence of the anti-symmetric peak amplitude on the in-plane spin rotation of ϕ_1, which effectively changes the spin sum.

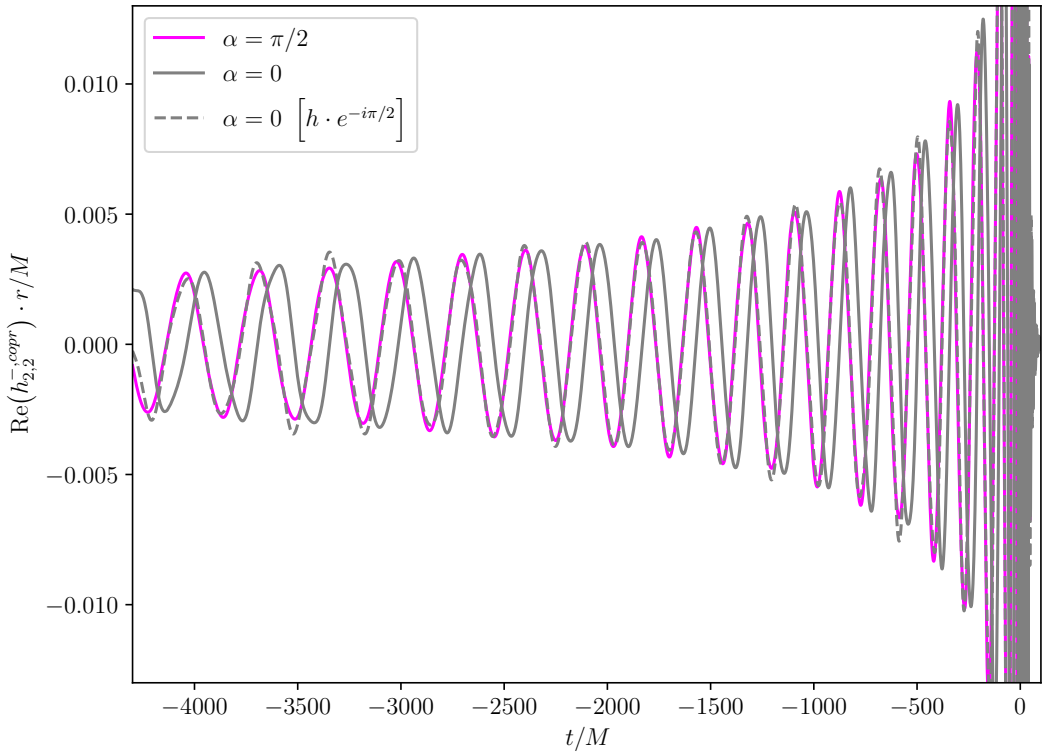

Figure 3.10: Anti-symmetric waveform for two configurations with oppositely aligned spins in the plane. For $\alpha = 0$ both spins are collinear to the separation vector, while for $\alpha = \pi/2$ both spins are perpendicular to the separation vector. The dashed grey line is the same waveform in the $\alpha = 0$ case, but a $\pi/2$ phase shift is applied to the waveform. In the inspiral regime it is in very good agreement with the $\alpha = \pi/2$ waveform, which is also approximately true for the merger regime. The figure is reconstructed from Fig. 2 in Ref. [32].

4 Correlating black hole kicks with mode asymmetry

In this section we go into the merger and ringdown regime and analyse the interplay between the GWs of precessing BBHs and the recoil velocity of the remnant BH. The reader can skip sec. 4.1 and sec. 4.2 if they are already familiar with the physics leading to the different recoil velocities. In sec. 4.3 we analyse the influence of the spin direction on the recoil and the dominant anti-symmetric waveform amplitude. Finally, the analytical expression for the linear momentum flux in terms of the $+/-$ waveform derived in sec. 4.4 is further discussed in sec. 4.5 and sec. 4.6.

4.1 Physics of the remnant black hole

When two BHs are in orbit around each other, they emit GWs and thereby lose energy, linear and angular momentum, as described by Eq. (2.32)−(2.34). As they get closer, their orbital velocity increases and at the final stages of their inspiral, they merge into a single BH, releasing a large amount of GW radiation. We will now focus a little bit more on the properties of the final BH.

It is difficult to determine the exact time during coalescence when the final BH begins to exist. The usual time of merger is defined by the peak of the waveform, see Eq. (2.41), but this does not tell us anything directly about the horizon structure of the remnant BH. However, we can at least state that the formation of an apparent horizon must occur close to the usual time of merger. In this dynamical strong field regime the apparent horizon is expected to be highly distorted [181], but if we go further in time we can fully characterise the final BH by its spin $\vec{\chi}_f$ and mass m_f. There is also an additional feature called the recoil velocity $\vec{v}_f$.

The amount of energy and angular momentum emitted by the source, and hence the amount of m_f and $\vec{\chi}_f$, depends mostly on the spin-orbit coupling, as well as the mass ratio and total mass of the inspiralling system, as can be seen in the PN equations [48]. When the total spin component aligns/opposes with the orbital angular momentum direction, more/less energy and angular momentum are generally emitted compared to a non-spinning case. This phenomenon is called the *orbital hangup effect* [30, 47, 182, 183]. The heuristic explanation of this effect is that BBHs with spins aligned/anti-aligned with $\vec{L}$ will merge slower/faster than non-spinning binaries, starting from the same reference epoch. This is because a spin addition of $\vec{L}$ with the individual BH spins $\vec{s}_1$ and $\vec{s}_2$ is not allowed to be larger than the maximum allowed spin magnitude of the Kerr BH $a = M$, so that a longer time is needed to radiate angular momentum in the form of GWs. On the other hand, in the anti-aligned case there is no need to radiate angular momentum away and the merger occurs earlier.

Any property of an orbit such as unequal BH masses or spin precession, that leads to an anisotropic GW radiation, could result in the newly formed BH receiving a recoil in the opposite direction of the GW linear momentum flux, which we also call a *kick*. The kick is a result of the conservation of momentum, similar to the recoil experienced when releasing a shot of a weapon. Kicks can be significant and have important astrophysical consequences. For instance, if the kick is strong enough, it can cause the merged BH to escape its host galaxy. The *in-plane kick* refers to the component of the final recoil velocity that is within the orbital plane of the BBH system just before merger. In addition to the mass ratio, the in-plane kick is influenced by the spins that are aligned or anti-aligned with the orbital angular momentum, and thus in-plane kicks occur even for non-precessing BBHs [184–186]. On the other hand, the *out-of-plane kick* refers to the component of the final recoil velocity that is perpendicular to the orbital plane. This kick is primarily influenced by the spin components not aligned with the orbital angular momentum. In this case the spins contribute to a mode asymmetry in the GWs, leading to a non-zero out-of-plane kick. In other words, the in-plane kick can be described with higher modes without considering mode asymmetry, but the out-of-plane kick needs a further investigation in the asymmetric emission between negative and positive m-modes, i.e. there is a relation to the $+/-$ waveform.

Strongly precessing BBHs have been found to generate kicks over 1000 km/s. One of these special configurations is the superkick configuration already mentioned in sec. 3.4, i.e. equal-mass binaries with identical spin magnitudes completely in the orbital plane but anti-parallel to each other [33, 184]. Note that there is no orbital precession for superkick configurations, since both spins precess at the same rate in the orbital plane, i.e. the spins remain opposite to each other during the time evolution and the vector sum remains zero [32]. To understand why superkick configurations can result in a large kick, we need to consider the constructive addition of the frame-dragging effect of both BHs. We will use an explanation given by Frans Pretorius in this paragraph [187]. Analysing the BBH orbit shown in Fig. 4.1, the rotation of BH 2 affects the movement of BH 1. The rotation of BH 2 drags spacetime, causing a minimal impact on BH 1 in phases A and C, but inducing movement in the negative z-direction in phase B and in the positive z-direction in phase D. The same effect occurs with the impact of the rotation of BH 1 on BH 2. In this superkick configuration, both BHs experience the same induced velocity perpendicular to the orbital plane, causing the orbital plane to oscillate up and down with the orbital frequency. Although this motion alone does not produce much radiation, it does cause a blue shift in one direction and a red shift in the other, affecting the net Doppler shift. As the GW radiation causes the orbital radius to decrease, the Doppler shift increases until the time of the merger, affecting the net momentum radiated in the z-direction. Finally, the magnitude and direction of the out-of-plane kick during the merger depend on the explicit phase of the orbit at that moment.

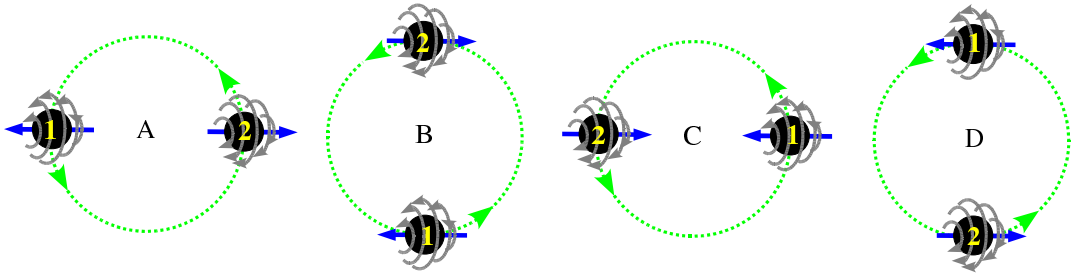

Figure 4.1: Four different orbital phases of the superkick configuration. The grey lines illustrates the frame-dragging of spacetime around the two rotating BHs, with spins pointing in the direction of the blue arrows. The depiction is taken from Fig. 5 in the lecture notes of Frans Pretorius [187].

Equal-mass binaries with a small spin component in the direction of the orbital angular momentum, but anti-parallel in the in-plane spin component, are called *hangup kick* configurations. These configurations have been found by Lousto et al. to have a maximum kick velocities of about 5000 km/s [30, 183]. These configurations combine the frame-dragging effects of the superkick configuration and the orbital hangup effect to increase the duration of the linear momentum flux in addition to the energy and angular momentum flux. *Ultimate kicks* up to 27 000 km/s, nearly 9 % of the speed of light, can be generated when eccentricity is included in the BBH orbits [188].

4.2 Centre-of-mass trajectory

During the inspiral and merger of a BBH system, the emission of linear momentum $\vec{P}$ in GWs leads to a motion of the centre-of-mass of the binary system. The trajectory of the centre-of-mass is given by $\vec{x}(t) = \int_{-\infty}^{\infty} \mathrm{d}t\, \vec{v}(t)$, where the time series of the kick velocity is defined by

$$\vec{v}(t) = -\frac{P_x(t)\,\hat{x} + P_y(t)\,\hat{y} + P_z(t)\,\hat{z}}{M(t)}\,, \tag{4.1}$$

due to linear momentum conservation. In other words, the momentum of the final BH is balanced by the momentum of the centre-of-mass of the merged system. The mass of the binary is time-dependent due to the emission of energy, but it can be shown that the final BH mass M_f can be expressed in units of the total mass M of the binary at early times [184]. As a result, M is just a scaling factor of the centre-of-mass trajectory, and the kick velocity is independent of the total mass.

In Fig. 4.2 the interplay of spin precession and mass asymmetry leads to a complicated motion of the centre-of-mass trajectory. The final kick velocity is given by $\vec{v}_f = \lim_{t\to\infty} \vec{v}(t)$. For the particular configuration described in the caption of the figure the final kick reaches a value of $|\vec{v}_f| \approx 1267\,\mathrm{km/s}$, mostly out of the orbital plane in the negative z-direction. This is already more than twice the escape velocity of our Milky Way [189]. The flux of linear momentum

is insignificant in the early stages, and the kick is only accumulated in the last few cycles before the merger. This is consistent with the build-up of the anti-symmetric waveform in the merger-ringdown regime.

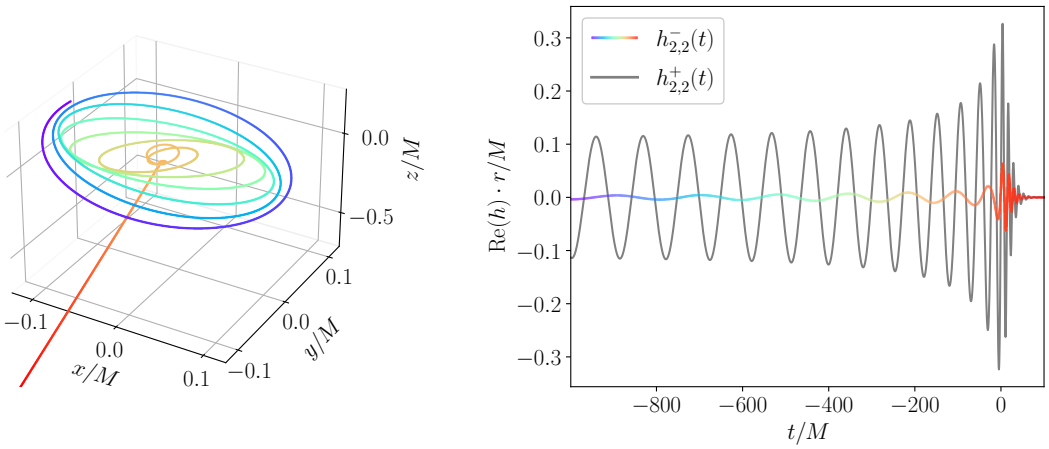

Figure 4.2: Centre-of-mass trajectory taken from moving puncture data computed with the `BAM` code for a $q = 2$ configuration with only the heavier BH spinning [54]. In the right panel the corresponding dominant $+/-$ waveform generated with `NRSur7dq4` is shown. The spin is defined at a reference frequency of $\omega_{orb} \approx 0.23\,\mathrm{rad/M}$ with $|\vec{\chi_1}| = 0.6$, $\theta_1 = \pi/2$ and $\phi_1 = \pi/2$. The rainbow colour indicates the time evolution from $t = -1000\,M$ until $t = 100\,M$. The final kick direction is the straight reddish line in the negative z-direction.

4.3 Effect of the spin direction on the kick mode-asymmetry correlation

In order to obtain a first quantitative relationship between the anti-symmetric waveform and the kick velocity, in this chapter we analyse the influence of the spin direction close to the merger. Therefore, we consider equal-mass BBH configurations with only one BH spinning with a high fixed spin magnitude of $\chi = 0.8$ and choose 2^{16} equally spaced sample points on the sphere, i.e. the spin angles are chosen from $\theta \in [0, \pi]$ and $\phi \in [0, 2\pi]$. We choose these configurations because the highest kick velocities for quasi-circular BBH orbits are expected for two maximally-spinning BHs and of equal mass [30, 183]. Focusing on the spin direction of only one BH simplifies considerations of the anti-symmetric waveform. In Fig. 4.3 the results are visualised by a scatter plot of the recoil velocity $v = |\vec{v}_f|$ versus the maximum value of the (2, 2) anti-symmetric amplitude $\hat{a}^-$ as defined in Eq. (3.9), which we will sometimes refer to as "asymmetry" for simplicity. Each point corresponds to one configuration from the sample set. The colours of the points indicate the in-plane spin component, i.e. the component of the spin perpendicular to the orbital angular momentum $\chi^{\perp} = \sin(\theta) \cdot \chi$.

Indeed, we can confirm the intuitive assumption that the kick velocity calculated with the surrogate model `NRSur7dq4Remnant` increases as the asymmetry calculated from `NRSur7dq4` waveforms increases. The linear dependence of the asymmetry on $\chi^{\perp}$, which we have already found in sec. 3.4, is clearly visible by the colour gradient from left to right.

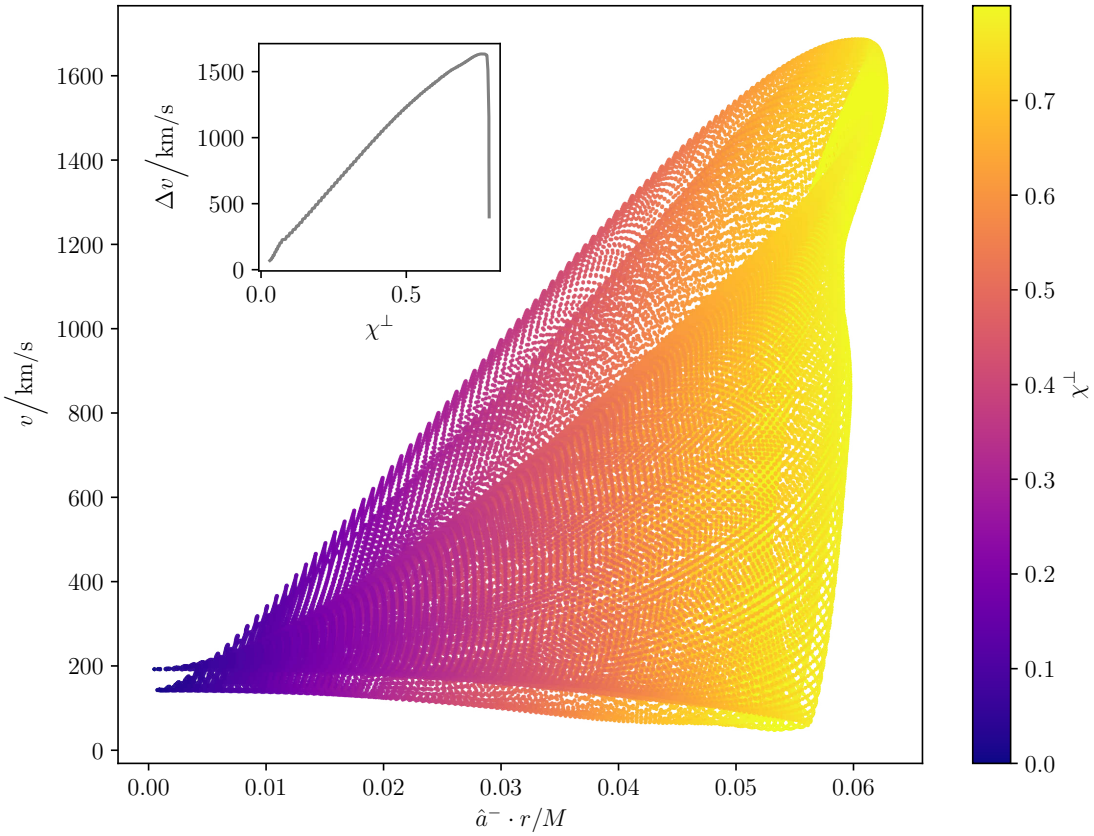

Figure 4.3: Relation between the magnitude of the kick velocity v and the peak amplitude of the dominant anti-symmetric waveform $\hat{a}^-$ for 2^{16} equal-mass BBH configurations with the spin specified at $t_{ref} = -100\,M$ placed on one BH. The colour map indicates the in-plane spin magnitude $\chi^\perp$. The inset shows the difference between the maximum and minimum kick velocity for 1024 vertical lines in the main plot versus the mean of $\chi^\perp$ in each line. The waveforms and remnant BH properties are calculated via `NRSur7dq4` and `NRSur7dq4Remnant`.

If we look at the three corners of the triangular shaped plot, we can see some interesting properties that are not so intuitive. Starting with the lower right corner, it should be noted that such configurations with very small recoil but strong anti-symmetric GW emission exist at all. There must be other quantities and relations between them, than just $a_{2,2}^{-;copr}(t)$ that affect the linear momentum emission. We will have a closer look at configurations in this corner in sec. 4.5.

The upper right corner consists of configurations with very high kicks and a strong asymmetry. There are two surprising facts. The first is that the global maximum of 1684 km/s is reached by a configuration where the spin is not completely in the plane. Consequently, the asymmetry does not reach the global maximum. This is consistent with the concept of the hangup kick configurations mentioned in sec. 4.1. These configurations combine the in-plane spin effect, which maximises the anti-symmetric waveform, and the orbital hangup effect, which maximises the duration of the GW emission due to the partial alignment of

the spin with the orbital angular momentum. The second interesting fact about the upper right corner is obtained by plotting the difference between the maximum and minimum kick velocity $\Delta v = |\vec{v}_f^{\,max}| - |\vec{v}_f^{\,min}|$ against the in-plane spin magnitude $\chi^\perp$. To generate this plot, we imagine vertical lines of small width in the scatter plot, i.e. constant asymmetry values, and calculate from the configurations intersecting the vertical line the mean value of $\chi^\perp$ and Δv. We observe an almost linear dependence, i.e. the higher the in-plane spin value, the wider the range of possible kick velocities. This indicates an increasing influence of the angle ϕ between the separation vector and the spin on the kick as $\chi^\perp$ increases, since ϕ is the only free quantity in this plot. In other words, ϕ must significantly modulate the maximum achievable kick value, which is determined by $\chi^\perp$ and thus by the anti-symmetric amplitude. At the far right of the inset plot Δv drops rapidly. These are very specific configurations with maximum asymmetry, due to a combination of maximum in-plane spin and a specific angle ϕ that maximises the asymmetry. This is consistent with the observation of small oscillations of the asymmetry with respect to ϕ in Fig. 3.7. So here ϕ takes a particular value, which is a peak of the small asymmetry oscillations, and thus there is no ϕ-modulation of the kick amplitude, which in turn leads to almost zero Δv.

In the lower left corner of Fig. 4.3 we see a split into two lines of constant velocity. To better understand where this split comes from, we generate Fig. 4.4. Therefore three vertical lines in Fig. 4.3 for a very small, a medium and a high constant asymmetry are notionally drawn. The lines have a small width of less than 15 % of the constant asymmetry value in order to intersect with enough points, since we are dealing with a discretised space. The intersecting points then have three free parameters left to analyse, the two spin angles and the kick velocity.

The first row in Fig. 4.4 is now exactly the case of the lower left corner of Fig. 4.3, i.e. an almost vanishing anti-symmetric waveform. We see a clear separation into two lines at $\theta = 0$ and $\theta = \pi$. This means that we have non-precessing configurations with the BH spin aligned, $\chi_z = +0.8$, or anti-aligned with the orbital angular momentum $\chi_z = -0.8$. The anti-aligned spin case has the slightly higher kick velocity of about 195 km/s compared to the aligned case with about 150 km/s. This difference can be explained by looking at the second order kick PN expression for spins collinear with the orbital angular momentum. Eq. (4.30) of Ref. [190] is where this expression was explicitly written down by Racine et al. Since we are using an equal-mass single-BH spinning configuration, we have to substitute the mass difference $\delta m = 0$, the symmetric mass ratio $\eta = 1/4$, the constant total spin $|\boldsymbol{S}^c|/m_1^2 = \chi_z$ and the constant spin difference $|\boldsymbol{\Delta}^c|/m_1^2 = -\chi_z$. The reader will find the precise definitions of these four quantities in the reference. Simplifying the above-mentioned Eq. (4.30) as proposed by Racine et al., we observe that there is no kick out of the plane, and the in-plane kick velocity

has a value of

$$\vec{v}_f = -\frac{29}{105}\,x^4\left(\chi_z\left(\frac{7}{29}\,x^{1/2} - \frac{18}{29}\,x^{3/2} + \frac{21\pi}{29}\,x^2\right) - \chi_z^2\,x^2\right)\hat{n}\,. \tag{4.2}$$

Here $\hat{n}$ is the normalised separation vector and x is the PN expansion parameter. What we now learn is that for the aligned-spin case with $\chi_z = +0.8$ the $\sim \chi_z$ and $\sim \chi_z^2$ terms have opposite signs, leading to a small kick velocity. On the other hand, in the anti-aligned case with $\chi_z = -0.8$, both terms have a negative sign, resulting in an effective addition of both terms and thus a higher kick.

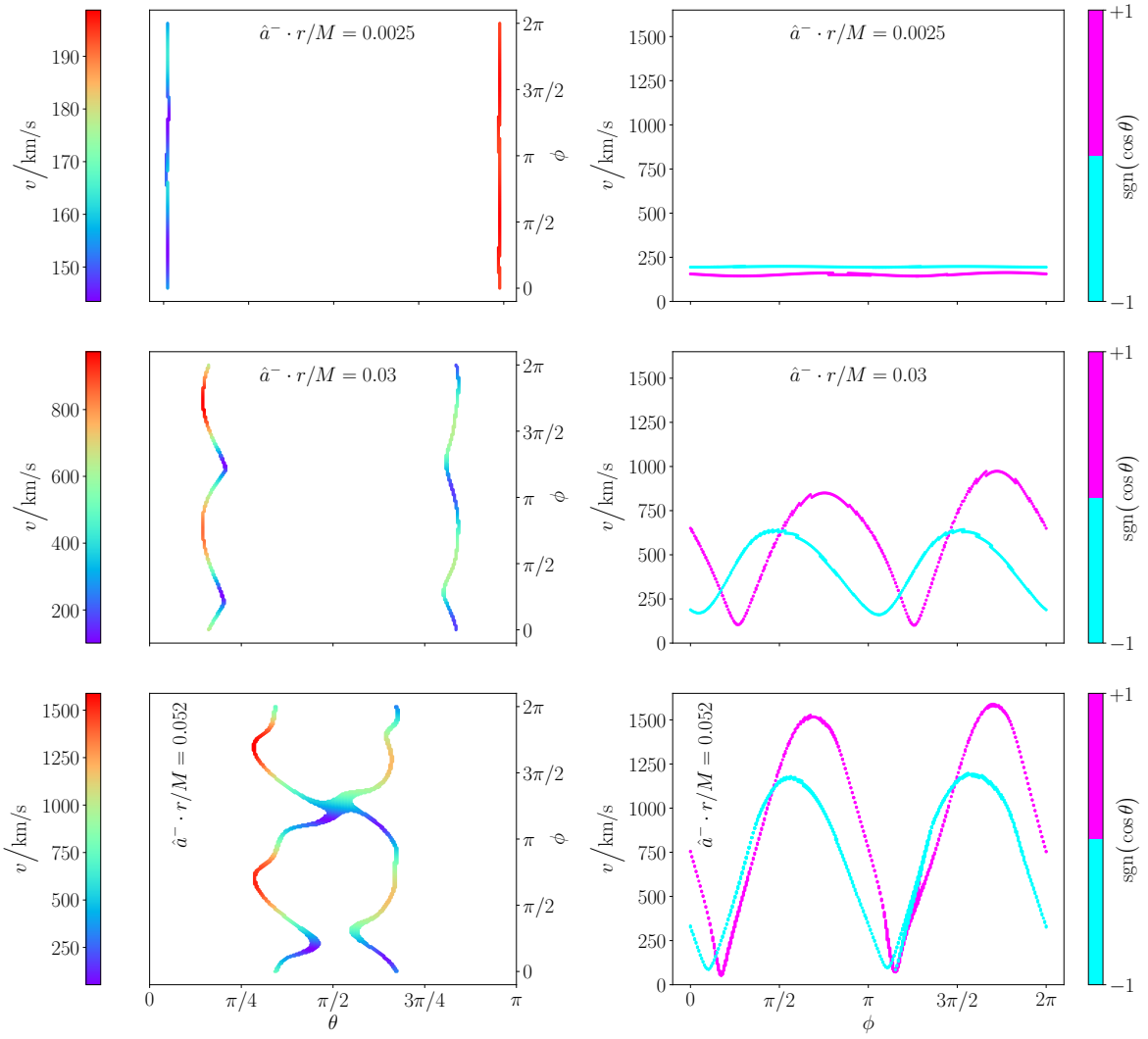

Figure 4.4: Spin polar angle θ, azimuthal angle ϕ and kick velocity magnitude v relations for a small, medium and high constant anti-symmetric peak amplitude $\hat{a}^- \cdot r/M \in \{0.0025, 0.03, 0.052\}$. The peak amplitude increases from the first to the last row. The colour bars in the left column have different scales to better show the relative colour gradient on the lines of the different spin angle configurations. The right column shows the sinusoidal dependence of the kick velocity on ϕ. The magenta lines correspond to BBH configurations with the spin above the orbital plane $v^{+1}(\phi)$, while the cyan lines correspond to configurations with the spin below the orbital plane $v^{-1}(\phi)$.

Increasing $\hat{a}^-$ causes the two spin angle lines to move towards $\theta = \pi/2$ until they are so close together that they connect in a circularly shape, as can be seen in the left column of Fig. 4.4. The fact that some irregular circular shapes are formed and that the straight lines in the upper left plot do not remain straight until connecting in $\theta = \pi/2$ is another indication that the anti-symmetric amplitude must also depend on ϕ, especially in the merger regime, as already mentioned in sec. 3.3. Another thing we can learn when increasing the asymmetry is from the rainbow colour gradient, which indicates the magnitude of the kick velocity. There is a sinusoidal pattern of the colours with respect to ϕ. The amplitude of the redness increases with $\hat{a}^-$, as can be seen from the scales of the colour bars on the left in each row of Fig. 4.4. Also, the redness is stronger on the left side of $\theta = \pi/2$ compared to the right side, and the points of maximum redness are at different ϕ on the left and right sides. The graphical representation of these descriptions are the plots in the right column of Fig. 4.4. In more mathematical words the kick velocity has a sinusoidal dependence on the in-plane angle. There are two sinusoids $v^{\pm 1}(\phi)$ for configurations with the spin above or below the orbital plane, which is characterised by the sign of $\cos\theta$. The amplitude of both $v^{\pm 1}(\phi)$ increase linearly with the asymmetry. The phase shift between v^{-1} and v^{+1} decreases with $\hat{a}^-$. At maximum asymmetry, which corresponds to an infinitesimal region around $\theta = \pi/2$, the phase shift is zero and $v^{+1}(\phi) = v^{-1}(\phi)$. To explain the sinusoidal dependence of the kick on the in-plane spin, we refer to Ref. [179], which first developed a model to predict the kick velocity, and to further studies by the group [134, 191–195]. The fact, that there are two sinusoids is that for a constant asymmetry always two out-of-plane angles are responsible since $\hat{a}^- \sim \sin(\theta)$ and the sin function is symmetric around $\theta = \pi/2$. v^{+1} has a higher amplitude than v^{-1} due to the orbital hangup effect mentioned above. This is counterintuitive to the PN argument made in Eq. (4.2), but remember that PN only gives possible trends from the insperial regime, whereas the orbital hangup effect is a full GR effect.

Besides the references given in the last paragraph, to understand the interaction between v, θ and ϕ, the reader can have a closer look at the variation of the kick velocity with the out-of-plane spin θ in Fig. 4.5. The six plots show the $v(\theta)$ profile of configurations with six different but fixed in-plane angles $\phi \in \{0, \pi/5, 2\pi/5, 3\pi/5, 4\pi/5, \pi\}$. Therefore configurations from Fig. 4.3 with an in-plane spin close to the six chosen ϕ-values are picked. From the colours we can again deduce that the peak asymmetry $\hat{a}^-$ is maximised for spins completely in the plane, which can be seen by the fact that the maximum redness is always at $\theta = \pi/2$. As expected, since we have only a single BH spinning system, the $v(\theta)$ maps are π-periodic in the rotation of the in-plane spin, which is consistent with the π-periodicity of the plots in the right column of Fig. 4.4. The maximum kick is reached in the plot for $\phi = 3\pi/5$ at about $\theta \approx 85°$, which is again a hangup kick configuration, a combination of frame-dragging maximisation, which is responsible for superkicks, and the hangup effect, which increases the energy emission.

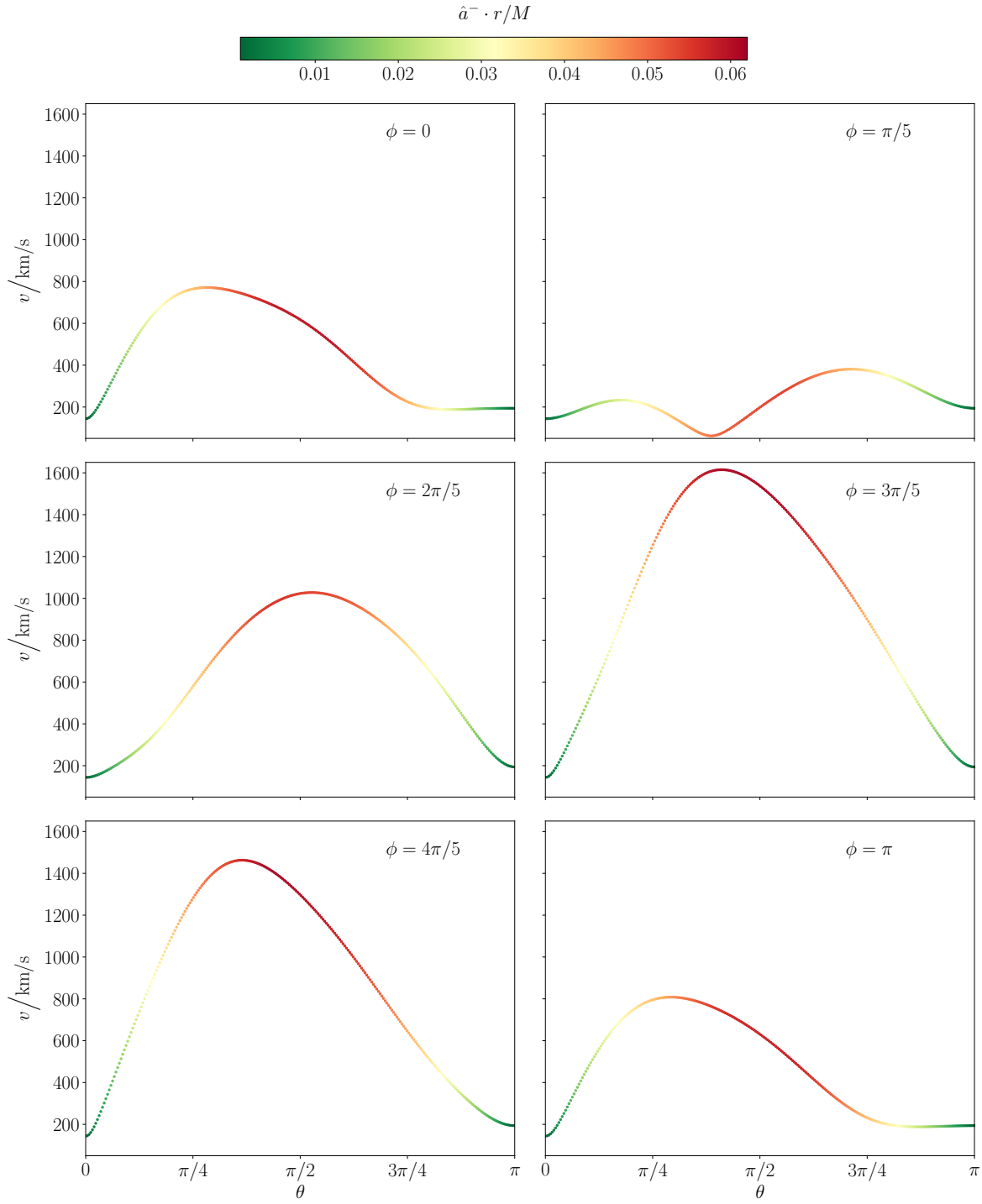

Figure 4.5: Effect of the polar angle θ on the kick velocity v for six different but fixed azimuthal angles ϕ. The relation of v and θ is π-periodic in ϕ, i.e. the plots in the upper left corner and lower right corner are equal. The colours indicate the dominant anti-symmetric peak amplitude. The highest peak amplitude is always reached when the spin is completely in the plane, so $\theta = \pi/2$. This is not the case for the kick velocity, where the peak also depends on ϕ.

4.4 Expressing the linear momentum flux through +/− waveform quantities

The transfer of linear momentum only occurs if there is an asymmetric energy distribution in the emitted waves, i.e. studying the mode asymmetry in GWs can help us to understand where the recoil comes from. Since mis-aligned systems lead to an out-of-plane kick and to higher asymmetries, we will focus here on the derivation of the z-component of the linear momentum flux in terms of the dominant +/− waveform. We therefore explain the calculations in chapter III of Ruiz et al. [46], adapt them to our notation, and include ideas from a non-public transcript by Shrobana Ghosh. We start with the linear momentum flux function in Eq. (2.33) and use $\Psi_4 = -\ddot{h}$ to get

$$\begin{aligned}\frac{\mathrm{d}P_z}{\mathrm{d}t} &= \lim_{r\to\infty} \frac{r^2}{16\pi} \oint \mathrm{d}\Omega\, l_z \left|\dot{h}\right|^2 \\ &= \lim_{r\to\infty} \frac{r^2}{16\pi} \oint \mathrm{d}\Omega\, l_z \left(\int_{-\infty}^{t} \mathrm{d}t'\, \Psi_4(t', r) \right) \left(\int_{-\infty}^{t} \mathrm{d}t'\, \Psi_4^*(t', r) \right) .\end{aligned} \tag{4.3}$$

We can now use the spherical harmonic expansion of Ψ_4 in Eq. (2.66). The property that the strain is in first order anti-proportional to the distance from source r, also holds for the expansion coefficients $\psi_{\ell,m}(t, r)$. So $\psi_{\ell,m}(t, r) \approx \psi_{\ell,m}(t)/r$ and we get rid of the limit in Eq. (4.3):

$$\frac{\mathrm{d}P_z}{\mathrm{d}t} = \frac{1}{16\pi} \sum_{\ell,m} \sum_{\ell',m'} \oint \mathrm{d}\Omega\, {}^{-2}Y_{\ell,m}\, {}^{-2}Y^*_{\ell',m'}\, l_z \left(\int_{-\infty}^{t} \mathrm{d}t'\, \psi_{\ell,m}(t') \right) \left(\int_{-\infty}^{t} \mathrm{d}t'\, \psi^*_{\ell',m'}(t') \right) . \tag{4.4}$$

To calculate the integral over the sphere, we can express the z-component of the radial unit vector as

$$l_z = \cos\theta = 2\sqrt{\frac{\pi}{3}}\, Y_{1,0} \tag{4.5}$$

where $Y_{\ell,m}$ are the common spin zero spherical harmonics. So we now have an integral over three SWSH in the form of

$$\begin{aligned}&\oint \mathrm{d}\Omega\, {}^{s_1}Y_{\ell_1,m_1}\, {}^{s_2}Y_{\ell_2,m_2}\, {}^{s_3}Y_{\ell_3,m_3} \\ &= \sqrt{\frac{(2\ell_1+1)(2\ell_2+1)(2\ell_3+1)}{4\pi}} \begin{pmatrix} \ell_1 & \ell_2 & \ell_3 \\ -s_1 & -s_2 & -s_3 \end{pmatrix} \begin{pmatrix} \ell_1 & \ell_2 & \ell_3 \\ m_1 & m_2 & m_3 \end{pmatrix} ,\end{aligned} \tag{4.6}$$

where we have written down the solution of the integral to the right of the equal sign, which involves Wigner 3-ℓm symbols. These Wigner 3-ℓm symbols are related to the Clebsch-Gordan coefficients from quantum mechanics, which in turn can be expressed in a closed form [63]. Since the complex conjugate of SWSH is given by

$${}^{s}Y^*_{\ell,m} = (-1)^{s+m}\, {}^{-s}Y_{\ell,-m}\,, \tag{4.7}$$

we have in the case of Eq. (4.4) $s_1 = -2$, $s_2 = 2$, $s_3 = 0$, $\ell_1 = \ell$, $\ell_2 = \ell'$, $\ell_3 = 1$, $m_1 = m$, $m_2 = -m'$ and $m_3 = 0$. In this special case the closed form of the Wigner matrices (Eq. (A24) in Ref. [46]) involves Kronecker deltas that are only non-vanishing for $m = m'$, $\ell = \ell'$, $\ell = \ell'+1$ and $\ell = \ell' - 1$. Thus the two sums in Eq. (4.4) can be simplified to one sum over $\ell \geq 2$ and $-\ell \leq m \leq +\ell$. So we have

$$\begin{aligned}\frac{\mathrm{d}P_z}{\mathrm{d}t} = \frac{1}{16\pi}\sum_{\ell,m}\Bigg(\int_{-\infty}^{t}\mathrm{d}t'\,\psi_{\ell,m}(t')\Bigg) \\ \cdot\left(\int_{-\infty}^{t}\mathrm{d}t'\,\left(c_{\ell,m}\,\psi^*_{\ell,m}(t') + d_{\ell,m}\,\psi^*_{\ell-1,m}(t') + d_{\ell+1,m}\,\psi^*_{\ell+1,m}(t')\right)\right),\end{aligned} \tag{4.8}$$

where the coefficients are given by

$$c_{\ell,m} = \frac{2m}{\ell(\ell+1)} \tag{4.9}$$

$$d_{\ell,m} = \frac{1}{\ell}\sqrt{\frac{(\ell-2)(\ell+2)(\ell-m)(\ell+m)}{(2\ell-1)(2\ell+1)}}\,. \tag{4.10}$$

Note that $\int \mathrm{d}t'\psi_{l,m}(t') = -\dot{h}_{l,m}(t)$. We now calculate the sum until $\ell = 2$ and keep only combinations with exclusively $\ell = 2$ and $m = \pm 2$ modes. Then we can rewrite Eq. (4.8) as

$$\frac{\mathrm{d}P_z}{\mathrm{d}t} = \frac{1}{16\pi}\left(\frac{2}{3}\,\dot{h}_{2,2}\dot{h}^*_{2,2} - \frac{2}{3}\,\dot{h}_{2,-2}\dot{h}^*_{2,-2}\right). \tag{4.11}$$

With the definitions in Eq. (3.1) and in Eq. (3.7) we can express the dominant modes for a precessing system in terms of the $+/-$ amplitude and phase:

$$h_{2,2}(t) = a^+_{2,2}(t)\,e^{i\phi^+_{2,2}(t)} + a^-_{2,2}(t)\,e^{i\phi^-_{2,2}(t)} \tag{4.12}$$

$$h_{2,-2}(t) = a^+_{2,2}(t)\,e^{-i\phi^+_{2,2}(t)} - a^-_{2,2}(t)\,e^{-i\phi^-_{2,2}(t)}. \tag{4.13}$$

Calculating the derivatives with the chain rule give:

$$\dot{h}_{2,2} = \left(\dot{a}^+_{2,2} + i\dot{\phi}^+_{2,2}\,a^+_{2,2}\right)e^{i\phi^+_{2,2}} + \left(\dot{a}^-_{2,2} + i\dot{\phi}^-_{2,2}\,a^-_{2,2}\right)e^{i\phi^-_{2,2}}\,, \tag{4.14}$$

$$\dot{h}_{2,-2} = \left(\dot{a}^+_{2,2} - i\dot{\phi}^+_{2,2}\,a^+_{2,2}\right)e^{-i\phi^+_{2,2}} - \left(\dot{a}^-_{2,2} - i\dot{\phi}^-_{2,2}\,a^-_{2,2}\right)e^{-i\phi^-_{2,2}}\,. \tag{4.15}$$

Substituting these into Eq. (4.11) and suppressing the subscript "$2,2$" for better reading, we find that:

$$\begin{aligned}\frac{\mathrm{d}P_z}{\mathrm{d}t} = \frac{1}{6\pi}\Big(\left(\dot{a}^-\dot{a}^+ + a^-a^+\dot{\phi}^-\dot{\phi}^+\right)\cos(\phi^- - \phi^+) \\ - \left(a^-\dot{a}^+\dot{\phi}^- - \dot{a}^-a^+\dot{\phi}^+\right)\sin(\phi^- - \phi^+)\Big)\,.\end{aligned} \tag{4.16}$$

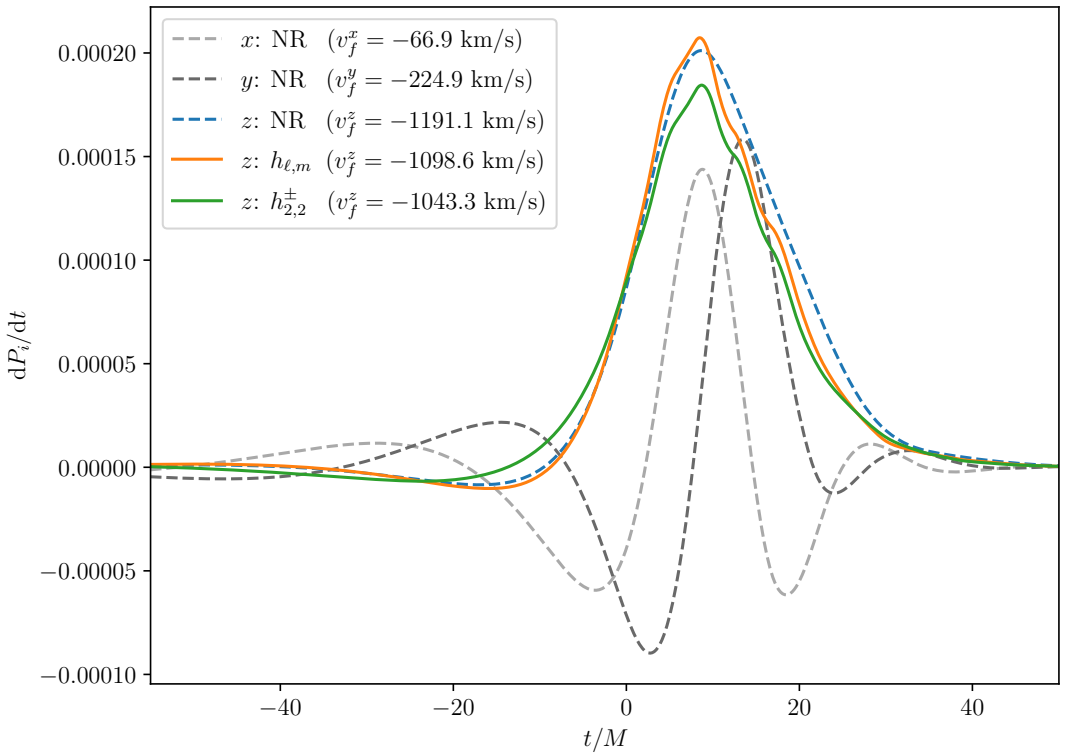

Figure 4.6: Linear momentum fluxes for the same configuration as in Fig. 4.2. The dashed lines are the momenta extracted at $r = 120\,M$ calculated with the `BAM` code [54] and are therefore the most accurate. The orange line is calculated using Eq. (2.33) and includes all available modes up to $\ell = 4$, where the modes are taken from the `NRSur7dq4` model as only Ψ_4 data are available in the `BAM` simulation. The green line is calculated using Eq. (4.16). As a sanity check of the calculations in this chapter, the reader can include only the $h_{2,\pm2}$ modes in Eq. (2.33) and see that the orange line would exactly overlie the green one, because Eq. (2.33) and Eq. (4.16) are equivalent for $\ell = 2$ and $m = \pm2$. In the brackets in the legend the kick velocity is given, which is nothing else than the negative of the integral over the full momentum time series. The kick in the x- and y-directions is suppressed, since the grey lines have stronger oscillations compared to the coloured lines. The inaccuracies in the v_f^z due to the surrogate modes, the limited integration bounds and the non-inclusion of all modes are in an acceptable range, considering the most recent accurate remnant model `NRSur7dq4Remnant` [24] give an out-of-plane kick of $v_f^z = -1116.3\,\mathrm{km/s}$ and have a 95th percentile error of $\sim 120\,\mathrm{km/s}$.

To the best of our knowledge, this relationship between the linear momentum flux and the dominant +/− waveform quantities has not been reported elsewhere. We can immediately see from this equation that when the anti-symmetric waveform is switched off, i.e. $a^-(t) = 0$, the out-of-plane recoil disappears, since the out-of-plane kick is given by

$$v_f^z = -\int_{-\infty}^{\infty} \mathrm{d}t \, \frac{\mathrm{d}P_z}{\mathrm{d}t} \Big/ M_f \,. \tag{4.17}$$

Notice two small sources of error when calculating the kick velocity in units of the total mass M by numerically integrating over Eq. (4.16). Since we only have a limited waveform time series, a small integration error occurs. In addition there are higher order corrections from

the subdominant $+/-$ waveforms. Nevertheless, in Fig. 4.6 and the following sections, we can explore the power of considering only these dominant waveform quantities. Further relations for the energy, linear momentum and angular momentum fluxes in terms of the dominant and subdominant $+/-$ waveforms can be derived using the same approach. However, deciding which relationship is worth investigating in terms of mode asymmetries and the final analysis of these expressions will require some future work.

4.5 Influence of the $+/-$ phase difference

So far, we can only state with the equation derived in the last sec. (4.16), that the merged BH indeed recoils due to mode asymmetries. But as we have seen in sec. 4.3, the recoil depends crucially on the spin direction. The strong dependence on the spin direction was also observed in sec. 3.3 for the anti-symmetric waveform. So it is reasonable to assume that there is a correlation between the two dependencies. The aim of this chapter is to further understand the different terms in the Eq. (4.16) between the out-of-plane linear momentum flux and the $+/-$ waveform quantities. Therefore, we take two configurations with equal masses and one BH spinning from Fig. 4.3. We choose a configuration in the lower right corner, which has the characteristics of a low kick velocity but high asymmetry (LKHA). The second configuration is in the upper right corner, so one with a high kick velocity but the same high asymmetry (HKHA). We make two hypotheses about their different kick velocities. First, the asymmetries vary only in phase, which means that the phase evolution is different for the two cases, and the final kick occurs at different phases in the motion of the precessing orbital plane. Consequently, the final kick is influenced by the phase at which the kick happens. Secondly, the two asymmetries actually differ in amplitude. These differences are barely discernible in the PN equations, but become more pronounced near the merger, making them perceptible in full NR waveforms.

The top panel of Fig. 4.7 shows the real part of the dominant $+/-$ waveform of both configurations in the coprecessing frame. Both the symmetric and the anti-symmetric amplitudes are of comparable order of magnitude. But we can already see just from the waveforms of LKHA and HKHA that in the merger-ringdown regime, which is mainly responsible for the final kick, the phase shift between their anti-symmetric and symmetric waveforms is different. In the LKHA case for $t \gtrsim -20\,M$ a peak of the anti-symmetric waveform is at the same time as a zero crossing of the symmetric waveform, i.e. there is a $\pi/2$ phase difference between them. For the HKHA case, we observe a π phase difference because a maximum of the anti-symmetric waveform is at the same time as a minimum of the symmetric waveform and vice versa.

Before we explain that the phase difference between the $+/-$ waveform is indeed mainly responsible for the different high kick values, let us have a look at the kick time series we get by expressing Eq. (4.17) as a function of the upper integration limit and assuming $M \approx M_f$.

In the lower panel of Fig. 4.7 we observe, that the LKHA configuration has a kick profile $v_z(t)$, which shows a *antikick*, i.e. there is a significant difference between the maximum kick and the final kick velocity [196]. The HKHA kick profile, on the other hand, does not fall back on low velocities.

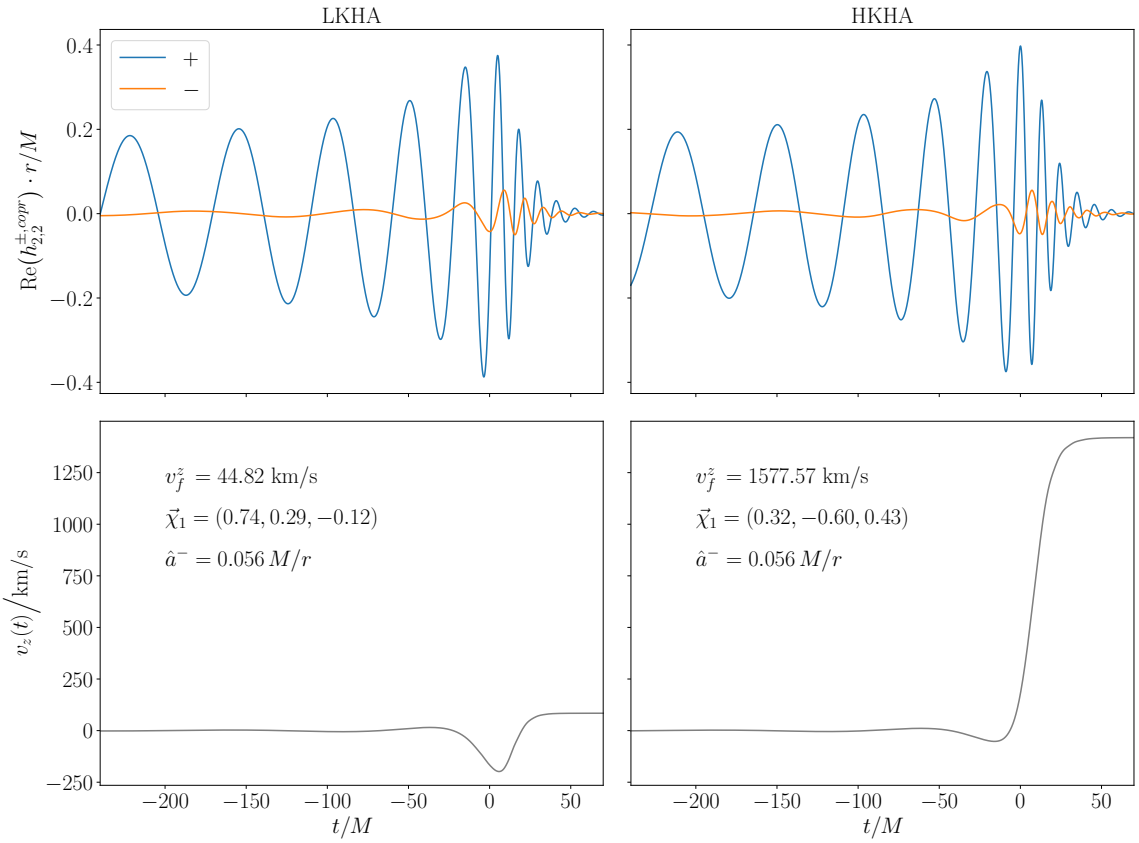

Figure 4.7: Real part of the dominant +/− waveforms in the coprecessing frame and the kick profile $v_z(t)$ for two $q = 1$ configurations, LKHA and HKHA, with one BH spinning, where the spin $\vec{\chi}_1$ is defined at $t_{ref} = -100\,M$. The two configurations have a similar high asymmetry amplitude $\hat{a}^-$, but differ in their final out-of-plane kick velocity v_f^z, since there is a different phase difference between the anti-symmetric and symmetric waveform.

We will now try to find an explanation for these phenomena by splitting Eq. (4.16) into four individual amplitude terms: $\dot{a}^-\dot{a}^+$, $a^-a^+\dot{\phi}^-\dot{\phi}^+$, $a^-\dot{a}^+\dot{\phi}^-$ and $\dot{a}^-a^+\dot{\phi}^+$. Therefore we plot in the upper left of Fig. 4.8 the four terms without the overall prefactor $1/6\pi$ and without the sine and cosine oscillations. For both, the LKHA and HKHA configuration, we find that the $a^-a^+\dot{\phi}^-\dot{\phi}^+$ term is the most dominant one, which we could also observe for all other precessing configurations at least in the seven-dimensional parameter space covered by `NRSur7dq4`. The difference between this term and the other three is that it is independent of the amplitude derivatives $\dot{a}^\pm$, which have the smallest order of magnitude compared to $a^\pm$ and $\dot{\phi}^\pm$. This can be seen in the upper right plot of Fig. 4.8. Note that in this plot we deliberately omit the units. We get $a^\pm$ in units of M/r, $\dot{a}^\pm$ in r and $\dot{\phi}^\pm$ in rad/M. However, in Eq. (4.16) the total

mass M cancels out when you multiply everything together. The dependence on the distance r cancels as well, since there is a total r^2 in Eq. (4.3), which we have ignored in the derivation of Eq. (4.16) with the argument that the strain is approximately proportional to $1/r$. Another argument for the dominance of the $a^- a^+ \dot{\phi}^- \dot{\phi}^+$ term is, that it is always positive, since the amplitude $a^\pm$ of a complex quantity and the combination $\dot{\phi}^- \dot{\phi}^+$ is always non-negative. The latter is true because the phase derivatives $\dot{\phi}^\pm$ become approximately equal in the merger-ringdown regime, as we have already suggested in sec. 3.2.3. Thus the area under $a^- a^+ \dot{\phi}^- \dot{\phi}^+$ is always non-negative, i.e. the linear momentum is not cancelled out by integration over oscillations in the flux, as could happen with the other terms.

It is interesting to note that the dominant terms for the LKHA and the HKHA configuration are at relatively the same high level, since their $+/-$ amplitudes and $+/-$ phase derivatives are approximately equal, apart from small peak amplitude differences and small oscillations of $\dot{\phi}^\pm$. The biggest effect now comes from the multiplication of the dominant term with $\cos(\phi^- - \phi^+)$, as can be seen in the lower left plot of Fig. 4.8. For the HKHA configuration the cosine is extreme in the regime of the maximum contribution of $a^- a^+ \dot{\phi}^- \dot{\phi}^+$ around $t_{max} \approx 9\,M$. A multiplication of the dominant term with the cosine only leads to a reflection of the dominant term on the x-axis, since $\phi^- - \phi^+ \approx \pi$ for the region around t_{max} and thus the cosine is -1. The situation is quite different in the case of LKHA. Here the cosine makes a zero crossing at t_{max}, leading to a folding of the dominant amplitude term from positive to negative values. Integration over these oscillations results in a kick velocity close to zero. Finally, the bottom right plot shows the wrapped phase difference for both configurations. In fact, in the region around t_{max} that contributes most to the momentum flux, the phase difference is $\pi/2$ for LKHA and π for HKHA, which is consistent with our observation from the different phase evolution of the $+/-$ waveforms in Fig. 4.7. We can also observe that the phase difference becomes approximately constant for $t \gtrsim 9\,M$, which is consistent with what we have already stated in the last paragraph of sec. 3.2.3. There we found that the phase evolution of the symmetric and anti-symmetric waveform remains parallel and hence their derivatives $\dot{\phi^-} \approx \dot{\phi^+}$ become equal in the merger-ringdown regime.

In a nutshell, the kick velocity depends on a very specific interplay of the $+/-$ waveforms. First, the magnitude of the anti-symmetric and symmetric amplitudes are crucial. However, we have seen in sec. 3.3 that the symmetric amplitude in leading order depends mostly on the mass ratio, while the anti-symmetric amplitude depends strongly on the spin magnitude and the polar angle in addition to the mass ratio. So, for a constant mass ratio, we can say that the magnitude of the anti-symmetric amplitude is the decisive quantity for the maximum achievable kick velocity. But secondly, we also have to consider that in the merger regime there is no phase difference modulo π between ϕ^- and ϕ^+.

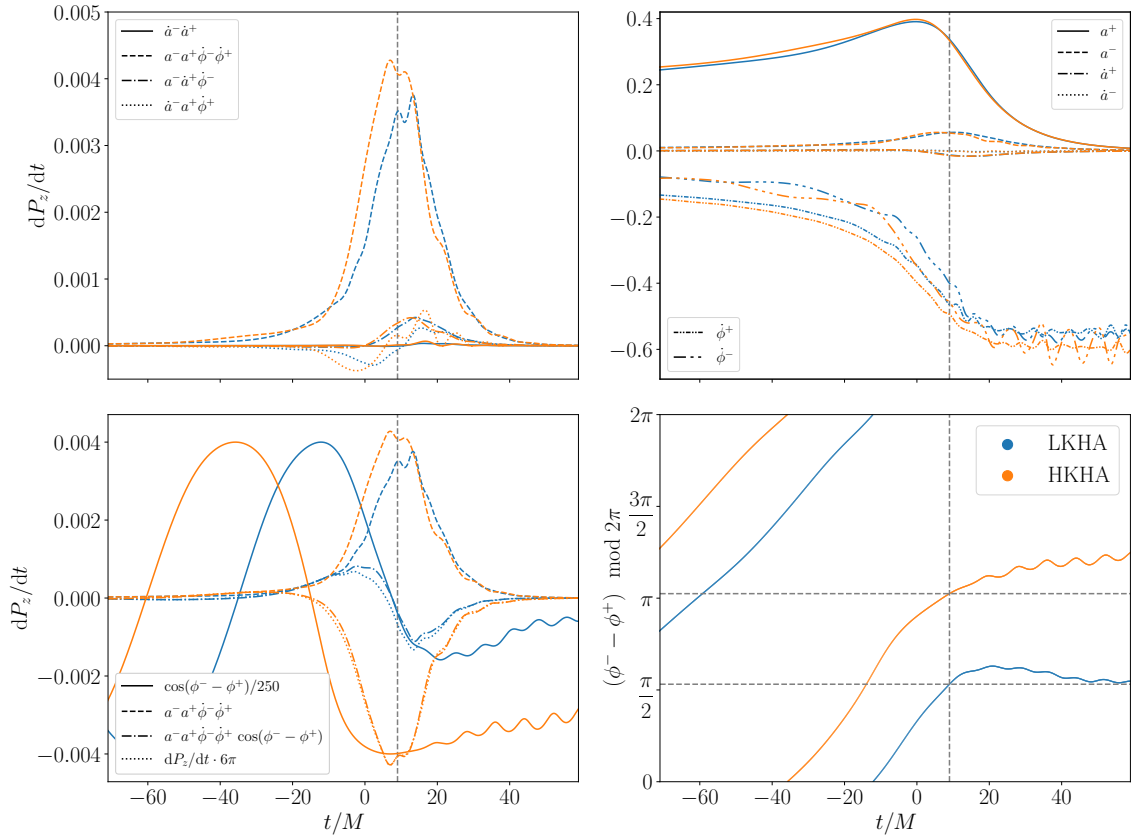

Figure 4.8: Analysis of the different components of the momentum flux defined in Eq. (4.16) for the same LKHA and HKHA configuration as in Fig. 4.7. The different line styles are used to represent different single terms of the Eq. (4.16). In the upper right plot, the bottom four lines correspond to $\dot{\phi}^{\pm}$, while the remaining lines are the amplitude $a^{\pm}$ and the small amplitude derivatives $\dot{a}^{\pm}$, respectively. The y-axis labels are dropped on porpuse as described in the text above. Note that in the lower left plot, the amplitude of $\cos(\phi^- - \phi^+)$ is scaled by $1/250$ for better visibility, and $\mathrm{d}P_z/\mathrm{d}t$ is scaled by 6π to compensate for the overall $1/6\pi$ factor in Eq. (4.16). The vertical grey dashed line indicates the time when the dominant term $a^-a^+\dot{\phi}^-\dot{\phi}^+$ is approximately maximal at $t_{max} \approx 9\,M$. At this time $\phi^- - \phi^+$ is approximately $\pi/2$ for LKHA and and π for HKHA, as indicated by the horizontal dashed lines in the lower right plot.

4.6 Correlation of in-plane spin rotation with the +/− phase difference

With our knowledge of the strong influence of the +/− phase difference on the out-of-plane kick velocity, we can now relate this to the sinusoidal kick dependence of superkick configurations on in-plane spin rotation. One could consider breaking the dependence on the phase differences further down to a dependence on the anti-symmetric phase only. For configurations with the same mass ratio and the same χ_{eff}, such as superkick configurations, this might work, because the contribution of the in-plane spin to the symmetric phase evolution is only at higher orders of the PN equations, as we saw in sec. 2.2.7. Thus $\phi^+(t)$ is relatively similar in all superkick cases. But since the momentum flux reaches its maximum in the merger-ringdown regime, we cannot use this PN assumption and we do not treat ϕ^+ as equal in all cases. We simply continue to analyse the difference $\phi^+ - \phi^-$ at t_{max}.

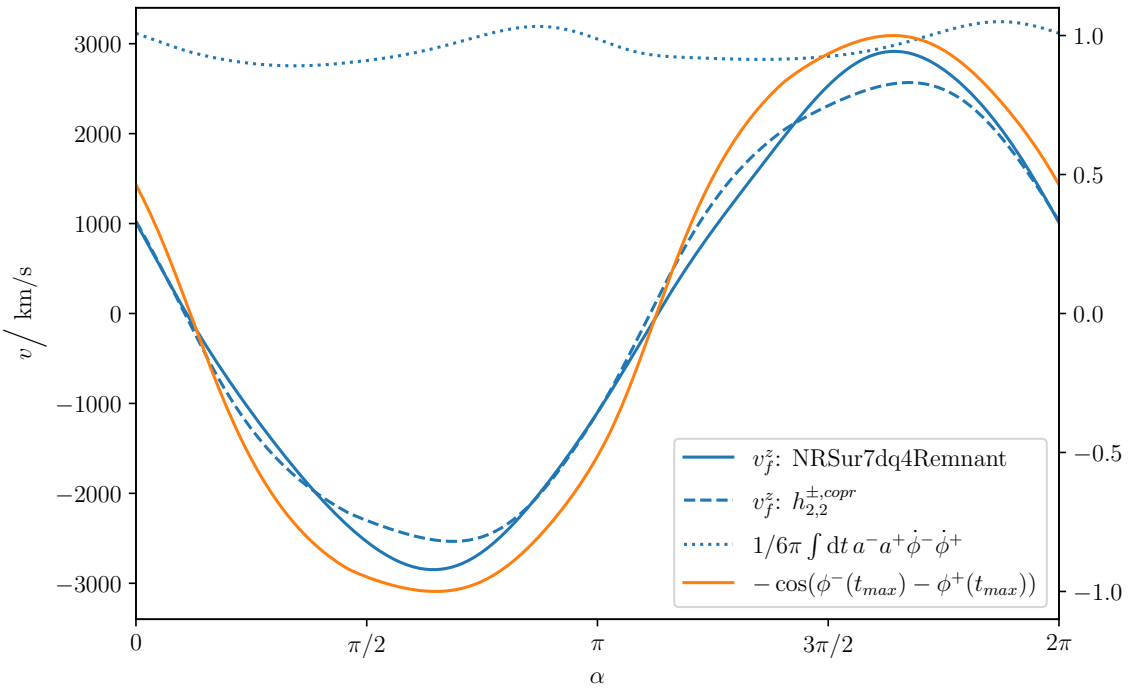

Figure 4.9: Out-of-plane recoil velocities for a series of superkick configurations rotated by an in-plane spin angle α. The blue lines belong to the left y-axis, while the orange line belongs to the right y-axis and is unitless. The solid blue line is calculated using the `NRSur7dq4Remnant` model and is assumed to be the most accurate. The dashed blue line is calculated using Eq. (4.16) and Eq. (4.17). It is in very good agreement with the solid line, considering that only (2, ±2) modes are included and that we can only integrate over a limited time series. The dotted line is the time integral over the dominant term $a^- a^+ \dot{\phi}^- \dot{\phi}^+$ in Eq. (4.16). The dominant term has a small dependence on α, but these oscillations are not responsible for a clear sinusoidal kick profile. Rather, the cosine of the phase difference $\phi^- - \phi^+$ in the merger-ringdown regime at about $t_{max} = 9\,M$ is the driving term for the integral evaluation, since $a^- a^+ \dot{\phi}^- \dot{\phi}^+$ is maximal at t_{max}.

Fig. 4.9 shows the out-of-plane kick velocity for binaries with dimensionless spins of $\vec{\chi}_1 = -\vec{\chi}_2 = 0.8 \cdot (\cos\alpha, \sin\alpha, 0)$ defined at $t_{ref} = -100\,M$, i.e. the same configurations we have already analysed in sec. 3.4. First, note again the good agreement in which the sinusoidal kick dependence on α can be reconstructed just by using $+/-$ waveform quantities in Eq. (4.16) by comparison with the more accurate `NRSur7dq4Remnant` prediction. As discussed in sec. 4.1 superkick configurations only lead to a very high kick velocity with a very specific orbital phase, i.e. depending on where exactly the merger occurs and whether the frame-dragging is constructive or destructive at that time. In other words, it is a question of finding the reference time to define the spins, which is directly at the point of merger, to relate the in-plane rotation α with the orbital phase. This question is not so easy to answer as we only have the waveform quantities and no information about when the apparent horizon of the remnant BH forms. However, it is not necessary to answer this question, as it would only result in a left or right shift of the overall sinusoidal kick behaviour, since the spin of superkick configurations remain opposite during spin evolution. So defining the spins at $t_{ref} = -100\,M$ is fine and we

just have to live with the fact that e.g. for $\alpha = 0$ the kick is not zero, as we would expect from the simple picture in Fig. 4.1 if t_{ref} were the exact merger time.

If we now analyse the rotation of the spins in the orbital plane with respect to the dominant term $a^- a^+ \dot{\phi}^- \dot{\phi}^+$ and with respect to the phase difference $\phi^- - \phi^+$ at the time of maximum linear momentum flux of the dominant term t_{max}, the final answer is that the +/− phase difference, which leads to different recoil velocities, is directly related to the in-plane spin rotation α. We can explore this in Fig. 4.9 by comparing the α-dependent kick profile with the cosine of the +/− phase difference at t_{max}, which has the same sinusoidal shape. Superkick configurations have almost no difference in the +/− amplitudes and phase derivatives, with the exception of minor oscillations associated with the azimuthal angle, as previously mentioned. Hence, the integral over the dominant term $\int \mathrm{d}t\, a^- a^+ \dot{\phi}^- \dot{\phi}^+$, which is the amplitude of the cosine, is almost constant with the α-variation. Graphically, one can imagine that multiplying the dotted blue line by the orange line gives the dashed line, except for the remaining three negligible small terms of Eq. (4.16). Note that the time integral over Eq. (4.16) actually goes over the time-dependent function $\cos\left(\phi^-(t) - \phi^+(t)\right)$. However, since the amplitude of the cosine is almost zero, except for a small region around t_{max}, the integral is approximately just the cosine evaluated at t_{max}. To summarise this chapter we can say that there is a direct relationship between the +/− phase difference and a rotation of the azimuthal angle.

5 Conclusion

In this thesis we have delved into the wide field of actually very weak oscillations of spacetime. Starting with the standing-above theory of GR, we have explored mathematical concepts to deduce and describe GWs, and limited ourselves to an interesting source of GWs, the precessing BBHs. In addition, we discussed the history and motivation behind GW measurements, detailed the detectors and data analysis processes, and finally introduced various models for simulating GWs, such as the NR surrogate, phenomenological and EOB waveform families.

The complex dynamics in mis-aligned BBH systems manifests itself in an asymmetry in the GW radiation between the $+m$ and $-m$ multipoles, which becomes significant in the merger regime. The effect is maximal for binaries with opposite spins that are completely in the orbital plane close to the merger. Technically, the important step was the transformation to a coprecessing frame that follows the precession of the orbital angular momentum, so that we can suppress artefacts such as beat effects in the waveform, and identify the anti-symmetric waveform for $\ell = 2$ and $m = \pm 2$ as the dominant one for all systems.

A discussion of the correlation between the magnitude of the recoil velocity and the mode asymmetry, showed that the anti-symmetric waveform amplitude is indeed a crucial quantity for the kick, but by far not the only quantity. Expressing the linear momentum flux in form of GW modes and separating the anti-symmetric and symmetric contributions in Eq. (4.16) shows that the recoil is a result of an interaction between both contributions. A high kick velocity can only be achieved if there is no phase difference modulo π between the (2, 2) anti-symmetric and symmetric waveform in the merger-ringdown regime and if the anti-symmetric amplitude is large. Furthermore, we found that this phase difference is related to an in-plane spin rotation of superkick configurations and thus to the specific orbital phase at the time of the merger.

The title of this thesis allows for very broad research questions, but in terms of understanding the physics of a small but not unimportant effect to improve current GW models as a next step, this thesis has made a major step. In particular, we found a $+/-$ waveform interaction responsible for the kick, which has long been known in research, but to our knowledge has never been published in this detail and disaggregation. However, in various sections we came across a few unresolved problems, such as the analysis of mode asymmetry in different rotated and boosted frames, which could lead to the disappearance of the anti-symmetric waveform, or the more accurate consideration of subdominant modes. Furthermore, we have only touched on the frequency-domain morphology of the $+/-$ waveform. It is obvious that in future work a time-domain model should be developed and compared with the frequency-domain model in `IMRPhenomXO4a` [32] or other upcoming mode asymmetry implementations.

For accurate spin and kick measurements, further investigation of the phenomenology, modelling and recoil relationship of mode asymmetry is essential, because, as detector sensitivity increases, louder signals with measurable spin misalignment are expected. Spin and kick measurements in turn will give new insights into different fields of research such as astrophysics or cosmology. Projected new ground-based detectors will be sensitive in a frequency range exactly where precessing BBHs are located [197]. The mode asymmetry including `NRSur7dq4` model will then be insufficient due to its limitations in parameter space and the short length of time series. But even for space-based detectors such as LISA, which will mainly detect other sources of GWs, waveform modelling is an ongoing process [198], and considerations about asymmetric radiation from BBHs should also hold to a certain level for other sources. All in all, there is plenty of scope for future research that will fascinate humanity for centuries to come.

Acknowledgements

I am grateful for the guidance I have received by my supervisors Shrobana Ghosh and Frank Ohme. It never felt like they were my examiners, but rather like they were long-time friends who supported me in every way. They suggested many of the research topics covered in this thesis, but were always open to new ideas and allowed me to experiment. Their scientific input during our weekly meetings has greatly improved the quality of this thesis.
I am particularly grateful to my office colleague Angela Borchers Pascual, who was always there to offer advice. Many constructive discussions with her led to improvements along the way. She also pointed out several errors in drafts of this thesis.
Furthermore, I would like to thank Noah Leon Göb, Juan Granieri, Daniel List, Max Melching, Bernd Ostermeier, Gina Sieksmeier and Luca Weber for reading this thesis, smoothing out the flow of the sections and pointing out mistakes.
Finally, I acknowledge the Max Planck Society for their support and the AEI Hanover for providing the office and computing infrastructure. I would also like to emphasise the great opportunity to gain a lot of new insights into the structures and topics of the Max Planck Society as a student assistant.

Appendix

A List of acronyms

ADM	Arnowitt-Deser-Misner
BAM	bi-functional adaptive mesh
BH	black hole
BBH	binary black hole
BNS	binary neutron star
BSSNOK	Baumgarte-Shapiro-Shibata-Nakamura-Oohara-Kojima
CBC	compact binary coalescence
CE	Cosmic Explorer
EFE	Einstein field equations
EOB	effective-one-body
ET	Einstein Telescope
GR	general relativity
GW	gravitational wave
HKHA	high kick high asymmetry
LIGO	Laser Interferometer Gravitational-Wave Observatory
LISA	Laser Interferometer Space Antenna
LKHA	low kick high asymmetry
NEMO	Neutron Star Extreme Matter Observatory
NR	numerical relativity
NS	neutron star
NSBH	neutron star-black hole
PN	post-Newtonian
PTA	pulsar timing array
SNR	signal-to-noise ratio
SpEC	Spectral Einstein Code
SXS	Simulating eXtreme Spacetime
SWSH	spin-weighted spherical harmonics
TT	transverse-traceless
$+/-$	symmetric/anti-symmetric

B Implementation of the reference time-frequency map

```
'''
Code snippet showing the implementation of the reference epoch algorithm
described in this thesis. An important function for the frame transformation
is described first.
'''


import numpy as np
import gwsurrogate as gws
import scri



def from_iner_to_copr(t, h, ell_min, ell_max):
    '''
    Transforms modes from the inertial frame into the coprecessing frame.

    Parameters
    ----------
    t : ndarray
        Time array.
    h : dict
        Dictionary of available modes with (ell, m) tuples as keys in
        the inertial frame.
    ell_min : int
        Minimum ell value.
    ell_max : int
        Maximum ell value.

    Returns
    -------
    dict
        Dictionary of modes in the coprecessing frame.
    '''
    # Build scri WaveformModes object
    data = list(h.values())
    data = np.array(data).T
    waveform_modes = scri.WaveformModes(
                            dataType=scri.h,
                            t=t,
                            data=data,
                            ell_min=ell_min,
                            ell_max=ell_max,
                            frameType=scri.Inertial,
                            r_is_scaled_out=True,
                            m_is_scaled_out=True)
```

```
    # Apply scri frame transformation
    waveform_modes.to_coprecessing_frame()
    data_copr = waveform_modes.data.T

    # Build mode dictionary
    mode_list = [(ell, m) for ell in range(ell_min, ell_max+1)
                 for m in range(-ell, ell+1)]
    h_copr = dict(zip(mode_list, data_copr))

    return h_copr



def get_f_ref(q, chi1, chi2, t_ref):
    '''
    Maps a reference time in units of M to the reference frequency in units
    of cycles/M, which is used to set the reference epoch in NRSur7dq4.

    Parameters
    ----------
    q : float
        Mass ratio m1/m2 >= 1.
    chi1 : ndarray
        Dimensionless spin of the heavier black hole.
    chi2 : ndarray
        Dimensionless spin of the lighter black hole.
    t_ref : float
        Reference time between -4300 M and -100 M to define spins.

    Returns
    -------
    float
        Reference frequency in cycles/M.
    '''
    # Generate surrogate waveform GW^0 at t^0_{ref} = -4300 M
    sur = gws.LoadSurrogate('NRSur7dq4')
    dt = 0.1
    ell_min = 2
    ell_max = 4
    t, h, dyn = sur(q, chi1, chi2, dt=dt, f_low=0)
    h_copr = from_iner_to_copr(t, h, ell_min, ell_max)

    # Get frequency-time map from GW phase
    phi_GW0 = 1/2 * (np.angle(h_copr[(2, -2)]) - np.angle(h_copr[(2, 2)]))
    phi_GW0_dot = np.diff(phi_GW0) / dt
    phi_GW0_dot = np.append(phi_GW0_dot[0], phi_GW0_dot)
```

```
    # Substitute t_{ref} and multiply conversion factor
    i_ref = np.argmin(np.abs(t - t_ref))
    f_ref = phi_GW0_dot[i_ref] / (2*np.pi)

    return f_ref



# Example output
q = 2
chi1 = [.5, .2, .5]
chi2 = [-.3, .1, .5]
t_ref = -500
f_ref = get_f_ref(q, chi1, chi2, t_ref)
print('The GW frequency at t = %.1f M is f = %.4f cyc/M' % (t_ref, f_ref))
```

References

[1] A. Einstein. "Über Gravitationswellen". In: *Sitzungsberichte der Könglich Preussischen Akademie der Wissenschaften* (1918), pp. 154–167. URL: https://echo.mpiwg-berlin.mpg.de/MPIWG:8HSP60BU.

[2] B. P. Abbott et al. "Observation of Gravitational Waves from a Binary Black Hole Merger". In: *Phys. Rev. Lett.* 116 (2016), p. 061102. DOI: 10.1103/PhysRevLett.116.061102.

[3] B. P. Abbott et al. "GWTC-1: A Gravitational-Wave Transient Catalog of Compact Binary Mergers Observed by LIGO and Virgo during the First and Second Observing Runs". In: *Phys. Rev. X* 9 (2019), p. 031040. DOI: 10.1103/PhysRevX.9.031040.

[4] R. Abbott et al. "GWTC-2: Compact Binary Coalescences Observed by LIGO and Virgo during the First Half of the Third Observing Run". In: *Physical Review X* 11.2 (2021). DOI: 10.1103/physrevx.11.021053.

[5] R. Abbott et al. "GWTC-3: Compact Binary Coalescences Observed by LIGO and Virgo During the Second Part of the Third Observing Run". In: *arXiv General Relativity and Quantum Cosmology* (2021). DOI: 10.48550/arXiv.2111.03606.

[6] B. P. Abbott et al. "GW170817: Observation of Gravitational Waves from a Binary Neutron Star Inspiral". In: *Phys. Rev. Lett.* 119 (2017), p. 161101. DOI: 10.1103/PhysRevLett.119.161101.

[7] R. Abbott et al. "Observation of Gravitational Waves from Two Neutron Star–Black Hole Coalescences". In: *The Astrophysical Journal Letters* 915.1 (2021), p. L5. DOI: 10.3847/2041-8213/ac082e.

[8] J. Antoniadis et al. "The second data release from the European Pulsar Timing Array. I. The dataset and timing analysis". In: *Astronomy and Astrophysics* (2023). DOI: 10.1051/0004-6361/202346841.

[9] G. Agazie et al. "The NANOGrav 15 yr Data Set: Evidence for a Gravitational-wave Background". In: *The Astrophysical Journal Letters* 951.1 (2023), p. L8. DOI: 10.3847/2041-8213/acdac6.

[10] D. J. Reardon et al. "Search for an Isotropic Gravitational-wave Background with the Parkes Pulsar Timing Array". In: *The Astrophysical Journal Letters* 951.1 (2023), p. L6. DOI: 10.3847/2041-8213/acdd02.

[11] F.-K. Thielemann et al. "Neutron Star Mergers and Nucleosynthesis of Heavy Elements". In: *Annual Review of Nuclear and Particle Science* 67.1 (2017), pp. 253–274. DOI: 10.1146/annurev-nucl-101916-123246.

[12] B. P. Abbott et al. "Tests of General Relativity with GW150914". In: *Physical Review Letters* 116.22 (2016). DOI: 10.1103/physrevlett.116.221101.

[13] B. P. Abbott et al. "GW170817: Measurements of Neutron Star Radii and Equation of State". In: *Physical Review Letters* 121.16 (2018). DOI: 10.1103/physrevlett.121.161101.

[14] R. Abbott et al. "Tests of General Relativity with GWTC-3". In: *arXiv General Relativity and Quantum Cosmology* (2021). DOI: 10.48550/arXiv.2112.06861.

[15] M. Sasaki et al. "Primordial black holes - perspectives in gravitational wave astronomy". In: *Classical and Quantum Gravity* 35.6 (2018), p. 063001. DOI: 10.1088/1361-6382/aaa7b4.

[16] E. Bagui et al. "Primordial black holes and their gravitational-wave signatures". In: *arXiv Cosmology and Nongalactic Astrophysics* (2023). DOI: 10.48550/arXiv.2310.19857.

[17] B. P. Abbott et al. "A Gravitational-wave Measurement of the Hubble Constant Following the Second Observing Run of Advanced LIGO and Virgo". In: *The Astrophysical Journal* 909.2 (2021), p. 218. DOI: 10.3847/1538-4357/abdcb7.

[18] B. F. Schutz. "Determining the Hubble Constant from Gravitational Wave Observations". In: *Nature* 323 (1986), pp. 310–311. DOI: 10.1038/323310a0.

[19] M. C. Guzzetti et al. "Gravitational waves from inflation". In: *La Rivista del Nuovo Cimento* 39.9 (2016), pp. 399–495. DOI: 10.1393/ncr/i2016-10127-1.

[20] B. P. Abbott et al. "First targeted search for gravitational-wave bursts from core-collapse supernovae in data of first-generation laser interferometer detectors". In: *Physical Review D* 94.10 (2016). DOI: 10.1103/physrevd.94.102001.

[21] B. P. Abbott et al. "Binary Black Hole Population Properties Inferred from the First and Second Observing Runs of Advanced LIGO and Advanced Virgo". In: *The Astrophysical Journal* 882.2 (2019), p. L24. DOI: 10.3847/2041-8213/ab3800.

[22] R. Abbott et al. "Population Properties of Compact Objects from the Second LIGO–Virgo Gravitational-Wave Transient Catalog". In: *The Astrophysical Journal Letters* 913.1 (2021), p. L7. DOI: 10.3847/2041-8213/abe949.

[23] R. Abbott et al. "The population of merging compact binaries inferred using gravitational waves through GWTC-3". In: *arXiv High Energy Astrophysical Phenomena* (2022). DOI: 10.48550/arXiv.2111.03634.

[24] V. Varma et al. "Surrogate models for precessing binary black hole simulations with unequal masses". In: *Physical Review Research* 1.3 (2019). DOI: 10.1103/physrevresearch.1.033015.

[25] M. Pürrer and C.-J. Haster. "Ready for what lies ahead? – Gravitational waveform accuracy requirements for future ground based detectors". In: *arXiv General Relativity and Quantum Cosmology* (2019). DOI: 10.48550/arXiv.1912.10055.

[26] M. Pürrer, M. Hannam and F. Ohme. "Can we measure individual black-hole spins from gravitational-wave observations?" In: *Phys. Rev. D* 93 (2016), p. 084042. DOI: 10.1103/PhysRevD.93.084042.

[27] S. Khan et al. "Including higher order multipoles in gravitational-wave models for precessing binary black holes". In: *Physical Review D* 101.2 (2020). DOI: 10.1103/physrevd.101.024056.

[28] V. Varma, M. Isi and S. Biscoveanu. "Extracting the Gravitational Recoil from Black Hole Merger Signals". In: *Phys. Rev. Lett.* 124 (2020), p. 101104. DOI: 10.1103/PhysRevLett.124.101104.

[29] J. Calderón Bustillo et al. "Tracking Black Hole Kicks from Gravitational-Wave Observations". In: *Phys. Rev. Lett.* 121 (2018), p. 191102. DOI: 10.1103/PhysRevLett.121.191102.

[30] C. O. Lousto and J. Healy. "Kicking gravitational wave detectors with recoiling black holes". In: *Phys. Rev. D* 100 (2019), p. 104039. DOI: 10.1103/PhysRevD.100.104039.

[31] M. Boyle et al. "Gravitational-wave modes from precessing black-hole binaries". In: *arXiv General Relativity and Quantum Cosmology* (2014). DOI: 10.48550/ARXIV.1409.4431.

[32] S. Ghosh, P. Kolitsidou and M. Hannam. "First frequency-domain phenomenological model of the multipole asymmetry in gravitational-wave signals from binary-black-hole coalescence". In: *arXiv General Relativity and Quantum Cosmology* (2023). DOI: 10.48550/arXiv.2310.16980.

[33] B. Brügmann et al. "Exploring black hole superkicks". In: *Phys. Rev. D* 77.12 (2008). DOI: 10.1103/physrevd.77.124047.

[34] J. B. Hartle. *Gravity: An Introduction to Einstein's General Relativity*. Benjamin Cummings, 2003. ISBN: 0-8053-8662-9.

[35] B. Schutz. *A First Course in General Relativity*. 2nd. Cambridge University Press, June 2009. ISBN: 0-521-88705-4.

[36] A. Einstein. "Näherungsweise Integration der Feldgleichungen der Gravitation". In: *Sitzungsberichte der Könglich Preussischen Akademie der Wissenschaften* (1916), pp. 688–696. URL: https://md.mpiwg-berlin.mpg.de/purls/docuview/echo/MPIWG:RA6W5W65.

[37] C. W. Misner, K. S. Thorne and J. A. Wheeler. *Gravitation*. W. H. Freeman and Company, 1973. ISBN: 0-7167-0344-0.

[38] M. Visser. "The Kerr spacetime: A brief introduction". In: *arXiv General Relativity and Quantum Cosmology* (2008). DOI: 10.48550/arXiv.0706.0622.

[39] M. Haunaske. *ART mit dem Computer*. Online, accessed 10-August-2023. 2021. URL: https://itp.uni-frankfurt.de/~hanauske/VARTC/VARTC2021.html.

[40] J. Frank, A. King and D. Raine. *Accretion Power in Astrophysics*. 3rd ed. Cambridge University Press, 2002. DOI: 10.1017/CBO9781139164245.

[41] J. D. E. Creighton and W. G. Anderson. Wiley-VCH Verlag GmbH & Co. KGaA, 2011. ISBN: 978-3-5274-0886-3. DOI: 10.1002/9783527636037.

[42] M. J. W. Hall. *General Relativity: An Introduction to Black Holes, Gravitational Waves, and Cosmology*. Morgan & Claypool Publishers, 2018. ISBN: 978-1-6817-4885-6. DOI: 10.1088/978-1-6817-4885-6.

[43] LIGO Caltech. *Sources and Types of Gravitational Waves*. Online, accessed 30-July-2023. URL: https://www.ligo.caltech.edu/page/gw-sources.

[44] L. Blanchet. "Gravitational Radiation from Post-Newtonian Sources and Inspiralling Compact Binaries". In: *Living Reviews in Relativity* 17.1 (2014). DOI: 10.12942/lrr-2014-2.

[45] C. Cutler and É. E. Flanagan. "Gravitational waves from merging compact binaries: How accurately can one extract the binary's parameters from the inspiral waveform?" In: *Physical Review D* 49.6 (1994), pp. 2658–2697. DOI: 10.1103/physrevd.49.2658.

[46] M. Ruiz et al. "Multiple expansions for energy and momenta carried by gravitational waves". In: *General Relativity and Gravitation* 40.8 (2007), pp. 1705–1729. DOI: 10.1007/s10714-007-0570-8.

[47] V. Varma, L. C. Stein and D. Gerosa. "The binary black hole explorer: on-the-fly visualizations of precessing binary black holes". In: *Classical and Quantum Gravity* 36.9 (2019), p. 095007. DOI: 10.1088/1361-6382/ab0ee9.

[48] L. E. Kidder. "Coalescing binary systems of compact objects to (post)$^{5/2}$-Newtonian order. V. Spin effects". In: *Physical Review D* 52.2 (1995), pp. 821–847. DOI: 10.1103/physrevd.52.821.

[49] J. Blackman et al. "Numerical relativity waveform surrogate model for generically precessing binary black hole mergers". In: *Physical Review D* 96.2 (2017). DOI: 10.1103/physrevd.96.024058.

[50] S. Ossokine et al. "Comparing post-Newtonian and numerical relativity precession dynamics". In: *Physical Review D* 92.10 (2015). DOI: 10.1103/physrevd.92.104028.

[51] L. Reali et al. "Mapping the asymptotic inspiral of precessing binary black holes to their merger remnants". In: *Classical and Quantum Gravity* 37.22 (2020), p. 225005. DOI: 10.1088/1361-6382/abb639.

[52] M. Boyle et al. "The SXS collaboration catalog of binary black hole simulations". In: *Classical and Quantum Gravity* 36.19 (2019), p. 195006. DOI: 10.1088/1361-6382/ab34e2.

[53] D. Ferguson et al. "Second MAYA Catalog of Binary Black Hole Numerical Relativity Waveforms". In: *arXiv General Relativity and Quantum Cosmology* (2023). DOI: 10.48550/arXiv.2309.00262.

[54] E. Hamilton et al. "A catalogue of precessing black-hole-binary numerical-relativity simulations". In: *arXiv General Relativity and Quantum Cosmology* (2023). DOI: 10.48550/arXiv.2303.05419.

[55] P. Schmidt, F. Ohme and M. Hannam. "Towards models of gravitational waveforms from generic binaries: II. Modelling precession effects with a single effective precession parameter". In: *Physical Review D* 91.2 (2015). DOI: 10.1103/physrevd.91.024043.

[56] C. L. Rodriguez et al. "Illuminating black hole binary formation channels with spins in Advanced LIGO". In: *The Astrophysical Journal Letters* 832.1 (2016), p. L2. DOI: 10.3847/2041-8205/832/1/L2.

[57] Q. Hu et al. "Semianalytical approach for sky localization of gravitational waves". In: *Physical Review D* 104.10 (2021). DOI: 10.1103/physrevd.104.104008.

[58] K. S. Thorne. "Multipole expansions of gravitational radiation". In: *Rev. Mod. Phys.* 52 (1980), pp. 299–339. DOI: 10.1103/RevModPhys.52.299.

[59] L. E. Kidder. "Using full information when computing modes of post-Newtonian waveforms from inspiralling compact binaries in circular orbit". In: *Phys. Rev. D* 77 (2008), p. 044016. DOI: 10.1103/PhysRevD.77.044016.

[60] M. Boyle and A. H. Mroué. "Extrapolating gravitational-wave data from numerical simulations". In: *Physical Review D* 80.12 (2009). DOI: 10.1103/physrevd.80.124045.

[61] J. N. Goldberg et al. "Spin-s Spherical Harmonics and ð". In: *Journal of Mathematical Physics* 8.11 (1967), pp. 2155–2161. DOI: 10.1063/1.1705135.

[62] M. Boyle. "Angular velocity of gravitational radiation from precessing binaries and the corotating frame". In: *Physical Review D* 87.10 (2013). DOI: 10.1103/physrevd.87.104006.

[63] E. P. Wigner. *Group Theory and its Application to the Quantum Mechanics of Atomic Spectra*. Academic Press, 1959. ISBN: 9780127505503. DOI: 10.1016/b978-0-12-750550-3.x5001-0.

[64] P. Schmidt et al. "Tracking the precession of compact binaries from their gravitational-wave signal". In: *Phys. Rev. D* 84 (2011), p. 024046. DOI: 10.1103/PhysRevD.84.024046.

[65] M. Boyle, D. Iozzo and L. C. Stein. *moble/scri: v1.2*. Zenodo. 2020. DOI: 10.5281/zenodo.4041972.

[66] M. Boyle, R. Owen and H. P. Pfeiffer. "Geometric approach to the precession of compact binaries". In: *Phys. Rev. D* 84 (2011), p. 124011. DOI: 10.1103/PhysRevD.84.124011.

[67] J. Weber. "Detection and Generation of Gravitational Waves". In: *Phys. Rev.* 117 (1960), pp. 306–313. DOI: 10.1103/PhysRev.117.306.

[68] J. Weber. "Gravitational Radiation". In: *Phys. Rev. Lett.* 18 (1967), pp. 498–501. DOI: 10.1103/PhysRevLett.18.498.

[69] J. Weber. "Gravitational-Wave-Detector Events". In: *Phys. Rev. Lett.* 20 (1968), pp. 1307–1308. DOI: 10.1103/PhysRevLett.20.1307.

[70] J. Weber. "Evidence for Discovery of Gravitational Radiation". In: *Phys. Rev. Lett.* 22 (1969), pp. 1320–1324. DOI: 10.1103/PhysRevLett.22.1320.

[71] J. Hough, S. Rowan and B. S. Sathyaprakash. "The search for gravitational waves". In: *Journal of Physics B: Atomic, Molecular and Optical Physics* 38.9 (2005), S497. DOI: 10.1088/0953-4075/38/9/004.

[72] R. A. Hulse and J. H. Taylor. "Discovery of a pulsar in a binary system." In: *The Astrophysical Journal* 195 (1975), pp. L51–L53. DOI: 10.1086/181708.

[73] J. H. Taylor and J. M. Weisberg. "Further Experimental Tests of Relativistic Gravity Using the Binary Pulsar PSR 1913+16". In: *The Astrophysical Journal* 345 (1989), p. 434. DOI: 10.1086/167917.

[74] R. Abbott et al. "Open data from the first and second observing runs of Advanced LIGO and Advanced Virgo". In: *SoftwareX* 13 (2021), p. 100658. DOI: https://doi.org/10.1016/j.softx.2021.100658.

[75] R. Abbott et al. "Open Data from the Third Observing Run of LIGO, Virgo, KAGRA, and GEO". In: *Astrophys. J. Suppl.* 267.2 (2023), p. 29. DOI: 10.3847/1538-4365/acdc9f.

[76] J. Aasi et al. "Advanced LIGO". In: *Classical and Quantum Gravity* 32.7 (2015), p. 074001. DOI: 10.1088/0264-9381/32/7/074001.

[77] F. Acernese et al. "Advanced Virgo: a second-generation interferometric gravitational wave detector". In: *Classical and Quantum Gravity* 32.2 (2014), p. 024001. DOI: 10.1088/0264-9381/32/2/024001.

[78] T. Akutsu et al. "KAGRA: 2.5 generation interferometric gravitational wave detector". In: *Nature Astronomy* 3.1 (2019), pp. 35–40. DOI: 10.1038/s41550-018-0658-y.

[79] G. Agazie et al. "The NANOGrav 15 yr Data Set: Observations and Timing of 68 Millisecond Pulsars". In: *The Astrophysical Journal Letters* 951.1 (2023), p. L9. DOI: 10.3847/2041-8213/acda9a.

[80] G. Agazie et al. "The NANOGrav 15 yr Data Set: Detector Characterization and Noise Budget". In: *The Astrophysical Journal Letters* 951.1 (2023), p. L10. DOI: 10.3847/2041-8213/acda88.

[81] G. Agazie et al. “The NANOGrav 15 yr Data Set: Constraints on Supermassive Black Hole Binaries from the Gravitational-wave Background”. In: *The Astrophysical Journal Letters* 952.2 (2023), p. L37. DOI: 10.3847/2041-8213/ace18b.

[82] A. Afzal et al. “The NANOGrav 15 yr Data Set: Search for Signals from New Physics”. In: *The Astrophysical Journal Letters* 951.1 (2023), p. L11. DOI: 10.3847/2041-8213/acdc91.

[83] G. Agazie et al. “The NANOGrav 15 yr Data Set: Bayesian Limits on Gravitational Waves from Individual Supermassive Black Hole Binaries”. In: *The Astrophysical Journal Letters* 951.2 (2023), p. L50. DOI: 10.3847/2041-8213/ace18a.

[84] G. Agazie et al. “The NANOGrav 15-year Data Set: Search for Anisotropy in the Gravitational-Wave Background”. In: *arXiv High Energy Astrophysical Phenomena* (2023). DOI: 10.48550/arXiv.2306.16221.

[85] A. Zic et al. “The Parkes Pulsar Timing Array Third Data Release”. In: *arXiv High Energy Astrophysical Phenomena* (2023). DOI: 10.48550/arXiv.2306.16230.

[86] D. J. Reardon et al. “The Gravitational-wave Background Null Hypothesis: Characterizing Noise in Millisecond Pulsar Arrival Times with the Parkes Pulsar Timing Array”. In: *The Astrophysical Journal Letters* 951.1 (2023), p. L7. DOI: 10.3847/2041-8213/acdd03.

[87] J. Antoniadis et al. “The second data release from the European Pulsar Timing Array II. Customised pulsar noise models for spatially correlated gravitational waves”. In: *arXiv High Energy Astrophysical Phenomena* (2023). DOI: 10.48550/arXiv.2306.16225.

[88] J. Antoniadis et al. “The second data release from the European Pulsar Timing Array III. Search for gravitational wave signals”. In: *arXiv High Energy Astrophysical Phenomena* (2023). DOI: 10.48550/arXiv.2306.16214.

[89] J. Antoniadis et al. “The second data release from the European Pulsar Timing Array IV. Search for continuous gravitational wave signals”. In: *arXiv High Energy Astrophysical Phenomena* (2023). DOI: 10.48550/arXiv.2306.16226.

[90] J. Antoniadis et al. “The second data release from the European Pulsar Timing Array: V. Implications for massive black holes, dark matter and the early Universe”. In: *arXiv Cosmology and Nongalactic Astrophysics* (2023). DOI: 10.48550/arXiv.2306.16227.

[91] C. Smarra et al. “The second data release from the European Pulsar Timing Array: VI. Challenging the ultralight dark matter paradigm”. In: *arXiv High Energy Astrophysical Phenomena* (2023). DOI: 10.48550/arXiv.2306.16228.

[92] J. D. Romano and B. Allen. “Answers to frequently asked questions about the pulsar timing array Hellings and Downs correlation curve”. In: *arXiv General Relativity and Quantum Cosmology* (2023). DOI: 10.48550/arXiv.2308.05847.

[93] S. Stahler and F. Palla. *The Formation of Stars*. 1st. WILEY-VCH Verlag GmbH & Co. KGaA, 2004. ISBN: 978-3-5274-0559-6. DOI: 10.1002/9783527618675.

[94] M. Mapelli. "Binary Black Hole Mergers: Formation and Populations". In: *Frontiers in Astronomy and Space Sciences* 7 (2020). DOI: 10.3389/fspas.2020.00038.

[95] D. Gerosa and A. Sesana. "Missing black holes in brightest cluster galaxies as evidence for the occurrence of superkicks in nature". In: *Monthly Notices of the Royal Astronomical Society* 446.1 (2014), pp. 38–55. ISSN: 0035-8711. DOI: 10.1093/mnras/stu2049.

[96] D. Merritt et al. "Consequences of Gravitational Radiation Recoil". In: *The Astrophysical Journal* 607.1 (2004), p. L9. DOI: 10.1086/421551.

[97] P. Manoharan. *Universal Relations for Binary Neutron Star Mergers with Long-lived Remnants*. 1st. Springer Spektrum Wiesbaden, Mar. 2022. ISBN: 978-3-658-36840-1. DOI: 10.1007/978-3-658-36841-8.

[98] R. Abbott et al. "All-sky search for continuous gravitational waves from isolated neutron stars using Advanced LIGO and Advanced Virgo O3 data". In: *Physical Review D* 106.10 (2022). DOI: 10.1103/physrevd.106.102008.

[99] Alexandre T. et al. "Modeling gravitational waves from exotic compact objects". In: *Physical Review D* 103.6 (2021). DOI: 10.1103/physrevd.103.064042.

[100] A. Lamberts et al. "Predicting the LISA white dwarf binary population in the Milky Way with cosmological simulations". In: *Monthly Notices of the Royal Astronomical Society* 490.4 (2019), pp. 5888–5903. DOI: 10.1093/mnras/stz2834.

[101] N. V. Krishnendu and F. Ohme. "Testing General Relativity with Gravitational Waves: An Overview". In: *Universe* 7.12 (2021), p. 497. DOI: 10.3390/universe7120497.

[102] J. Aasi et al. "Advanced LIGO". In: *Classical and Quantum Gravity* 32.7 (2015), p. 074001. DOI: 10.1088/0264-9381/32/7/074001.

[103] D. V. Martynov et al. "Sensitivity of the Advanced LIGO detectors at the beginning of gravitational wave astronomy". In: *Physical Review D* 93.11 (2016). DOI: 10.1103/physrevd.93.112004.

[104] M. Saleem et al. "The science case for LIGO-India". In: *Classical and Quantum Gravity* 39.2 (2021), p. 025004. DOI: 10.1088/1361-6382/ac3b99.

[105] LIGO Scientific Collaboration. *LSC Research Program, Instrument Science White Paper 2022-2023*. Online, accessed 17-August-2023. 2022. URL: https://www.ligo.org/about/white_paper.php.

[106] M. Maggiore et al. "Science case for the Einstein telescope". In: *Journal of Cosmology and Astroparticle Physics* 2020.03 (2020), p. 050. DOI: 10.1088/1475-7516/2020/03/050.

[107] D. Reitze et al. "Cosmic Explorer: The U.S. Contribution to Gravitational-Wave Astronomy beyond LIGO". In: *arXiv Instrumentation and Methods for Astrophysics* (2019). DOI: 10.48550/arXiv.1907.04833.

[108] K. Ackley et al. "Neutron Star Extreme Matter Observatory: A kilohertz-band gravitational-wave detector in the global network". In: *Publications of the Astronomical Society of Australia* 37 (2020). DOI: 10.1017/pasa.2020.39.

[109] P. Amaro Seoane et al. "The Gravitational Universe". In: *arXiv Cosmology and Nongalactic Astrophysics* (2013). DOI: /10.48550/arXiv.1305.5720.

[110] M. Armano et al. "Sub-Femto-g Free Fall for Space-Based Gravitational Wave Observatories: LISA Pathfinder Results". In: *Phys. Rev. Lett.* 116 (2016), p. 231101. DOI: 10.1103/PhysRevLett.116.231101.

[111] S. Kawamura et al. "Current status of space gravitational wave antenna DECIGO and B-DECIGO". In: *Progress of Theoretical and Experimental Physics* 2021.5 (Feb. 2021), 05A105. DOI: 10.1093/ptep/ptab019.

[112] J. Luo et al. "TianQin: a space-borne gravitational wave detector". In: *Classical and Quantum Gravity* 33.3 (2016), p. 035010. DOI: 10.1088/0264-9381/33/3/035010.

[113] A. H. Nitz et al. "3-OGC: Catalog of Gravitational Waves from Compact-binary Mergers". In: *The Astrophysical Journal* 922.1 (2021), p. 76. DOI: 10.3847/1538-4357/ac1c03.

[114] D. Davis et al. "Subtracting glitches from gravitational-wave detector data during the third LIGO-Virgo observing run". In: *Classical and Quantum Gravity* 39.24 (2022), p. 245013. DOI: 10.1088/1361-6382/aca238.

[115] S. A. Usman et al. "The PyCBC search for gravitational waves from compact binary coalescence". In: *Classical and Quantum Gravity* 33.21 (2016), p. 215004. DOI: 10.1088/0264-9381/33/21/215004.

[116] B. P. Abbott et al. "A guide to LIGO–Virgo detector noise and extraction of transient gravitational-wave signals". In: *Classical and Quantum Gravity* 37.5 (2020), p. 055002. DOI: 10.1088/1361-6382/ab685e.

[117] M. Maggiore. *Gravitational Waves: Volume 1: Theory and Experiments*. Oxford University Press, 2007. ISBN: 9780198570745. DOI: 10.1093/acprof:oso/9780198570745.001.0001.

[118] M. Vallisneri. "Use and abuse of the Fisher information matrix in the assessment of gravitational-wave parameter-estimation prospects". In: *Physical Review D* 77.4 (2008). DOI: 10.1103/physrevd.77.042001.

[119] A. Nitz et al. *gwastro/pycbc: v2.2.1 release of PyCBC*. Version v2.2.1. 2023. DOI: 10.5281/zenodo.8190155.

[120] C. Messick et al. "Analysis framework for the prompt discovery of compact binary mergers in gravitational-wave data". In: *Physical Review D* 95.4 (2017). DOI: 10.1103/physrevd.95.042001.

[121] F. Aubin et al. "The MBTA pipeline for detecting compact binary coalescences in the third LIGO–Virgo observing run". In: *Classical and Quantum Gravity* 38.9 (2021), p. 095004. DOI: 10.1088/1361-6382/abe913.

[122] G. Ashton et al. "Bilby: A User-friendly Bayesian Inference Library for Gravitational-wave Astronomy". In: *The Astrophysical Journal Supplement Series* 241.2 (2019), p. 27. DOI: 10.3847/1538-4365/ab06fc.

[123] J. Veitch et al. "Parameter estimation for compact binaries with ground-based gravitational-wave observations using the LALInference software library". In: *Physical Review D* 91.4 (2015). DOI: 10.1103/physrevd.91.042003.

[124] C. M. Biwer et al. "PyCBC Inference: A Python-based Parameter Estimation Toolkit for Compact Binary Coalescence Signals". In: *Publications of the Astronomical Society of the Pacific* 131.996 (2019), p. 024503. DOI: 10.1088/1538-3873/aaef0b.

[125] LIGO Scientific Collaboration. *LIGO Algorithm Library - LALSuite*. free software (GPL). 2018. DOI: 10.7935/GT1W-FZ16.

[126] K. D. Kokkotas and B. G. Schmidt. "Quasi-Normal Modes of Stars and Black Holes". In: *Living Reviews in Relativity* 2.1 (1999). DOI: 10.12942/lrr-1999-2.

[127] L. Rezzolla and O. Zanotti. *Relativistic Hydrodynamics*. Oxford University Press, 2013. ISBN: 9780198528906. DOI: 10.1093/acprof:oso/9780198528906.001.0001.

[128] C. Palenzuela. "Introduction to Numerical Relativity". In: *Frontiers in Astronomy and Space Sciences* 7 (2020). DOI: 10.3389/fspas.2020.00058.

[129] R. Arnowitt, S. Deser and C. W. Misner. "Dynamical Structure and Definition of Energy in General Relativity". In: *Physical Review* 116.5 (1959), pp. 1322–1330. DOI: 10.1103/PhysRev.116.1322.

[130] M. Shibata and T. Nakamura. "Evolution of three-dimensional gravitational waves: Harmonic slicing case". In: *Phys. Rev. D* 52 (1995), pp. 5428–5444. DOI: 10.1103/PhysRevD.52.5428.

[131] T. W. Baumgarte and S. L. Shapiro. "Numerical integration of Einstein's field equations". In: *Phys. Rev. D* 59 (1998), p. 024007. DOI: 10.1103/PhysRevD.59.024007.

[132] E. Newman and R. Penrose. "An Approach to gravitational radiation by a method of spin coefficients". In: *J. Math. Phys.* 3 (1962), pp. 566–578. DOI: 10.1063/1.1724257.

[133] C. Reisswig and D. Pollney. "Notes on the integration of numerical relativity waveforms". In: *Classical and Quantum Gravity* 28.19 (2011), p. 195015. DOI: 10.1088/0264-9381/28/19/195015.

[134] M. Campanelli et al. "Comparison of numerical and post-Newtonian waveforms for generic precessing black-hole binaries". In: *Physical Review D* 79.8 (2009). DOI: 10.1103/physrevd.79.084010.

[135] D. J. A. McKechan, C. Robinson and B. S. Sathyaprakash. "A tapering window for time-domain templates and simulated signals in the detection of gravitational waves from coalescing compact binaries". In: *Classical and Quantum Gravity* 27.8 (2010), p. 084020. DOI: 10.1088/0264-9381/27/8/084020.

[136] L. Santamaria et al. "Matching post-Newtonian and numerical relativity waveforms: Systematic errors and a new phenomenological model for nonprecessing black hole binaries". In: *Physical Review D* 82.6 (2010). DOI: 10.1103/physrevd.82.064016.

[137] L. Kidder et al. "Black hole evolution by spectral methods". In: *Physical Review D* 62.8 (2000). DOI: 10.1103/physrevd.62.084032.

[138] B. Brügmann. "Adaptive mesh and geodesically sliced Schwarzschild spacetime in 3+1 dimensions". In: *Physical Review D* 54.12 (1996), pp. 7361–7372. DOI: 10.1103/physrevd.54.7361.

[139] P. Ajith et al. "A phenomenological template family for black-hole coalescence waveforms". In: *Classical and Quantum Gravity* 24.19 (2007), S689–S699. DOI: 10.1088/0264-9381/24/19/s31.

[140] Sebastian K. et al. "Frequency-domain gravitational waves from nonprecessing black-hole binaries. II. A phenomenological model for the advanced detector era". In: *Physical Review D* 93.4 (2016). DOI: 10.1103/physrevd.93.044007.

[141] L. London et al. "First Higher-Multipole Model of Gravitational Waves from Spinning and Coalescing Black-Hole Binaries". In: *Physical Review Letters* 120.16 (2018). DOI: 10.1103/physrevlett.120.161102.

[142] S. Khan et al. "Phenomenological model for the gravitational-wave signal from precessing binary black holes with two-spin effects". In: *Physical Review D* 100.2 (2019). DOI: 10.1103/physrevd.100.024059.

[143] S. Khan et al. "Including higher order multipoles in gravitational-wave models for precessing binary black holes". In: *Physical Review D* 101.2 (2020). DOI: 10.1103/physrevd.101.024056.

[144] G. Pratten et al. "Setting the cornerstone for a family of models for gravitational waves from compact binaries: The dominant harmonic for nonprecessing quasicircular black holes". In: *Phys. Rev. D* 102 (2020), p. 064001. DOI: 10.1103/PhysRevD.102.064001.

[145] C. García-Quirós et al. "Multimode frequency-domain model for the gravitational wave signal from nonprecessing black-hole binaries". In: *Physical Review D* 102.6 (2020). DOI: 10.1103/physrevd.102.064002.

[146] G. Pratten et al. "Computationally efficient models for the dominant and subdominant harmonic modes of precessing binary black holes". In: *Physical Review D* 103.10 (2021). DOI: 10.1103/physrevd.103.104056.

[147] Jonathan E. Thompson et al. *PhenomXO4a: a phenomenological gravitational-wave model for precessing black-hole binaries with higher multipoles and asymmetries*. 2023. DOI: /10.48550/arXiv.2312.10025.

[148] H. Estellés et al. "Phenomenological time domain model for dominant quadrupole gravitational wave signal of coalescing binary black holes". In: *Physical Review D* 103.12 (2021). DOI: 10.1103/physrevd.103.124060.

[149] H. Estellés et al. "Time domain phenomenological model of gravitational wave subdominant harmonics for quasi-circular non-precessing binary black hole coalescences". In: *arXiv General Relativity and Quantum Cosmology* (2020). DOI: /10.48550/arXiv.2012.11923.

[150] H. Estellés et al. "New twists in compact binary waveform modeling: A fast time-domain model for precession". In: *Physical Review D* 105.8 (2022). DOI: 10.1103/physrevd.105.084040.

[151] A. Buonanno and T. Damour. "Effective one-body approach to general relativistic two-body dynamics". In: *Physical Review D* 59.8 (1999). DOI: 10.1103/physrevd.59.084006.

[152] M. Maggiore. *Gravitational Waves: Volume 2: Astrophysics and Cosmology*. Oxford University Press, 2018. ISBN: 9780198570899. DOI: 10.1093/oso/9780198570899.001.0001.

[153] T. Damour et al. "Accurate effective-one-body waveforms of inspiralling and coalescing black-hole binaries". In: *Physical Review D* 78.4 (2008). DOI: 10.1103/physrevd.78.044039.

[154] A. Taracchini et al. "Prototype effective-one-body model for nonprecessing spinning inspiral-merger-ringdown waveforms". In: *Physical Review D* 86.2 (2012). DOI: 10.1103/physrevd.86.024011.

[155] E. Barausse, E. Racine and A. Buonanno. "Hamiltonian of a spinning test particle in curved spacetime". In: *Physical Review D* 80.10 (2009). DOI: 10.1103/physrevd.80.104025.

[156] Y. Pan et al. "Inspiral-merger-ringdown waveforms of spinning, precessing black-hole binaries in the effective-one-body formalism". In: *Physical Review D* 89.8 (2014). DOI: 10.1103/physrevd.89.084006.

[157] A. Ramos-Buades et al. "SEOBNRv5PHM: Next generation of accurate and efficient multipolar precessing-spin effective-one-body waveforms for binary black holes". In: *arXiv General Relativity and Quantum Cosmology* (2023). DOI: 10.48550/ARXIV.2303.18046.

[158] M. Pürrer. "Frequency-domain reduced order models for gravitational waves from aligned-spin compact binaries". In: *Classical and Quantum Gravity* 31.19 (2014), p. 195010. DOI: 10.1088/0264-9381/31/19/195010.

[159] M. Pürrer. "Frequency domain reduced order model of aligned-spin effective-one-body waveforms with generic mass ratios and spins". In: *Physical Review D* 93.6 (2016). DOI: 10.1103/physrevd.93.064041.

[160] S. E. Field et al. "Fast Prediction and Evaluation of Gravitational Waveforms Using Surrogate Models". In: *Phys. Rev. X* 4 (2014), p. 031006. DOI: 10.1103/PhysRevX.4.031006.

[161] M. Tiglio and A. Villanueva. "Reduced order and surrogate models for gravitational waves". In: *Living Reviews in Relativity* 25.1 (2022). DOI: 10.1007/s41114-022-00035-w.

[162] J. Blackman et al. "Fast and Accurate Prediction of Numerical Relativity Waveforms from Binary Black Hole Coalescences Using Surrogate Models". In: *Physical Review Letters* 115.12 (2015). DOI: 10.1103/physrevlett.115.121102.

[163] V. Varma et al. "Surrogate model of hybridized numerical relativity binary black hole waveforms". In: *Physical Review D* 99.6 (2019). DOI: 10.1103/physrevd.99.064045.

[164] T. Islam et al. "Eccentric binary black hole surrogate models for the gravitational waveform and remnant properties: Comparable mass, nonspinning case". In: *Phys. Rev. D* 103 (2021), p. 064022. DOI: 10.1103/PhysRevD.103.064022.

[165] T. Islam et al. "Surrogate model for gravitational wave signals from nonspinning, comparable-to large-mass-ratio black hole binaries built on black hole perturbation theory waveforms calibrated to numerical relativity". In: *Physical Review D* 106.10 (2022). DOI: 10.1103/physrevd.106.104025.

[166] M. Boschini et al. "Extending black-hole remnant surrogate models to extreme mass ratios". In: *arXiv General Relativity and Quantum Cosmology* (2023). DOI: 10.48550/arXiv.2307.03435.

[167] T. Islam. "Interplay between numerical relativity and black hole perturbation theory in the intermediate-mass-ratio regime". In: *Physical Review D* 108.4 (2023). DOI: 10.1103/physrevd.108.044013.

[168] SXS Collaboration. *SXS Gravitational Waveform Database*. Online, accessed 13-November-2023. 2020. URL: http://www.black-holes.org/waveforms.

[169] J. Calderón Bustillo et al. "Tracking Black Hole Kicks from Gravitational-Wave Observations". In: *Physical Review Letters* 121.19 (2018). DOI: 10.1103/physrevlett.121.191102.

[170] V. Varma, M. Isi and S. Biscoveanu. "Extracting the Gravitational Recoil from Black Hole Merger Signals". In: *Phys. Rev. Lett.* 124 (2020), p. 101104. DOI: 10.1103/PhysRevLett.124.101104.

[171] C. Kalaghatgi and M. Hannam. "Investigating the effect of in-plane spin directions for precessing binary black hole systems". In: *Physical Review D* 103.2 (2021). DOI: 10.1103/physrevd.103.024024.

[172] N. V. Krishnendu and F. Ohme. "Interplay of spin-precession and higher harmonics in the parameter estimation of binary black holes". In: *Phys. Rev. D* 105 (2022), p. 064012. DOI: 10.1103/PhysRevD.105.064012.

[173] P. Virtanen et al. "SciPy 1.0: Fundamental Algorithms for Scientific Computing in Python". In: *Nature Methods* 17 (2020), pp. 261–272. DOI: 10.1038/s41592-019-0686-2.

[174] F. J. Harris. "On the use of windows for harmonic analysis with the discrete Fourier transform". In: *Proceedings of the IEEE* 66.1 (1978), pp. 51–83. DOI: 10.1109/PROC.1978.10837.

[175] J. W. Gibbs. "Fourier's Series". In: *Nature* 59.1522 (1898), pp. 200–200. DOI: 10.1038/059200b0.

[176] C. R. Harris et al. "Array programming with NumPy". In: *Nature* 585.7825 (2020), pp. 357–362. DOI: 10.1038/s41586-020-2649-2.

[177] E. Hamilton et al. "Model of gravitational waves from precessing black-hole binaries through merger and ringdown". In: *Physical Review D* 104.12 (2021). DOI: 10.1103/physrevd.104.124027.

[178] D. Keppel et al. "Momentum flow in black-hole binaries. I. Post-Newtonian analysis of the inspiral and spin-induced bobbing". In: *Physical Review D* 80.12 (2009). DOI: 10.1103/physrevd.80.124015.

[179] M. Campanelli et al. "Large Merger Recoils and Spin Flips from Generic Black Hole Binaries". In: *The Astrophysical Journal* 659.1 (2007), pp. L5–L8. DOI: 10.1086/516712.

[180] J. A. González et al. "Supermassive Recoil Velocities for Binary Black-Hole Mergers with Antialigned Spins". In: *Phys. Rev. Lett.* 98 (2007), p. 231101. DOI: 10.1103/PhysRevLett.98.231101.

[181] A. Ashtekar and B. Krishnan. "Isolated and Dynamical Horizons and Their Applications". In: *Living Reviews in Relativity* 7.1 (2004). DOI: 10.12942/lrr-2004-10.

[182] M. Campanelli, C. O. Lousto and Y. Zlochower. "Spinning-black-hole binaries: The orbital hang-up". In: *Physical Review D* 74.4 (2006). DOI: 10.1103/physrevd.74.041501.

[183] C. O. Lousto and Y. Zlochower. "Hangup Kicks: Still Larger Recoils by Partial Spin-Orbit Alignment of Black-Hole Binaries". In: *Phys. Rev. Lett.* 107 (2011), p. 231102. DOI: 10.1103/PhysRevLett.107.231102.

[184] D. Gerosa, F. Hébert and L. C. Stein. "Black-hole kicks from numerical-relativity surrogate models". In: *Physical Review D* 97.10 (2018). DOI: 10.1103/physrevd.97.104049.

[185] Vijay V. et al. "High-Accuracy Mass, Spin, and Recoil Predictions of Generic Black-Hole Merger Remnants". In: *Physical Review Letters* 122.1 (2019). DOI: 10.1103/physrevlett.122.011101.

[186] A. Borchers and F. Ohme. "Inconsistent black hole kick estimates from gravitational-wave models". In: *Classical and Quantum Gravity* 40.9 (2023), p. 095008. DOI: 10.1088/1361-6382/acc5da.

[187] F. Pretorius. "Binary Black Hole Coalescence". In: *arXiv General Relativity and Quantum Cosmology* (2007). DOI: 10.48550/arXiv.0710.1338.

[188] J. Healy and C. O. Lousto. "Ultimate Black Hole Recoil: What the maximum high energy collisions kick is?" In: *arXiv General Relativity and Quantum Cosmology* (2022). DOI: 10.48550/arXiv.2301.00018.

[189] H. H. Koppelman and A. Helmi. "Determination of the escape velocity of the Milky Way using a halo sample selected based on proper motion". In: *Astronomy and Astrophysics* 649 (2021), A136. DOI: 10.1051/0004-6361/202038777.

[190] É. Racine, A. Buonanno and L. Kidder. "Recoil velocity at second post-Newtonian order for spinning black hole binaries". In: *Physical Review D* 80.4 (2009). DOI: 10.1103/physrevd.80.044010.

[191] M. Campanelli et al. "Maximum Gravitational Recoil". In: *Phys. Rev. Lett.* 98 (2007), p. 231102. DOI: 10.1103/PhysRevLett.98.231102.

[192] C. O. Lousto et al. "Remnant masses, spins and recoils from the merger of generic black hole binaries". In: 27.11 (2010), p. 114006. DOI: 10.1088/0264-9381/27/11/114006.

[193] C. O. Lousto and Y. Zlochower. "Modeling maximum astrophysical gravitational recoil velocities". In: *Phys. Rev. D* 83 (2011), p. 024003. DOI: 10.1103/PhysRevD.83.024003.

[194] C. O. Lousto and Y. Zlochower. "Nonlinear gravitational recoil from the mergers of precessing black-hole binaries". In: *Phys. Rev. D* 87 (2013), p. 084027. DOI: 10.1103/PhysRevD.87.084027.

[195] Y. Zlochower and C. O. Lousto. "Modeling the remnant mass, spin, and recoil from unequal-mass, precessing black-hole binaries: The intermediate mass ratio regime". In: *Phys. Rev. D* 92 (2015), p. 024022. DOI: 10.1103/PhysRevD.92.024022.

[196] J. D. Schnittman et al. "Anatomy of the binary black hole recoil: A multipolar analysis". In: *Physical Review D* 77.4 (2008). DOI: 10.1103/physrevd.77.044031.

[197] M. Pieroni, A. Ricciardone and E. Barausse. "Detectability and parameter estimation of stellar origin black hole binaries with next generation gravitational wave detectors". In: *Scientific Reports* 12.1 (2022). DOI: 10.1038/s41598-022-19540-7.

[198] N. Afshordi et al. "Waveform Modelling for the Laser Interferometer Space Antenna". In: *arXiv General Relativity and Quantum Cosmology* (2023). DOI: 10.48550/arXiv.2311.01300.

Eigenständigkeitserklärung/ Declaration of originality

Hiermit versichere ich gem. § 7 Abs. 5 der PO 2020, diese Arbeit selbstständig verfasst zu haben und keine anderen als die angegebenen Quellen und Hilfsmittel benutzt zu haben. Alle Stellen der Arbeit, die wörtlich oder sinngemäß aus anderen Quellen übernommen wurden, sind als solche kenntlich gemacht. Die Arbeit lag weder in gleicher, noch in ähnlicher Form bereits einer Prüfungsbehörde vor.

I hereby declare, according to § 7 para. 5 of the examination regulations 2020, that I have independently written this thesis and have not used any sources or aids other than those stated. Any sections of the paper that have been taken verbatim or paraphrased from other sources are clearly indicated as such. The thesis has not been submitted to an examination board in the same or similar form before.

Hannover, 24.11.2023

Ort, Datum

Jannik Mielke

Unterschrift